SURFACE STRUCTURE DETERMINATION BY LOW-ENERGY ELECTRON DIFFRACTION

Thesis by

A. C. Sobrero

In Partial Fulfillment of the Requirements

for the Degree of

Doctor of Philosophy

California Institute of Technology

Pasadena, California

2002

(Defended June 1, 1984)

Acknowledgments

It is a pleasure to thank Professor Henry Weinberg for his support and direction as well as the freedom he gave us to pursue our intellectual muses. Ellen Williams was a wonderful colleague, and her collaboration, training, encouragement, and moral support are greatly appreciated. Numerous discussions with Kurt Fickie and John Vajo, sometimes well into the night, greatly benefited the ideas that eventually developed into this work. Kathy Bubash's friendliness and good cheer in the face of complicated formulas and other adversity are greatly appreciated. It is especially gratifying to thank my parents who have always taken an interest in my work and supported my endeavors.

Abstract

Four aspects of low-energy electron diffraction (LEED) have been investigated: interpretation of spot patterns to determine the surface unit cell and possible ambiguities, development of a photographic method for measuring angles of incidence and determining alignment of the LEED instrument, study of reliability factors used for intensity analysis, and justification for equivalent beam averaging.

The interpretation of LEED spot patterns to determine the geometry of the surface unit cell can be involved when there are several symmetrically equivalent structural domains contributing to the pattern. Complex patterns can be deciphered by the algorithm described in Chapter II. The algorithm determines a surface unit cell that is often unique but not always, as where a p(2 x 2) pattern from a fcc(111) surface can be produced by a true (2 x 2) overlayer or by three domains of a (2 x 1) structure. This ambiguity arises on surfaces with 6m symmetry, such as fcc(111) and hcp(0001), for spot patterns with threefold rotational symmetry.

In Chapter III, a broadly applicable photographic method for measuring angles of incidence and determining the alignment of the LEED instruments is described. Two published methods for determining the angle of incidence are special cases of this general procedure. The procedure extends the photographic methods and facilitates the verification of the alignment of the components of the LEED instrument.

Reliability factors are used to evaluate correspondence between computed and observed LEED intensity spectra. Zanazzi and Jona, Pendry, and Sobrero and Weinberg have proposed reliability factors that are examined in Chapter IV. Chapter V provides a

theoretical analysis and shows that averaging over momentum space gives the best resolution of the surface structure while energy averaging smears out information in the intensity spectra.

Chapter VI provides a theoretical basis for the procedure of equivalent beam averaging, which provides a first-order correction to LEED intensities for systematic error due to angular misalignment of the incident beam and corrects for misorientation (where the actual surface plane is at a slight angle to the desired crystal plane). The potential of higher-order corrections is discussed.

Table of Contents

Chapter I

Introduction: Determination of Surface Structure by LEED

Introduction: Determination of Surface Structure by LEED

The determination of surface structure by LEED requires that experimental data be compared with computed intensity spectra. The reliability factor, or R-factor, is a quantitative measure of the level of agreement between the experiment and the computation. As the parameters in the theory are varied, the quality of the fit changes continuously. The underlying assumption is that the parameter values that optimize the fit are the closest to the true, physical parameters. This requires that the model employed in the fitting procedure be an accurate approximation of the true scattering process. The dynamical theory of LEED has been quite successful in this regard.

The dynamical theory has been used to study free electron metal surfaces, such as that of aluminum, as well as the more complex transition metals and semiconductors. A variety of molecular overlayers have also been studied. One thrust of research in LEED theory is in exploring new approximations to reduce the expense of the computations when large unit cells are involved (1-2), or when high energies are used (3). Despite the successes of LEED, there are systematic discrepancies between measured and calculated intensities even for simple surfaces.

The lack of perfect agreement is due to problems in the experiments and in the theory. For some surfaces, there are great difficulties in obtaining reproducible experimental data. The W(001)-(1 x 1) high temperature phase is a case in point. In a comparison of experimental data from six research groups (4-9), Stevens and Russell found large discrepancies. One cannot demand of the theory that it fit such data very closely, and even if good agreement could be obtained in all cases, the results would not be meaningful. Data can be fitted only to within the experimental uncertainty. Fine-tuning

beyond that is "fitting the noise" and devoid of significance.

Other experimental considerations are the irreproducibility of data for beams at glancing angles to the surface or of the absolute intensities in overlayer systems. Both of these effects are due to lateral disorder on the surface. Glancing beams have a large instrumental transfer width (10), which makes them sensitive to fine details of the lateral structure of the surface, including steps and other defects (11). The disposition of these defects depends on uncontrollable factors affected by the preparation of the sample. A sample aligned to within $\pm\frac{1}{2}^\circ$ of a nominal low Miller index surface will have on average one step every 70 lattice spacings along the azimuthal direction of the misalignment. The polishing procedure adds a random component of steps, and cleaning by ion bombardment adds point defects. In addition, there are surface manifestations of defects already present in the bulk such as dislocations. For angles of incidence and emergence near the surface normal, these defects redistribute elastic intensity only within the Brillouin zone, but at glancing angles the geometric view factor becomes important and even the integrated beam intensities are irreproducible.

Adsorbed overlayers present experimental difficulties because they cannot always be regenerated with a constant degree of order. For the Ru(001) $(\sqrt{3} \times \sqrt{3})R30^\circ$-CO system, both the exposure of the clean surface to the gas and the subsequent anneal have to be controlled rigorously in order to obtain reproducible intensities (12). The total electron dose (13) and the rate of dosing (beam current) (14) also affect the observed intensities. These factors make the comparison of absolute intensities subject to large experimental uncertainties.

Fortunately, the absolute intensities are not needed for structure determination; it is sufficient to compare the relative intensities. There is a problem, though, in that there is

no consensus regarding how to normalize the intensity spectra or how to gauge the level of agreement among the normalized curves. The lack of consensus is manifested in the use of various R-factors by various research groups. Since different R-factors give different surface structures as the optimum, the lack of consensus has real consequences.

References

1. N. Stoner, M. A. Van Hove, S. Y. Tong and M. B. Webb, Phys. Rev. Letters **40**, 243 (1978).
2. W. S. Yang, F. Jona and P. M. Marcus, Phys. Rev. B **27**, 1394 (1983).
3. J. B. Pendry, Inst. Phys. Conf. Ser. No.**41**, 205 (1978).
4. B. W. Lee, A. Ignatiev, S. Y. Tong and M. Van Hove, J. Vac. Sci. Technol. **14**, 291 (1977).
5. M. K. Debe, D. A. King and F. S. Marsh, Surface Sci. **68**, 37 (1977).
6. M. Kalisvaart, M. R. O'Neill, T. W. Riddle, F. B. Dunning and G. K. Walters, Phys. Rev. B **17**, 1570 (1978).
7. M. N. Read and G. R. Russell, Surface Sci. **88**, 95 (1979).
8. P. Heilmann, K. Heinz and K. Müller, Surface Sci. **89**, 84 (1979).
9. M. A. Stevens and G. R. Russell, Surface Sci. **104**, 354 (1981).
10. R. L. Park, J. E. Houston and D. G. Schreiner, Rev. Sci. Instrum. **42**, 60 (1971).
11. M. Henzler, Surface Sci. **73**, 240 (1978).
12. E. D. Williams, W. H. Weinberg and A. C. Sobrero, J. Chem. Phys. **76**, 1150 (1982).
13. T. E. Madey and D. Menzel, Japan J. Appl. Phys. Suppl. **2**, Pt. 2, 229 (1974).
14. C. W. Tucker, Jr., Surface Sci. **2**, 516 (1964).

Chapter II

Interpretation of LEED Spot Patterns and Possible Ambiguities

Abstract

The matrix notation for describing the structure of an overlayer in terms of the substrate unit vectors does not give a unique matrix for the structure. We discuss the equivalence class of matrices that all specify the same structure and demonstrate how to determine if two matrices are equivalent. This provides a convenient method for determining the point group symmetry of a structure from its matrix. The matrix theory is used to develop an algorithm for unscrambling the LEED pattern resulting from a superposition of patterns from symmetrically equivalent antiphase domains for simply related overlayers. Due to the existence of symmetrically equivalent domains, certain surface nets cannot be deduced unambiguously from their LEED patterns. A well-known example occurs for a p(2 x 2) overlayer on a fcc(111) or hcp(0001) substrate, the diffraction pattern of which can be interpreted as due either to a true (2 x 2) unit cell or to three domains of a (2 x 1) structure. It is demonstrated that this is the only type of ambiguity that can arise where the pattern resulting from a superposition of several Bravais lattices appears as a single Bravais lattice.

1. Introduction

When examining a new surface structure with low-energy electron diffraction (LEED), the first task is to determine the size and shape of the unit cell. This information is needed to complete the characterization of the structure. For an adsorbed overlayer, the shape of the surface unit cell can suggest the absolute coverage at saturation and occasionally even the adsorption site. If more than one structural phase occurs, either as a function of coverage or of temperature, the surface unit cells play a fundamental role in the understanding of the interatomic forces which lead to the phase transition.

For complex LEED patterns, the process of determining the true surface net has been described as a "nontrivial task requiring a certain amount of imagination" (1). In the absence of domains, the pattern on a LEED screen is a representation of the reciprocal lattice of the surface. The two-dimensional unit cell is determined easily from such a pattern. Complications arise, however, when there are several domains of an adsorbed ordered overlayer on a high-symmetry substrate. This complicating factor has two unfortunate consequences concerning the interpretation of LEED patterns. The obvious effect is that the pattern is difficult to interpret because the reciprocal lattices for each of the domains are all superimposed. A more subtle consequence is that it is not always possible to specify a unique surface net corresponding to the observed pattern. Such an ambiguity occurs on the Ir(111)-(2 x 2)-O surface, where either a single domain of a *bona fide* (2 x 2) overlayer or three rotationally symmetric domains of a (2 x 1) structure would both give the observed (2 x 2) pattern (2).

It is important to know which patterns can be interpreted in more than one way and to generate all possible interpretations. Without some underlying theory, it would be difficult to say whether all the possible surface nets corresponding to an observed

pattern had been exhibited or if a more complete search would yield new interpretations. Fortunately, it can be proven that there is only one type of ambiguity where the superposition or several Bravais lattices is ambiguous with the pattern produced by one or two overlayer domains. This occurs on a substrate with a hexagonal Bravais lattice where an overlayer which produces a p(S x S)Rφ° pattern may have either a (S x S) unit cell or three mutually rotated domains of a (S/2 x S) structure. Examples of this type of ambiguity abound, including Ir(111)-(2 x 2)-O (2), Rh(111)-(2 x 2)-O (3), Pt(111)-(6 x 6)-naphthalene (4) and UO2(111) (2$\sqrt{3}$ x $\sqrt{3}$)R30° (5). Other structures such as the Ru(0001)-($\sqrt{3}$ x $\sqrt{3}$)R30°-CO (6) would give rise to ambiguity if the adsorbate were bonded to a bridge site of the substrate rather than in an on-top site.

It is well known that the space group of the surface structure can seldom be determined completely from the diffraction pattern alone. Even the occurrence of a glide plane in one domain can be obscured by the presence of a rotated domain, as has been observed on the reconstructed W(100)($\sqrt{2}$ x $\sqrt{2}$)R45° surface (7, 8). Hence, the determination of space groups remains a difficult task. On the other hand, the analysis of the LEED pattern to deduce the surface unit cell can be reduced to a straightforward procedure if the overlayer is known to be related simply to the substrate. We exclude rationally related coincidence lattices and incommensurate overlayers from this discussion. Multiple scattering between a coincidence lattice and the substrate leads to ambiguity and other complications of interpretation for virtually any system.

In Section 2, the theory of Bravais lattices and structure matrices is presented. The matrix notation introduced by Park and Madden (9) is used to specify the lateral structure of an overlayer. Section 3 contains an algorithm for simply related surface structures to unscramble a complex LEED spot pattern into its component domains. It is assumed that the true LEED pattern is well resolved and completely known. This seldom

presents a limitation in practice since the missing spots in an incomplete pattern can be identified and filled in. We illustrate this procedure as well as the power of the algorithm for unscrambling complex structures with a number of examples. In Section 4 we discuss ambiguity and demonstrate that only the hexagonal overlayer on a hexagonal lattice presents any difficulties.

2. Bravais Lattices and Structure Matrices

The matrix notation used to specify the lateral structure of the overlayer in terms of the substrate unit vectors provides a convenient and powerful formalism for the analysis of LEED patterns (9). The 2 x 2 matrix for a superlattice represents the structure in terms of the substrate lattice unit vectors. The rows of these covariant structure matrices are the vectors specifying the Bravais lattice. The corresponding matrices in reciprocal space are contravariant with the columns giving the reciprocal unit vectors. The advantage of the matrix formalism is that much of linear algebra can be applied. For example, if S is a structure matrix, the reciprocal matrix is simply the inverse S^{-1}. A disadvantage is that the structure matrix for a Bravais lattice is not unique, as can be seen in Figure 1. We will define the equivalence class of S to consist of all the matrices that produce the same lattice. We say that S_1 is equivalent to S_2 when for any 1 x 2 integer vector m there exists an integer vector n with $mS_1 = nS_2$ and, conversely, for all integer vectors n there exists a corresponding m.

The absolute value of the determinant of S is the area of the two-dimensional unit cell. Hence, for two matrices S_1 and S_2 to be in an equivalence class it is necessary but not sufficient that

$$|\det S_1| = |\det S_2|. \qquad (1)$$

Equivalence is completely established by the following:

Theorem: The structure matrices S_1 and S_2 are equivalent if and only if there exists an integer matrix U of determinant ±1 with

$$S_1 = US_2. \qquad (2)$$

Proof: We note that $V = U^{-1}$ is also an integer matrix of determinant ±1, so that we have the symmetric condition

$$S_2 = VS_1. \qquad (3)$$

The first part of the theorem is therefore trivial: if there is a U satisfying Equation (2), then for any integer vector m the integer vector given by $n = mU$ satisfies $mS_1 = nS_2$. Conversely, for any n, $m = nV$ is the required integer vector. To prove the *only if* part of the theorem we need to show that if S_1 and S_2 are equivalent then an integer matrix U with $|\det U| = 1$ exists.

For the unit vectors $m_1 = (1\ 0)$ and $m_2 = (0\ 1)$ there are integer vectors n_1 and n_2 given by the equivalence $m_iS_1 = n_iS_2$ for $i = 1, 2$.

Define $U = \begin{bmatrix} n_1 \\ n_2 \end{bmatrix}$ and note that the identity matrix I is equal to $\begin{bmatrix} m_1 \\ m_2 \end{bmatrix}$. Hence

$$IS_1 = US_2. \qquad (4)$$

Since $|\det S_1| = |\det S_2| \neq 0$, we must have $\det U = \pm 1$, thus completing the proof. A corollary is that reciprocal matrices are equivalent if there exists an integer matrix U of determinant ±1 with $S_1 = S_2U$.

This theorem provides a convenient test for the equivalence of two matrices. If $U = S_1S_2^{-1}$ is an integer matrix of determinant ±1, then the structures are equivalent. The theorem gives a quick way to test if a structure has a particular point group symmetry.

Let R be a rotation matrix with det R = 1, and let M denote a mirror reflection so det M = -1. (Below we will show how to generate these matrices for nonorthogonal coordinate systems.) The matrices $\rho = SRS^{-1}$ and $\mu = SMS^{-1}$ have determinants of +1 and -1, respectively. If ρ is an integer matrix, then the structure S is equivalent to the structure SR. In other words S has the rotation specified by R as a symmetry element. Similarly, if μ is an integer matrix, then S has mirror symmetry. These symmetries are illustrated in Figure 2.

In order to specify the matrices R and M, we need to know the matrix representing the substrate Bravais lattice in terms of the natural Cartesian coordinate system of R^2. The matrix T gives the change of basis from the substrate lattice to R^2. Table 1 lists T matrices for the five types of Bravais lattices. If r is the rotation matrix in Cartesian coordinates,

$$r = \begin{bmatrix} \cos\varphi & \sin\varphi \\ -\sin\varphi & \cos\varphi \end{bmatrix}, \tag{5}$$

then the rotation in terms of the substrate lattice is (10)

$$R = TrT^{-1}. \tag{6}$$

Similarly, reflection in the x-axis is given by

$$m = \begin{bmatrix} 1 & 0 \\ 0 & -1 \end{bmatrix}, \tag{7}$$

so a general reflection about an oblique axis is

$$M = RmR^{-1}. \tag{8}$$

On a hexagonal lattice, for example

$$R = \begin{bmatrix} 1 & 1 \\ -1 & 1 \end{bmatrix}, \tag{9}$$

for a rotation by $\varphi = \pi/3$. The six mirror planes are obtained by rotating m through $\varphi = \pi/6$.

Algebraically, the set of matrices we have been considering has a rich structure. The set of structure matrices, reciprocal matrices and their products constitute the multiplicative group of nonsingular matrices with rational entries, $\mathcal{S}$. In n dimensions the nonsingular n x n rational matrices form a group. To show this, we need to establish that there is an identity element I with IS = SI, that the set is closed under multiplication, and that for any element S, its inverse is also in the set. The first two requirements are trivially verified, while for the third we rely on S^{-1} = (adj S)/det S, where the adjoint is formed by replacing each element in S by its cofactor and transposing the resulting matrix (11). Hence, if S is a rational matrix, so is adj S; and for nonsingular S, det S will be a nonzero rational number, and S^{-1} is seen to be a nonsingular rational matrix.

The set of integer matrices with determinants of ±1, $\mathcal{U}$, form a subgroup of $\mathcal{S}$. The importance of these observations is that we can now make use of the algebraic concept of coset. The left coset of $\mathcal{U}$ by S is the set $S\mathcal{U} = \{SU|U \in \mathcal{U}\}$, and we see that our definition of equivalence amounts to saying that that structure matrices are equivalent if they are members of the same left coset. The set of all left cosets of $\mathcal{U}$ is written as $\mathcal{S}/\mathcal{U}$ (read "$\mathcal{S}$ mod $\mathcal{U}$"). We can make use of the theorem that $\mathcal{S}/\mathcal{U}$ is a partition of S and that two elements S_1 and S_2 of $\mathcal{S}$ are equivalent if and only if $S_1^{-1}S_2 \in \mathcal{U}$ (12). This is exactly the content of our theorem. Finally, note that a method for constructing all integer matrices U with integer inverses has been proposed by Hanson (13).

3. Unscrambling LEED Patterns

If we apply the symmetry operations of the substrate to the surface lattice, we will generate the lattices for all the equivalent domains. Only operations that are not symmetries of the surface produce new lattices. When the domains are much larger than the coherence area of the instrument, the LEED pattern for a simply related overlayer consists of the superposition of the reciprocal lattices of the domains. We would like to

decompose such a pattern into its component Bravais lattices and, if the pattern is not completely known, supply the missing spots as part of the analysis. The algorithm described here will generate an interpretation for the pattern, but, as is discussed in the next section, this may not be the only one possible.

Since the symmetry of the substrate is known, we need only find one of the surface reciprocal Bravais lattices in order to generate all of them. This means that we must find the two unit vectors for one of these lattices. A *simple unit vector* is defined to be any vector from an integral order spot to another spot on the pattern that does not pass through a third spot, as in Figure 3. A vector constructed according to this definition is a unit vector for the surface reciprocal lattice since any line between two spots in a single Bravais lattice, which does not pass through a third spot in the lattice, can be chosen as a unit vector. Hence, there are two difficulties when drawing vectors on a LEED pattern. The first is that we might connect spots from different domains. This is avoided by choosing an integral order beam as one of the spots because these beams belong to all the (simply related) domains. The vector between an integral order beam and any other spot must belong to a common surface Bravais lattice. The second difficulty is that the vector might intersect a third spot in the lattice. Since a simple unit vector does not pass through any other spots, this problem is avoided completely. As a practical matter, if all the spots in the LEED pattern are not known, a vector that appears to be a simple unit vector actually intersect an invisible spot in its lattice, as illustrated in Figure 4. To minimize this possibility the shortest vector from an integral order beam should be chosen as a trial unit vector.

We still need to find the second unit vector. This is easiest to do by identifying all the points in the LEED pattern that must belong to a single Bravais lattice. We define a *lattice line* $\{v_n\}$ to be the set of points generated by the vector u applied to the origin u_0,

$$v_n = u_0 + n_u \text{ for all } n \in Z. \qquad (10)$$

Again, since the substrate beams belong to all domains, for a given unit vector u there will be lattice lines in the pattern through all of these beams and all of these lines belong to a single domain. In addition to these lattice lines, there may be others that pass only through overlayer spots. These lines can be found by systematically testing each of the fractional order beams within a substrate reciprocal unit cell to see if it can be construed as the origin for a lattice line. There are a finite number of such beams so there is little difficulty in executing procedure. These fractional order lattice lines, however, may belong to two different domains, as shown in Figure 5. In cases where this occurs, the integral order lattice lines belong to both domains. Since the density of points in a lattice line depends on the length of the unit vector used in generating it, another advantage to choosing the shortest available unit vector is that this accounts for the greatest number of spots in the pattern.

In patterns that appear to have many spots missing, the integral order lattice lines should always be filled in since all the points on these lines must be present in the true pattern. Many of the missing elements can be supplied by taking each of the vectors between any of the substrate beams and any other spot as a trial vector (even if it is not a simple unit vector) and constructing all of the integral order lattice lines. Applying the point group symmetry operations of the substrate will generate the lattice lines for other domains and may fill in more of the pattern. Also, the use of translational symmetry should not be overlooked; the same pattern should be made by the fractional order beams within each of the substrate reciprocal unit cells.

The filling in of fractional order lattice lines calls for some judgment since what appears to be a line with many beams missing may actually be the coincidental alignment of spots due to different domains. It is best to err on the side of too few fractional order lines since omissions will become obvious as the unscrambling of the pattern proceeds. Again, the use of symmetry can be helpful. Eventually, all the spots must belong to the

sets of lattice lines produced at this stage, so this is a useful guide for deciding if an apparent fractional order lattice line is really in the pattern.

A second unit vector can be found now by connecting any point on an integral order lattice line with a point on an adjacent lattice line. If the surface domains do not have mirror symmetry, there may be two essentially different ways of doing this, leading to Bravais lattices that are mirror images of each other (e.g., Figure 5). The symmetry operations of the substrate generate the Bravais lattices for all the domains. Together, these must account for all the spots observed in the pattern, thus providing a check on the method.

If some spots remain unaccounted for, then the vectors we have chosen must be integer multiples of the true unit vectors, a situation which can arise if there are many missing spots. The correct unit vectors will often be evident, but at worst we will need only to test a few fractions of our chosen vectors. This is another reason for choosing the shortest vectors possible. If the test vectors become unreasonably short, the possibilities that there are incommensurate overlayers or two structural phases should be considered.

It remains to be shown that the algorithm cannot fail to unscramble a LEED pattern for a simply related surface. Let S be the contravariant reciprocal matrix the columns of which specify the unit vectors of a Bravais lattice. The entire lattice itself is generated by

$$v = Sh \text{ for all } h \in Z^2. \tag{11}$$

Hence if v_1 and v_2 are points in the lattice, so are the integer linear combinations

$$n_1v_1 + n_2v_2 = S(n_1h_1 + n_2h_2) \text{ for all } n_1, n_2 \in Z. \tag{12}$$

Since the substrate beams belong to all domains, all the integral order lattice lines for a single generating vector belong to the same Bravais lattice, and any spots missing from such a line must be part of the true pattern. Hence, the procedure for filling in the

pattern is justified. This also shows that the only uncertainty in picking a trial unit vector is that the one chosen might be a multiple of a true unit vector. When specifying the second unit vector, we need to guarantee that it belongs to the same domain as the first, an objective which is achieved by choosing a trial unit vector connecting lattice lines which are known to be in a single domain.

In summary, a practical algorithm for the unscrambling of LEED patterns is

1. Fill in the missing spots supplied by all the integral order lattice lines that can be constructed.
2. Use the symmetry operations of the substrate to fill in additional lattice lines.
3. Complete the fractional order lattice lines that are clearly in the pattern.
4. Choose the shortest vector from a substrate spot to any other as a trial unit vector and mark the integral order lattice lines accounted for by this vector as belonging to one domain.
5. Indicate that the rotationally equivalent lines belong to other domains.
6. Use the shortest vector between an integral order lattice and an adjacent line for the same domain as a second unit vector.
7. Mark the Bravais lattice generated by the two vectors. Generate the lattices for the other domains.

If any spots remain unaccounted for, one or both of the vectors chosen in steps 4 and 6 will have to be shortened by 1/n, where n is an integer. These steps are illustrated in Figure 6, where a pattern with many missing spots is analyzed.

The algorithm relies heavily on the exact spacing between points in the pattern so the LEED instrument must be aligned carefully to insure that straight lines in reciprocal space do not appear curved on the fluorescent screen. A photographic technique for

establishing the alignment and for verifying the absence of distortions due to residual magnetic fields has been presented previously (14). For complicated surfaces it is useful to use low energies in order to resolve the pattern. It is not necessary to display one entire substrate Brillouin zone since varying the angle of incidence will display different parts of the pattern on the screen. Photographs can be overlapped to piece together the entire pattern. In some cases, it may be advantageous to obtain the pattern at several energies in order to obtain as many spots as possible.

4. Ambiguity in LEED Patterns

Once the LEED pattern has been analyzed into its component domains, we would like to know if the proposed decomposition is unique. We have already seen that a hexagonal (S x S)Rφ° pattern from a hexagonal substrate can always be interpreted in two ways. We will show that this is the only ambiguity where a superposition of several Bravais lattices appears as a single Bravais lattice.

It is instructive to examine how ambiguity arises in the hexagonal case. Throughout this section we will use contravariant matrices. In reciprocal space, rotation through an angle of $\pi/3$ is given by

$$R = \begin{bmatrix} 0 & 1 \\ -1 & 1 \end{bmatrix}. \qquad (13)$$

A reciprocal lattice with a sixfold rotation axis can therefore be represented by a matrix of the form

$$S = [I: R] \begin{bmatrix} a \\ b \end{bmatrix}$$

$$= \begin{bmatrix} a & b \\ b & b-a \end{bmatrix} \text{ for } a, b \in Z. \qquad (14)$$

We will show that the superposition of the LEED patterns from the three rotational domains of

$$T = [I: 2R]\begin{bmatrix} a \\ b \end{bmatrix}$$

$$= \begin{bmatrix} a & 2b \\ b & 2(b-a) \end{bmatrix} \text{ for } a, b \in Z, \tag{15}$$

gives the same spot pattern as S. So, for any 2 x 1 integer vector h there exists an integer vector k with

$$Sh = \begin{cases} Tk, \\ RTk, \text{ or} \\ R^2Tk, \end{cases} \tag{16}$$

and conversely. It is convenient to rearrange the components of the matrix equations into the following:

$$Sh = [h_1I + h_2R] \begin{bmatrix} a \\ b \end{bmatrix}, \tag{17}$$

$$Tk = [k_1I + 2k_2R] \begin{bmatrix} a \\ b \end{bmatrix}, \tag{18}$$

$$RTk = [-2k_2I + (k_1+2k_2)R] \begin{bmatrix} a \\ b \end{bmatrix}, \tag{19}$$

and

$$R^2Tk = [-(k_1+2k_2)I + k_1R] \begin{bmatrix} a \\ b \end{bmatrix}. \tag{20}$$

So for any k in either Equations (18), (19), or (20), there exists a corresponding h. For example, in Equation (19), $h_1 = -2k_2$ and $h_2 = k_1 + 2k_2$. To demonstrate the converse, we consider the components of h modulo 2. If h_1 is odd and h_2 is even, then we use Equation (18) with $k_1 = h_1$ and $k_2 = h_2/2$. The four possible cases are listed in Table 2. Hence, the domains of T give exactly the same pattern as S.

Having shown that lack of uniqueness is possible, we can now ask if other types of ambiguity can be found. The vectors

$$h_1 = \begin{bmatrix} 1 \\ 0 \end{bmatrix}, h_2 = \begin{bmatrix} 0 \\ 1 \end{bmatrix}, h_3 = \begin{bmatrix} 1 \\ 1 \end{bmatrix}, h_4 = \begin{bmatrix} -1 \\ 1 \end{bmatrix}, \tag{21}$$

play a special role. As shown in Equation (12), if two vectors are in the Bravais lattice for S, then so are all the integer linear combinations. Suppose that the pattern resulting from the superposition of the lattices for the domains represented by T is the same as the pattern produced by S. We will show that the vectors Sh_1, Sh_2 and Sh_3 must belong to different domains of T if S and T are not equivalent. Assume to the contrary that

$$S[h_1\ h_2] = T[k_1\ k_2]. \tag{22}$$

Then

$$I = S^{-1}TK, \tag{23}$$

where $K = [k_1\ k_2]$ and $|\det K| \geq 1$. Any point in the Bravais lattice of T corresponds to some point in the lattice of S, so $|\det T| \geq |\det S|$. Equation (23) implies that $|\det K| = 1$ and $|\det T| = |\det S|$, so that S and T are equivalent, which contradicts our assumption. Since we can construct anyone of h_1, h_2 or h_3 as an integer linear combination of the other two, each of these three vectors must map to a different domain of T. Hence, T must have at least three inequivalent domains. As can be seen from Table 1, the only substrates with sufficient symmetry are the square and hexagonal lattices.

On a square lattice, the point group symmetry operations are rotation by $\pi/2$ and reflection, with

$$R = \begin{bmatrix} 0 & 1 \\ -1 & 0 \end{bmatrix} \text{ and } M = \begin{bmatrix} 1 & 0 \\ 0 & -1 \end{bmatrix}, \tag{24}$$

and there can be four domains given by T, RT, MT and MRT.

Suppose a surface structure has 4m symmetry. The matrix S can be written in one of the following forms:

$$S = \begin{bmatrix} a & 0 \\ 0 & a \end{bmatrix} \text{ or } S = \begin{bmatrix} a & a \\ a & -a \end{bmatrix}. \tag{25}$$

Consider the first form. Suppose there is an oblique reciprocal lattice represented by the matrix T such that the superposition of the patterns for the four domains of T is the same as the pattern from S. Without loss of generality, assume $Sh_1 = Tk_1 = \begin{bmatrix} a \\ 0 \end{bmatrix}$. Now, $Sh_2 = \begin{bmatrix} 0 \\ a \end{bmatrix} = -RSh_1 = -RTk_1$ so h_2 belongs to the domain RT, and we must have $Sh_3 = MTk_3$ or $Sh_3 = RMTk_3$. Assume the first case. Solving for Tk_3,

$$TK = \begin{bmatrix} a & a \\ 0 & -a \end{bmatrix}, \tag{26}$$

where $K = [k_1 \;\; k_3]$. Since $|\det K| \geq 1$, we have $|\det T| \leq a^2$, but $|\det S| = a^2$. Now, there exist vectors l_1 and l_2 with $Th_1 = Sl_1$ and $Th_2 = Sl_2$, so

$$T = SL, \tag{27}$$

where $L = [l_1 \;\; l_2]$. By assumption, S and T are not equivalent, so $|\det L| > 1$, and by implication, $|\det T| \geq 2\,|\det S|$. This contradicts the constraint on det T. The argument generalizes to the other cases, thereby proving that there is no possibility for ambiguity with a 4m overlayer Bravais lattice.

If a lattice has a fourfold rotation axis, it can be represented by a matrix of the form

$$S = [I: R] \begin{bmatrix} a \\ b \end{bmatrix}$$

$$= \begin{bmatrix} a & b \\ b & -a \end{bmatrix} \quad \text{for } a, b \in Z. \tag{28}$$

The vectors h_1, h_2 and h_3 must be assigned to different domains. Assume without loss of generality that there is a k_1 with $Sh_1 = Tk_1$. Now,

$$Sh_2 = RSh_1$$

$$= RTk_1, \tag{29}$$

so h_2 belongs to RT, and h_3 maps to one of the reflected domains. Assuming $Sh_3 = MTk_3$, we obtain

$$TK = \begin{bmatrix} a & a+b \\ b & a-b \end{bmatrix}, \tag{30}$$

and hence $|\det T| \leq |a^2 - 2ab - b^2|$. Here, S does not have mirror symmetry so for any vector h_i there are two possibilities, either $Th_i = Sl_i$ or $Th_i = MSl_i$. Hence, at least two of the vectors h_1, h_2 and h_3 (and therefore all three) belong to one domain of S. As before, this implies that $|\det T| \geq 2|\det S| = 2(a^2 + b^2) \geq 0$. There are two possibilities, depending on the sign of det T:

$$a^2 - 2ab - b^2 \geq 2a^2 + 2b^2 \geq 0$$

and

$$b^2 + 2ab - a^2 \geq 2a^2 + 2b^2 \geq 0, \tag{31}$$

from which we deduce that

$$0 \geq (a + b)^2 + 2b^2$$

or

$$0 \geq 2a^2 + (a - b)^2, \tag{32}$$

respectively. These inequalities only allow for the trivial solution a=b=0, demonstrating that no ambiguity is possible when interpreting the pattern of an overlayer Bravais lattice with a C4 rotation axis.

For a structure with mirror symmetry, we use

$$S = [I:M] \begin{bmatrix} a \\ b \end{bmatrix}, \tag{33}$$

and carry over the previous arguments with slight modifications. The domains are S and RS, so again $|\det T| \geq 2 |\det S|$ and we can derive a contradiction.

The only remaining case for a substrate with a square Bravais lattice is for a structure S with no symmetry. We would like to know if there can be a matrix T where the superposition of the patterns for four domains of T is the same as for the four domains

of S. It appears that apart from the trivial case where T is equivalent to one of the domains of S this ambiguity cannot occur, but no proof has been constructed.

On a substrate with 6m symmetry, there are seven cases to be considered. The overlayer can have any of the symmetries 6m, 6, 2m or 2. It can be shown that the only ambiguities where the superposition of several Bravais lattices is equivalent to one lattice or to the sum of a lattice and its mirror reflection occurs for the previously cited case of overlayers with 6m or 6 symmetries. This leaves three cases involving low symmetry overlayers that cannot be handled by our methods.

For a surface structure with a sixfold rotation axis, the matrix S is given by Equation (14). Again, taking $Sh_1 = Tk_1$ gives $Sh_2 = -RTk_1$ and $Sh_3 = -R^2Tk_1$. This is the hexagonal ambiguity discussed at the beginning of this section. If S has mirror symmetry, then the superposition of patterns from three domains of T will be equivalent to the pattern from S. When the structure does not have mirror symmetry, S has two domains. Here, three rotational domains of T give the same pattern as one of the domains of S, while the reflected domains of T cover the other domain of S. Now, six different domains of a structure T' cannot give the pattern of a 6m structure S since this would require that two domains of T" be equivalent to one domain of T.

Finally, the only remaining case that can be treated here is where the superposition of the patterns from three domains of a 2m structure contains the same spots as the two patterns from a structure with symmetry 6. Again, take $Sh_1 = Tk_1$, which implies that $Sh_2 = -RTk_1$, $Sh_3 = -R^2Tk_1$ and, since T has mirror symmetry, $MSh_1 = Tk_2$, whence

$$TK = [I:M]Sh_1$$

$$= \begin{bmatrix} a & a \\ b & -b \end{bmatrix}, \qquad (34)$$

where $K = [k_1\ k_2]$. This implies $|\det T| \leq |2ab|$, while we also have $|\det T| \geq 2\,|\det S| = 2\,|ab - a^2 - b^2|$. The two possible signs of the product ab give $\pm ab \geq a^2 + b^2 - ab \geq 0$, with the implications that $0 \geq a^2 + b^2$ or $0 \geq (a - b)^2$. The only nontrivial solution, a=b, is not acceptable since it gives S mirror symmetry and $S^{-1}MS = \begin{bmatrix} -1 & 0 \\ 2 & 1 \end{bmatrix}$.

We have shown that ambiguity, where the superposition of the patterns from several domains of one overlayer gives the same pattern as a single domain of a different structure, occurs only on a hexagonal substrate (where the LEED pattern due to an overlayer with 6m symmetry can be interpreted in terms of three independent domains rotated $\pi/3$ with a 2m structure). The superposition of this ambiguity and its mirror reflection (for a structure with symmetry 6 and rotational domains of symmetry 2) constitute the only ambiguity where the LEED pattern of several domains of one structure is the same as that due to two domains of a different overlayer. We have also shown that the only further possibilities which need to be considered are where three or more domains of a low symmetry overlayer produce LEED patterns equivalent to that of three or more domains of another low symmetry structure. No such ambiguities, however, are known.

References

1. D. A. King and D. P. Woodruff, eds., *The Chemical Physics of Solid Surfaces and Heterogeneous Catalysis*, Elsevier, New York (1981), Vol. 1, p. 98. It is incorrectly stated in this reference that ambiguity of the type described here never arises.
2. C.-M. Chan and W. H. Weinberg, J. Chem. Phys. **71,** 2788 (1979).
3. P. A. Thiel, J. T. Yates, Jr. and W. H. Weinberg, Surface Sci. **82,** 22 (1979).
4. D. Dahlgren and J. C. Hemminger, Surface Sci. **109,** L513 (1981).
5. R. L. Park and J. E. Houston, Surface Sci. **18**, 213 (1969).
6. E. D. Williams and W. H. Weinberg, Surface Sci. **82**, 93 (1979).
7. M. K. Debe and D. A. King, Phys. Rev. Letters **39**, 708 (1977).
8. M. K. Debe and D. A. King, Surface Sci. **81**, 193 (1979).
9. R. L. Park and H. H. Madden, Jr., Surface Sci. **11**, 188 (1968).
10. J. E. Houston and R. L. Park, Surface Sci. **21**, 209 (1970).
11. E. D. Nering, *Linear Algebra and Matrix Theory*, Wiley, New York (1970).
12. J. D. Lipson, *Elements of Algebra and Algebraic Computing*, Addison-Wesley, New York (1981).
13. R. Hanson, Two-Year Coll. Math. J. **13**, 18 (1982).
14. A. C. Sobrero and W. H. Weinberg, Rev. Sci. Instrum. **53**, 1566 (1982).

Table Captions

Table 1: The symmetries and structure matrices for the Bravais lattices.

Table 2: Example of ambiguity on a hexagonal substrate. For any integer vector h there is a corresponding integer vector k that satisfies one of Equations (18), (19), or (20), as indicated. If both components of h are even, the spot in the LEED pattern belongs to all three rotational domains of T and each of the k can be used in its corresponding equation.

Table 3: The notation i=j indicates that i domains of S must give the same LEED pattern as the j domains of T for the pattern to be ambiguous. As discussed in the text, the cases with i and j <3 are eliminated. On a 4m substrate, this leaves four cases to be considered, while for a 6m substrate there are seven. Cases where one of i or j is <3 are treated individually.

Table 1. The Five Bravais Lattices

Lattice Type	Symmetry	Structure Matrix T	Conditions
Hexagonal	6m	$\begin{bmatrix} 1 & 0 \\ -1/2 & \sqrt{3}/2 \end{bmatrix}$	
Square	4m	$\begin{bmatrix} 1 & 0 \\ 0 & 1 \end{bmatrix}$	
Rectangular	2mm	$\begin{bmatrix} 1 & 0 \\ 0 & a \end{bmatrix}$	$a > 1$
Centered Rectangular	2mm	$\begin{bmatrix} 1 & 0 \\ 1/2 & a/2 \end{bmatrix}$	$a>1$, $a\neq\sqrt{3}$
Oblique	2	$\begin{bmatrix} 1 & 0 \\ a\cos\varphi & a\sin\varphi \end{bmatrix}$	$a=1$: $\varphi\neq\pi/2,\pi/3,2\pi/3$ $a>1$: $\varphi\neq\pi/2$, $\varphi\neq\tan^{-1}[(4a^2-1)^{1/2}]$

Conditions on a and φ make the lattice types mutually exclusive.

Table 2. Ambiguity on a Hexagonal Substrate

h_1 mod 2	h_2 mod 2	Equations	k_1	k_2
1	1	20	h_2	$-(h_1+h_2)/2$
0	1	19	h_1+h_2	$-h_1/2$
1	0	18	h_1	$h_2/2$
0	0	18,19,20		

Table 3.

4m Substrate.

S	T			
	4m	4	2m	2
4m	1=1	1=2	1=2	1=4
4		2=2	2=2	2=4
2m			2=2	2=4
2				4=4

6m Substrate.

S	T			
	6m	6	2m	2
6m	1=1	1=2	1=3	1=6
6		2=2	2=3	2=6
2m			3=3	3=6
2				6=6

Figure Captions

Figure 1: Three different unit cells for a (1 x 1) structure.

Figure 2: (a) An overlayer with p2mm symmetry. (b) Overlayer with p6 symmetry.

Figure 3: *Solid line:* one of six equivalent simple unit vectors connecting an integral order spot with a fractional order beam. *Dotted line:* apparent simple unit vector connecting two integral order beams.

Figure 4: Missing spot (O) falls on long vector.

Figure 5: Complex LEED pattern resulting from the superposition of diffraction from four domains. Note that spurious fractional order lattice lines (with many missing beams) result if overlayer beams from different domains are connected.

Figure 6: Analysis of an incomplete pattern following the algorithm described in the text. (a) Shortest simple unit vector. (b) Integral order lattice line. (c) Integral order lattice lines through all substrate spots. (d) Superposition of lattice lines from three rotational domains. (e) Complete specification of unit vectors for one domain.

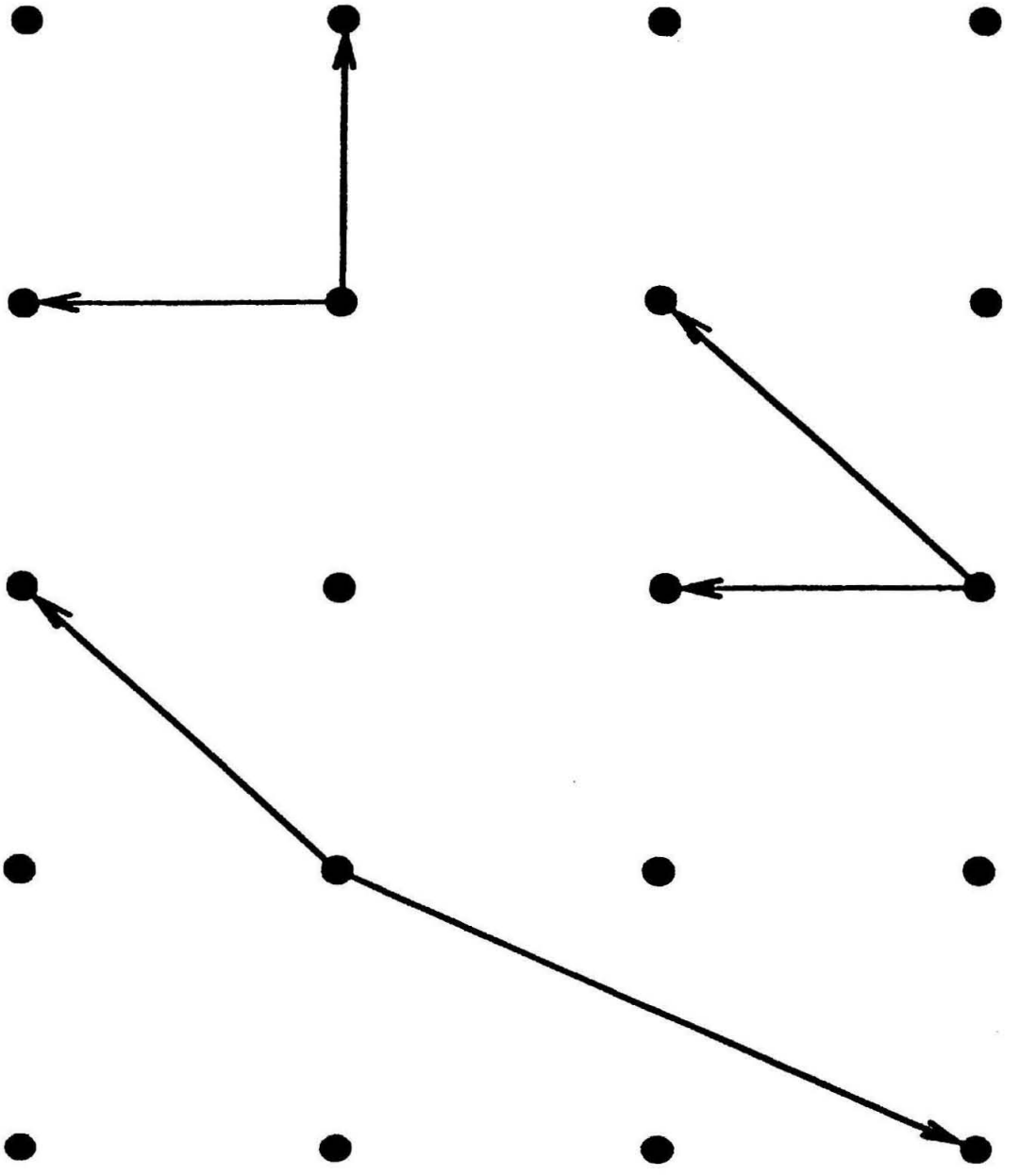

Figure 1

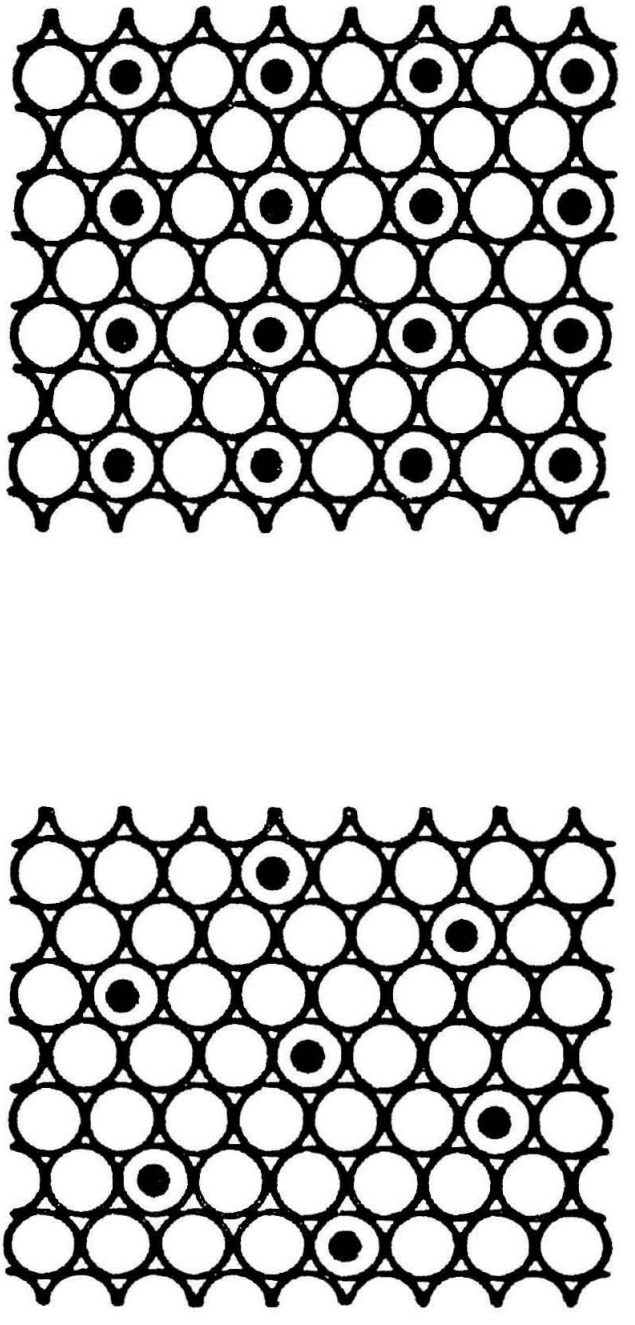

Figure 2

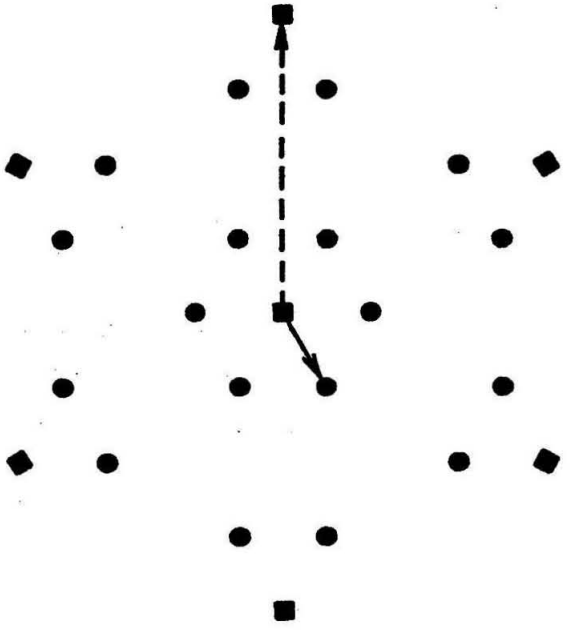

Figure 3

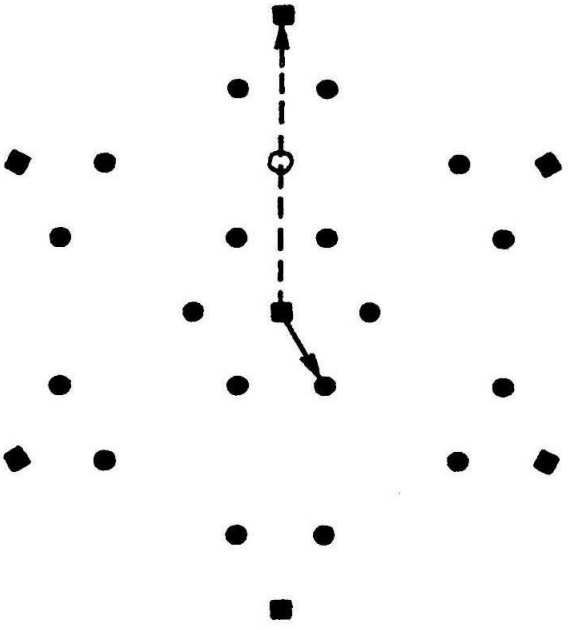

Figure 4

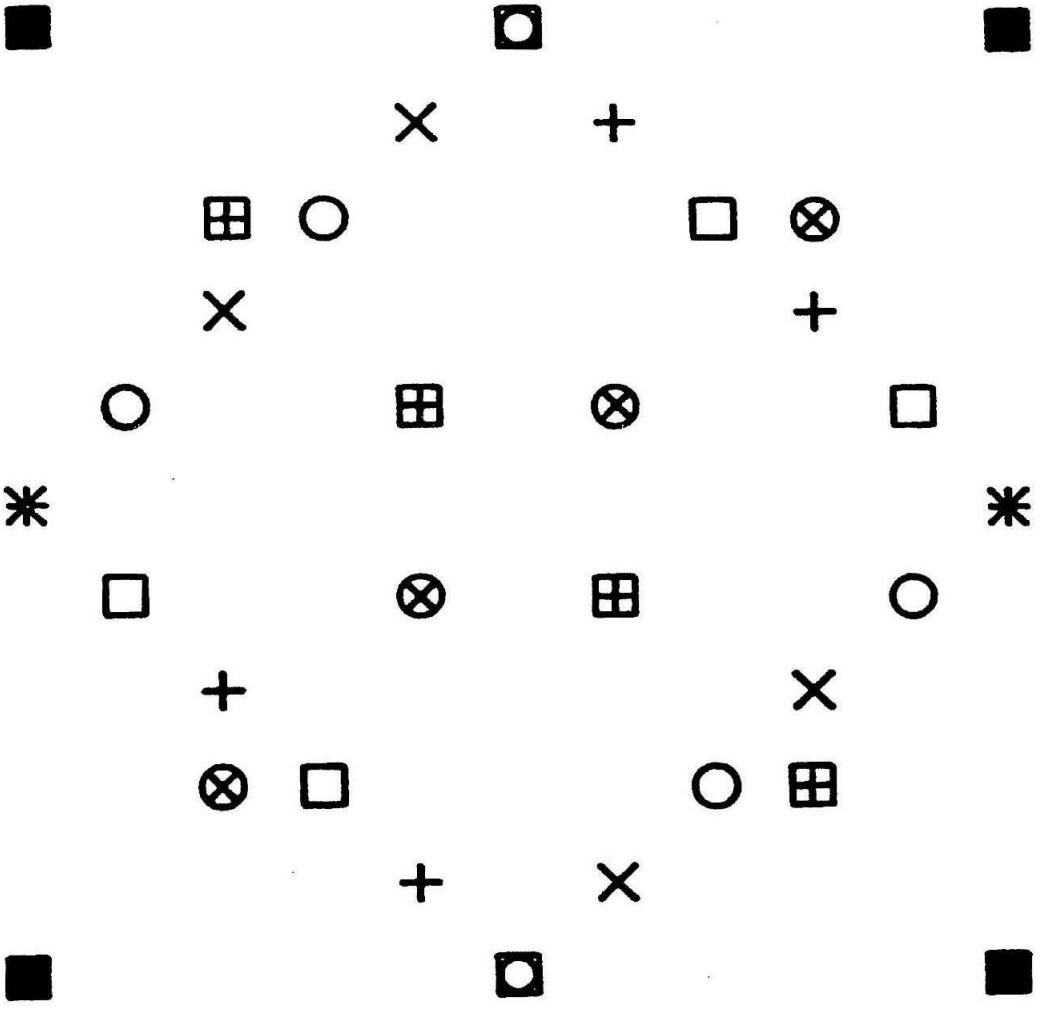

Figure 5

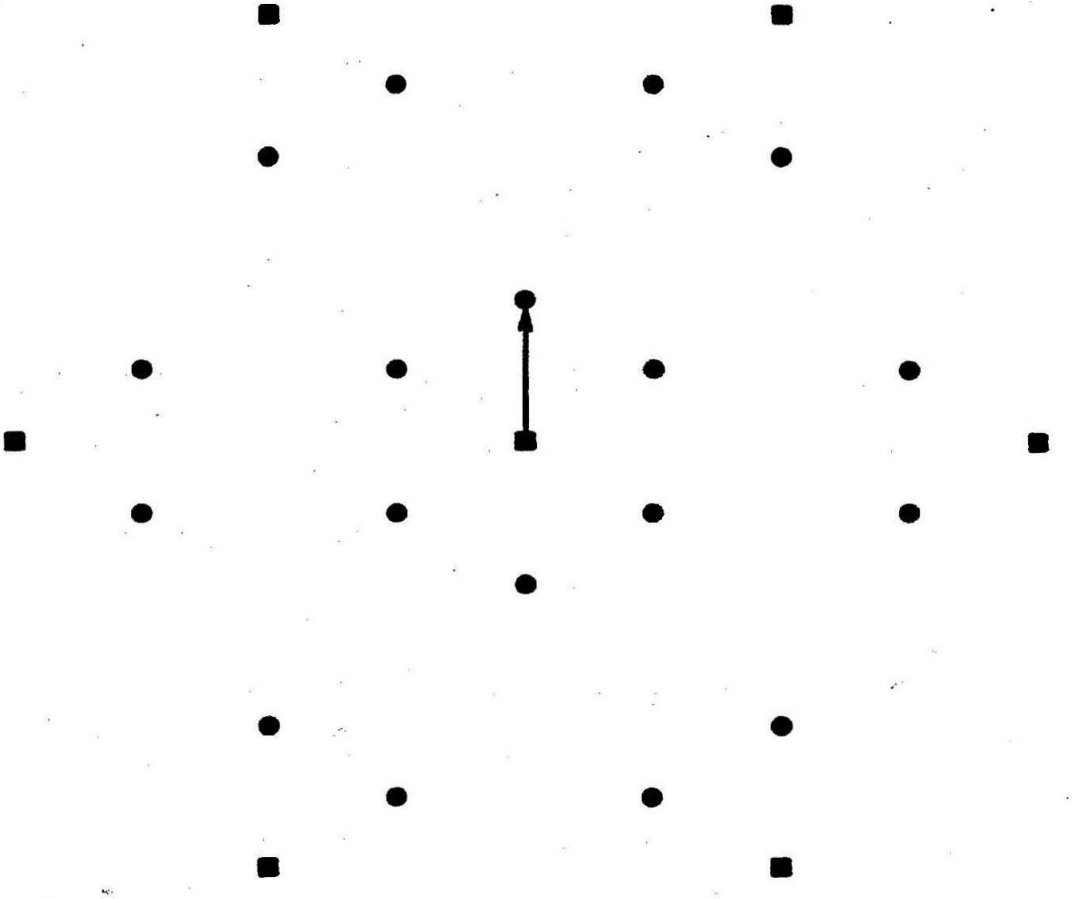

Figure 6a

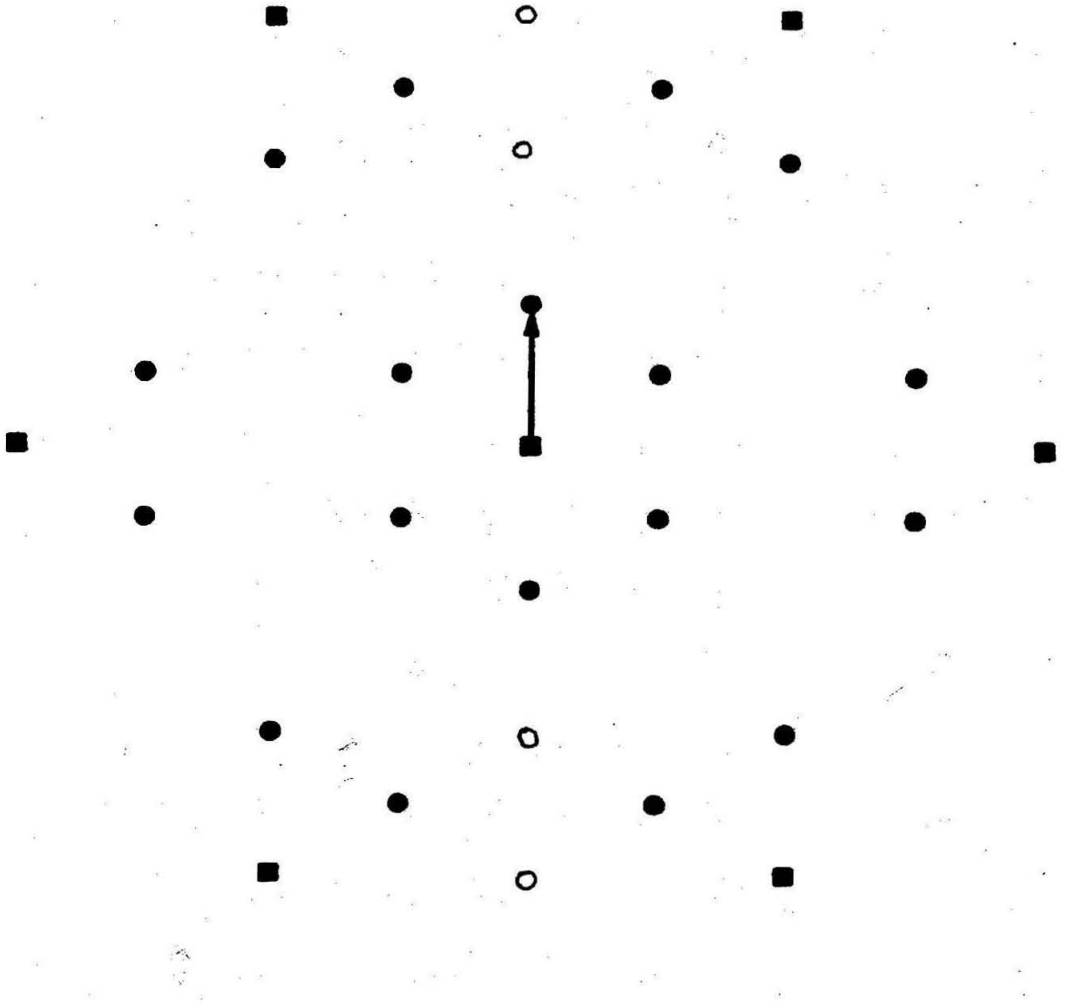

Figure 6b

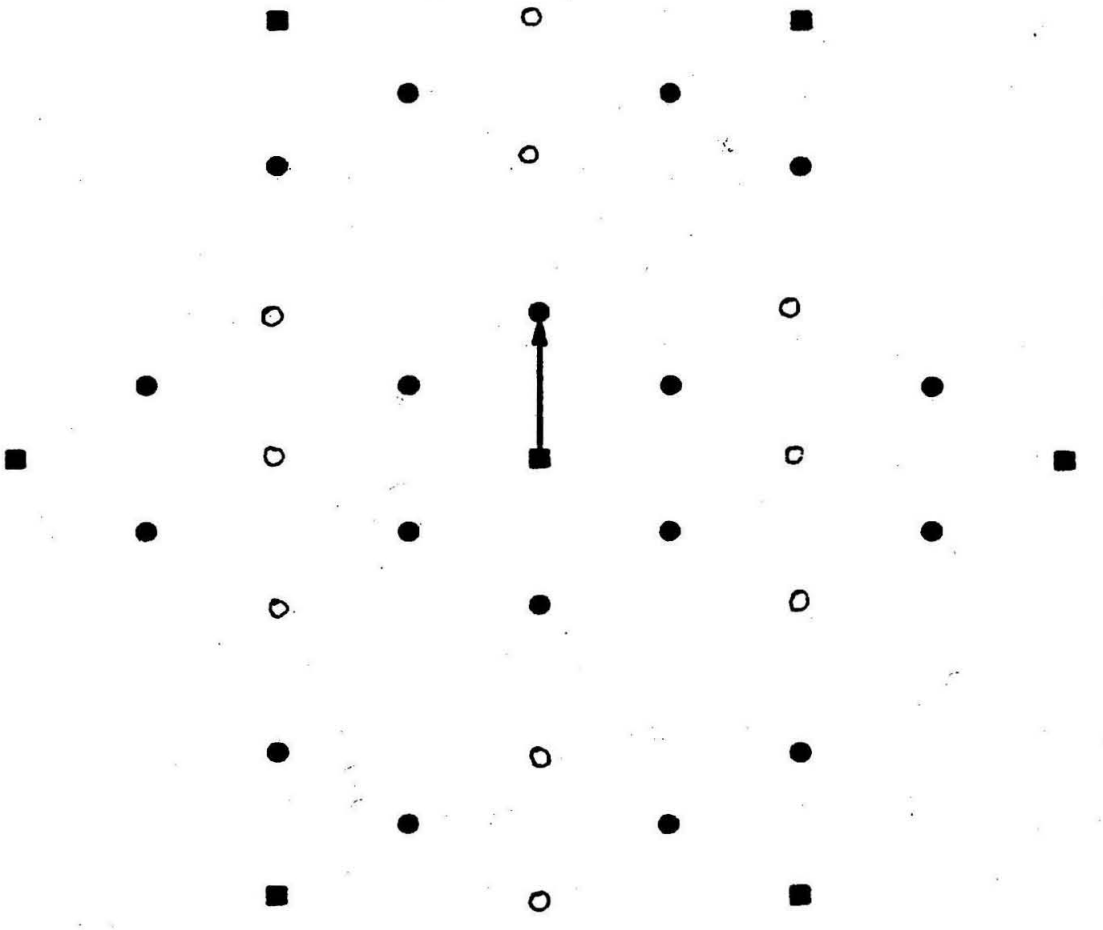

Figure 6c

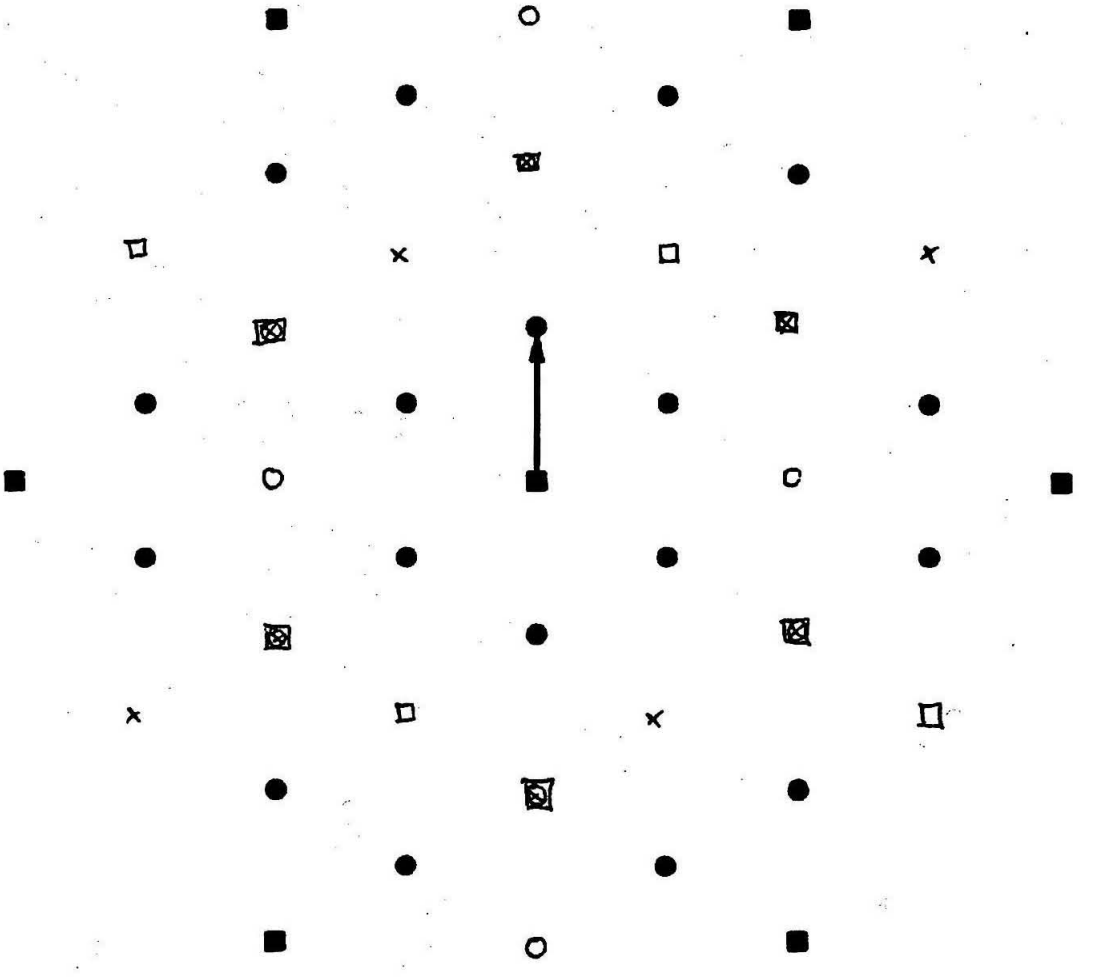

Figure 6d

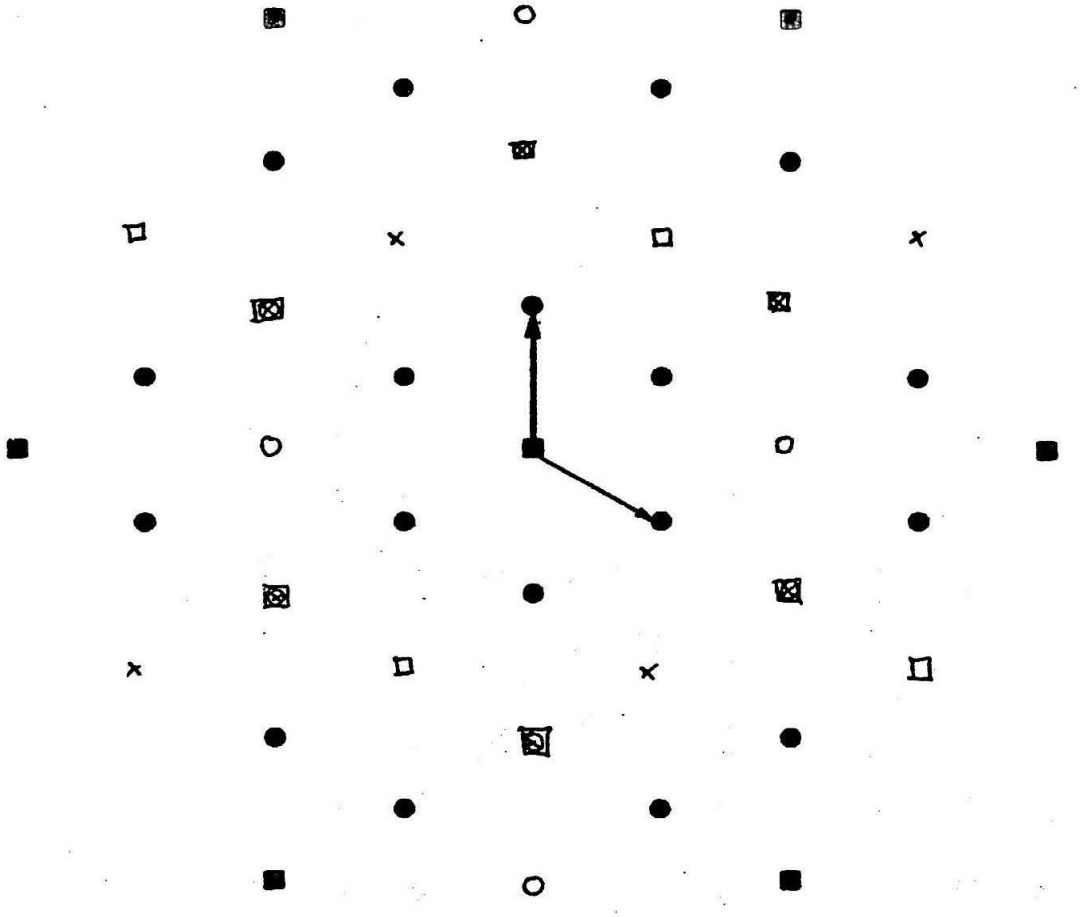

Figure 6e

CHAPTER III

Unified Approach to Photographic Methods for Obtaining the Angles of Incidence in Low-Energy Electron Diffraction

Unified approach to photographic methods for obtaining the angles of incidence in low-energy electron diffraction

A. Charles Sobrero and W. Henry Weinberg

Division of Chemistry and Chemical Engineering, California Institute of Technology, Pasadena, California 91125

(Received 1 October 1981; accepted for publication 14 June 1982)

An equation is developed to describe the geometrical relationships between the electron gun, the crystal surface, and the phosphorescent display screen in back-reflection, post-acceleration LEED experiments. Photographic methods for determining the polar and azimuthal angles of incidence in LEED experiments can be derived starting from this equation. In particular, two published procedures appear here as special cases. New methods are described for cases where the existing techniques do not apply. It is shown that the alignment of the electron gun and the positioning of the crystal can be checked using a photographic technique. An example illustrates that the angles of incidence can be measured with precisions of $\pm 0.2°$ by recording data on several photographs taken over a wide range in electron energy.

PACS numbers: 61.14.Fe

INTRODUCTION

Accurate measurements of the polar and azimuthal angles of incidence are essential for the acquisition and analysis of low-energy electron diffraction (LEED) intensity data.[1] Both the study of surface resonances[2] and the determination of surface structure[3] require the angles of incidence as inputs for the computation of intensity spectra, while the acquisition of experimental data in the form of rotation diagrams[4] and constant momentum transfer averages[5] also depends fundamentally on knowledge of these angles. Since the LEED intensity can be sensitive to variations as small as 0.1°, the measurement of the angles must be quite accurate.

The photographic methods for obtaining the angles of incidence are easy to use and can achieve precisions of better than ±0.2°; this compares favorably with the mechanical techniques.[6] Under appropriate conditions, the position of only one spot on a photograph of the diffraction pattern can determine the angles, and it is easy to increase the precision of the measurement by recording more spots, perhaps using several photographs taken at different electron energies. Additionally, when the angles are overdetermined, statistical analysis can provide estimates of the precision and some indication of the accuracy of the measurements. In contrast, with the mechanical methods, a single datum determines the angles and the accuracy of the measurement relies on the alignment between electrical and mechanical components of the LEED apparatus.

The photographic techniques have several further advantages. These methods can be applied whenever a phosphorescent screen is used to display the diffraction pattern, and no special equipment other than a camera is needed.[7] The photographic procedures are simple to automate, thus facilitating the acquisition of rotation diagrams and constant momentum transfer data.[8] Finally, photographic methods can also be used to check items such as the position of the crystal relative to the LEED screen, the alignment of the electron gun, or the work function compensation applied to the electron gun voltage.[9]

Currently, there are two techniques for obtaining the angles of incidence from the information available on a photograph of the LEED pattern.[7,9] These methods appear to be quite different, and indeed they were intended to complement each other. One procedure, due to Cunningham and Weinberg,[7] can be applied only when the electron gun is collinear with the axis of the camera. The equation which determines the angles of incidence from the data is nonlinear and requires an iterative solution. On the other hand, the method of Price[9] can be used when the electron gun does not point at the camera, but the crystal must be positioned precisely at the center of curvature of the LEED screen. For this case, the equation is linear and only a (3×3) matrix inversion is needed. Both methods require that the incident electron beam be aligned with the center of curvature of the LEED screen. Unfortunately, there are instances when neither technique is appropriate, e.g., if large angles of incidence must be used while the crystal may be off-center, or in any situation where the electron gun may be misaligned.

The approach adopted in this work unifies and extends the existing photographic methods. Section I presents an equation which relates the data on a photograph to the angles of incidence. In Sec. II, we show that the two published techniques can be derived from this equation, and we describe how new procedures may be formulated. Section III contains examples demonstrating the use of two photographic techniques.

I. THEORY

The basis for the photographic methods is that the diffraction pattern on the display screen is a simple trans-

 0034-6748/82/101566-07$01.30

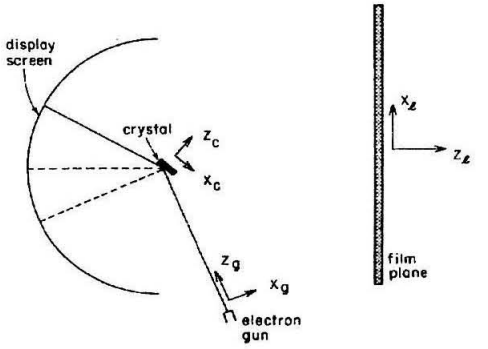

FIG. 1. Schematic of a LEED apparatus showing the reference frames associated with the important components of the equipment. The subscripts *c*, *g*, and *l* denote the crystal, electron gun, and laboratory coordinate systems, respectively.

formation of the two-dimensional reciprocal lattice of the surface.[10] When the point of incidence on the crystal and the center of curvature of the screen coincide, the transformation is an affine mapping. Improper positioning of the crystal or misalignment of the gun introduces a nonlinear magnification factor which distorts the affine relationship and produces a curved image of the reciprocal lattice on the screen.

The geometrical description of diffraction[11] provides the connection between the image on the screen, which represents reciprocal space, and the real space lattice. In reciprocal space, an electron beam is regarded as an infinitely wide, monoenergetic plane wave characterized by the wave vector **k**. Scattering from a perfect, infinite surface adds reciprocal lattice vectors to the wave vector for the incident beam. On the other hand, when viewed on the screen, an electron beam (idealized as having zero width) is represented by the real vector **r**. The crystal surface is a plane of point scatterers arranged in a two-dimensional real lattice.

Since the real and reciprocal spaces are dual to each other,[12] the geometrical description consists of superimposing these two structures on a single vector space.[13] Then, the vectors **k** and **r** describing an electron beam are related by a scale factor F with units of area, i.e., $\mathbf{r} = F\mathbf{k}$. This procedure is possible because on a microscopic scale the transfer width of the instrument is wide ($\sim 10^4$ wavelengths),[14,15] while on a macroscopic scale the electron beams are narrow (~ 1 mm in diameter). In practice, instrumental broadening due to the width of the beams in real space, as well as the angular and energy spread of the wave vectors **k**, limit the precision of the angle measurement.[7]

To specify the components of **k** and **r**, it is necessary to impose a coordinate system on the vector space. As depicted in Fig. 1, for reciprocal space vectors, the geometrical description of LEED gives rise to individual reference frames associated with the electron gun, the crystal surface, and the film. It is convenient to use right-handed orthonormal bases, placing the origins of the three coordinate systems at the point of incidence on the crystal surface. The laboratory coordinate system has the Z_l axis perpendicular to the film plane pointing away from the screen with the X_l and Y_l directions chosen to form an orthogonal coordinate system. The crystal frame has the Z_c axis normal to the surface pointing into the bulk of the crystal, while the X_c axis lies parallel to one of the unit vectors of the surface reciprocal lattice. In the gun coordinate system, the Z_g axis points along the incident beam, with X_g chosen so that the specular beam lies in the second or third quadrant of the X_gZ_g plane. It is not necessary that the (00) spot appear on the screen. At normal incidence the angle φ is defined to be zero and X_g can be any direction perpendicular to Z_g.

Ideally, the point of incidence coincides with the screen center, but it is difficult to achieve exact alignment. For a misaligned instrument, we place the origin of real space at the center of curvature. There are two reasons for this choice. With the origin at the screen center, the vectors representing the diffraction spots, $\mathbf{r}(hk)$, all have the same length; in fact, $|\mathbf{r}| = \rho$, where ρ is the radius of curvature. Furthermore, the image of this origin is simple to locate on a photograph: Fig. 2 shows the plane containing the point of incidence A, the center of curvature B, and the (hk) diffraction spot. The points p_0 and p_1 on the film are projections along the Z_l direction of B and A, respectively. In order to use the point of incidence as the origin for real space, we would need to establish the location of p_1. On systems employing transparent LEED screens,[16] this may be feasible, but in general only p_0 can be located directly. This is because the edge of the screen is a circle defined by the intersection of the spherical surface of the screen with a plane. The projected image of this circle is an ellipse, and the intersection of the major and minor axes of the ellipse is the point p_0. All real space vectors will be specified in the l' frame, which is a translation of the laboratory coordinate system from A to B.

The vector from the point of incidence to the (hk) spot on the display is the real space equivalent of the scattered wave vector $\mathbf{k}_l^s$,

$$\mathbf{r} = F\mathbf{k}_l^s + \mathbf{e}, \tag{1}$$

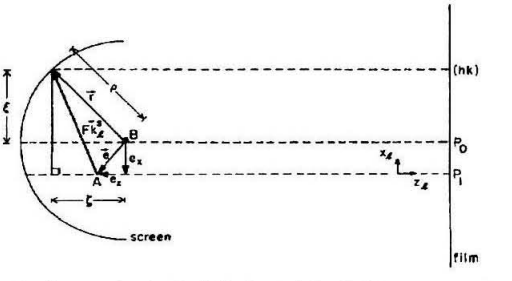

FIG. 2. Cross section in the X_lZ_l plane of the LEED apparatus. The diagram depicts a situation where the point of incidence *A*, center of curvature of the screen *B*, and the (hk) spot on the screen all lie in the X_lZ_l plane. The notation is described in the text.

where the vector e, extending from B to A, measures the alignment error in the instrument. (For simplicity, in Fig. 2 there is no error in the Y_l direction and the optical magnification of the camera, M, is unity.) When e is zero, the scale factor is a constant, $F = \rho/k$, where $k = (2mE/\hbar^2)^{1/2}$ is the magnitude of the wave vectors, E is the electron energy relative to vacuum zero, m is the electron rest mass, and $\hbar$ is Planck's constant divided by 2π. In general, however,

$$F = \frac{|\mathbf{r} - \mathbf{e}|}{k} \tag{2}$$

so for $\mathbf{e} \neq 0$, the factor F depends nonlinearly on r, and the duality of the real and reciprocal spaces is lifted. This means that the scale factor may differ even between diffraction spots on a single photograph. In fact, if the error in positioning is sufficiently great, the dependence of F on r leads to a discernible distortion of the LEED pattern.

Define the components in l' of the magnified vector $M\mathbf{r}$ to be ξ, η, and ζ. The only quantities which can be obtained from a photograph of the LEED pattern are ξ and η, so the angle determination problem becomes a question of extracting Θ and Φ from these measurements. By construction, the length of $M\mathbf{r}$ is equal to ρM, hence,

$$\zeta = -[(\rho M)^2 - \xi^2 - \eta^2]^{1/2}. \tag{3}$$

If either the radius or the magnification cannot be ascertained, the ζ component may be left as an unknown to be determined by the analysis.

The angles of incidence are defined between the crystal and gun reference frames, as shown in Fig. 3. Specifically, the polar angle Θ is the angle from the Z_c direction to Z_g (measured in the X_gZ_g plane), while the azimuth Φ is the angle between X_c and the projection of X_g along Z_c onto the surface plane.[10] The domains are restricted to $0 \leq \Theta \leq \pi/2$ and $-\pi/n < \Phi \leq \pi/n$ for a Bravais lattice with n-fold rotational symmetry. The orthogonal matrices S and T transform the coordinates of a wave vector from the crystal reference frame to those of the gun frame according to

$$\mathbf{k}_g = \mathbf{S}\mathbf{T}\mathbf{k}_c, \tag{4}$$

where

$$\mathbf{S}(\Theta) = \begin{pmatrix} \cos\Theta & 0 & -\sin\Theta \\ 0 & 1 & 0 \\ \sin\Theta & 0 & \cos\Theta \end{pmatrix}, \tag{5}$$

and

$$\mathbf{T}(\Phi) = \begin{pmatrix} \cos\Phi & -\sin\Phi & 0 \\ \sin\Phi & \cos\Phi & 0 \\ 0 & 0 & 1 \end{pmatrix}. \tag{6}$$

Similarly, the angles Θ_l and Φ_l which relate the gun and laboratory reference frames determine the matrix R, with

$$\mathbf{k}_l = \mathbf{R}\mathbf{k}_g. \tag{7}$$

Using the rotation matrices, the incident wave vector measured in the gun coordinate system can be related to the scattered wave in the laboratory frame. If $\mathbf{k}_c^i$ is the incident wave vector in the crystal frame, then the scattered wave vector for the (hk) diffraction beam is given by

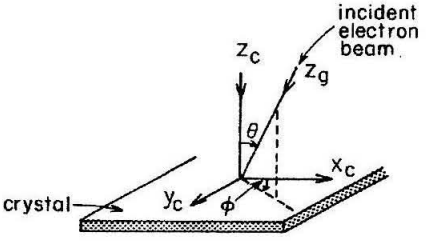

FIG. 3. Detail of the crystal reference frame. The relationship between the gun and crystal reference frames determines the angles of incidence Θ and Φ.

$$\mathbf{k}_c^s(hk) = \mathbf{k}_c^i + \mathbf{g}_c(hk), \tag{8}$$

where the $g_{cx}(hk)$ and $g_{cy}(hk)$ components of the reciprocal lattice vector are obtained from

$$\mathbf{g}_c = \mathbf{U}\begin{pmatrix} h \\ k \\ g_{cz} \end{pmatrix}. \tag{9}$$

Here U is the matrix containing the two-dimensional reciprocal lattice unit vectors and $g_{cz}(hk)$ is determined by the condition for elastic diffraction,

$$\mathbf{0} = (2\mathbf{k}_c^i + \mathbf{g}_c)^T\mathbf{g}_c. \tag{10}$$

In the gun coordinate system, the incident wave vector is $\mathbf{k}_g^i = (0\ 0\ k)^T$, so Eq. (8) is transformed to laboratory coordinates as

$$\mathbf{k}_l^s = \mathbf{R}\mathbf{k}_g^i + \mathbf{R}\mathbf{S}\mathbf{T}\mathbf{g}_c. \tag{11}$$

Combining these results, Eq. (1) becomes

$$\begin{pmatrix} \xi \\ \eta \\ \zeta \end{pmatrix} = M\mathbf{r} = MF(E; hk) \times \mathbf{R}[\mathbf{k}_g^i(E) + \mathbf{S}(\Theta)\mathbf{T}(\Phi)\mathbf{g}_c(E; hk)] + M\mathbf{e}, \tag{12}$$

where some functional dependences have been indicated explicitly. This notation obscures the fact that only the z components k_{gz}^i and g_{cz} of the vectors $\mathbf{k}_g^i$ and $\mathbf{g}_c$ depend on E. Equation (12) is the desired relationship between the angles of incidence and the information available from a photograph, $\xi(E; hk)$ and $\eta(E; hk)$. For each spot, Eq. (12) represents three equations in 14 independent variables: the components of the reciprocal lattice vector, g_{cx} and g_{cy}; the components ξ and η of the spot vector; the angles of incidence Θ and Φ; the angles Θ_l and Φ_l; the components e_x, e_y, and e_z of the error vector; the energy E; the optical magnification M; and the radius of curvature ρ. The usual situation is that ξ and η are measured from a photograph recorded at a known E, while g_{cx}, g_{cy}, M, and ρ are known *a priori*. This leaves three independent equations in seven unknowns, so a general method for determining the angles of incidence requires data from a minimum of three spots. Moreover, for the common

case where the electron gun position cannot be changed, the angles Θ_I and φ_I are fixed and only five unknowns remain.

II. ANGLE DETERMINATION

In order to simplify the analysis, the published angle determination methods[7,9] assume that some or all of the components of the error vector **e** are zero. This assumption may be justified if the LEED instrument is aligned carefully since the elimination of unnecessary parameters decreases the uncertainty in fitting the unknowns. On the other hand, determining **e** directly from Eq. (12) can be useful when checking the alignment of the apparatus.[17] The X_g and Y_g components of **e** (in the gun frame) give the error in the gun position, while the Z_c component gives the amount by which the crystal is incorrectly positioned.

Section II A presents a linear technique for determining the angles of incidence, while a modified version of the method of Price[9] is derived in Sec. II B. In Sec. II C, Gauss–Newton optimization is used to fit the parameters in the equation used by Cunningham and Weinberg.[7]

A. A simple linear method

A straightforward procedure for obtaining the angles of incidence can be developed if the vector $M\mathbf{e}$ and the matrix **R** are known. A common case is when the film plane is perpendicular to the primary electron beam so that **R** can be taken as the identity matrix. Transposing **S** in Eq. (12) yields

$$\mathbf{T}\mathbf{g}_c = \mathbf{g}_p = \mathbf{S}^T\mathbf{R}^T\mathbf{g}_I = \mathbf{S}^T\mathbf{g}_g, \tag{13}$$

where the components of $\mathbf{g}_I = (\mathbf{k}_I^s - \mathbf{k}_I^i)$ are

$$g_{Ix} = \frac{\xi - Me_x}{MF}, \quad g_{Iy} = \frac{\eta - Me_y}{MF},$$
$$g_{Iz} = \frac{\zeta - Me_z}{MF} - k. \tag{14}$$

For **R** known, take $\mathbf{g}_g = \mathbf{R}^T\mathbf{g}_I$. The x and y components of Eq. (13) give

$$g_{px} = g_{cx}\cos\varphi - g_{cy}\sin\varphi = g_{gx}\cos\Theta + g_{gz}\sin\Theta, \tag{15}$$

$$g_{py} = g_{cx}\sin\varphi + g_{cy}\cos\varphi = g_{gy}. \tag{16}$$

Equation (16) can be solved for the azimuthal angle,

$$\varphi = \sin^{-1}\left(\frac{\langle\eta - Me_y\rangle}{M(\langle Fg_{cx}\rangle^2 + \langle Fg_{cy}\rangle^2)^{1/2}}\right) - \tan^{-1}\left(\frac{\langle Fg_{cy}\rangle}{\langle Fg_{cx}\rangle}\right), \tag{17}$$

where the brackets $\langle\ \rangle$ denote the averaged quantities when data from several spots are used. Once φ is known, the polar angle is obtained from Eq. (15),

$$\Theta = \sin^{-1}\left(\frac{\langle g_{px}\rangle}{(\langle g_{gx}\rangle^2 + \langle g_{gz}\rangle^2)^{1/2}}\right) - \tan^{-1}\left(\frac{\langle g_{gx}\rangle}{\langle g_{gz}\rangle}\right). \tag{18}$$

Alternatively, Eqs. (17) and (18) can be solved for each spot individually, and the values averaged to give $\langle\varphi\rangle$ and $\langle\Theta\rangle$. The former procedure is preferable since the mean of the measurement errors in $\mathbf{g}_I$ is apt to be zero.

B. The method of Price[9]

The technique due to Price is also a linear procedure which requires that the error vector be known, but it can be used even when the matrix **R** is unknown. The matrix product **RST** is generated in the course of computing the angles Θ and φ. The original method assumes that the radius ρ and the factor M are known, while E is determined empirically. To simplify the discussion, however, we will assume that the precise energies (relative to vacuum zero) at which the photographs were taken are known.

First, suppose that the LEED apparatus is aligned perfectly and $\mathbf{e} = \mathbf{0}$. Assume that $n + 1$ spots, not all collinear, are available ($n \geq 3$), and let $M\mathbf{r}_i$ for $i = 0, 1, \ldots, n$ be the measured spot vectors, with the ζ components computed from Eq. (3). To eliminate the $\mathbf{k}_g^i$ term in Eq. (12), take the n differences

$$\mathbf{r}_i' \equiv \mathbf{r}_i - \langle\mathbf{r}\rangle = \mathbf{RST}\mathbf{r}_i'' \quad \text{for} \quad i = 1, 2, \ldots, n, \tag{19}$$

where

$$\mathbf{r}_i'' \equiv (F_i\mathbf{g}_{ci} - \langle F\mathbf{g}_c\rangle) \text{ and } \langle\mathbf{r}\rangle \text{ is the average of the } \mathbf{r}_i\text{'s.}$$

When photographs are recorded at various energies, we introduce the dimensionless variables $x = g_{cx}/k$, $y = g_{cy}/k$, and $z = g_{cz}/k$. Let $\lambda_{1i} = x_i - \langle x\rangle$, $\lambda_{2i} = y_i - \langle y\rangle$, and $\mu_I = z_i - \langle z\rangle$, so that

$$\mathbf{r}_i'' = \rho\begin{pmatrix}\lambda_{1i}\\ \lambda_{2i}\\ \mu_i\end{pmatrix}, \quad \text{for} \quad i = 1, 2, \ldots, n; \tag{20}$$

here the λ_{ji}'s are knowns, while the μ_i's are unknowns. Construct the partitioned $(3 \times n)$ matrices[18]

$$S' = (\mathbf{r}_1'\,\mathbf{r}_2'\cdots\mathbf{r}_n'); \tag{21}$$

$$S'' = (\mathbf{r}_1''\,\mathbf{r}_2''\cdots\mathbf{r}_n''), \tag{22}$$

and note that they are related by $S'' = (\mathbf{RST})^T S'$. The top two rows of the matrix $R = (\mathbf{RST})^T$ are given by the linear regression[19]

$$R = S''(S')^T[S'(S')^T]^{-1}. \tag{23}$$

To find the angles of incidence, compute the vector

$$\langle\mathbf{k}^*\rangle \equiv \begin{pmatrix}\langle x^*\rangle\\ \langle y^*\rangle\\ \langle z^*\rangle\end{pmatrix} = \frac{1}{\rho}R\langle\mathbf{r}\rangle \tag{24}$$

so that

$$\Theta = \sin^{-1}[(\langle x^* - x_i\rangle^2 + \langle y^* - y_i\rangle^2)^{1/2}] \tag{25}$$

and

$$\varphi = -\tan^{-1}\left(\frac{\langle y^* - y_i\rangle}{\langle x^* - x_i\rangle}\right). \tag{26}$$

As before, Eqs. (24–26) can be solved for each spot, and the individual values averaged to obtain $\langle\Theta\rangle$ and $\langle\varphi\rangle$, but the procedure shown here is preferred. The matrix **R** is $R^T\mathbf{T}^T(\varphi)\mathbf{S}^T(\Theta)$.

If **e** is not zero, the definitions of the matrices S' and S'', as well as the vector $\langle \mathbf{k}^* \rangle$, must be modified. The entries in the matrices are given by

$$\mathbf{r}'_i = \frac{\mathbf{r}_i - \mathbf{e}}{|\mathbf{r}_i - \mathbf{e}|} - \left\langle \frac{\mathbf{r} - \mathbf{e}}{|\mathbf{r} - \mathbf{e}|} \right\rangle \quad \text{for} \quad i = 1, 2, \ldots, n \tag{27}$$

$$\mathbf{r}''_i = \begin{pmatrix} \lambda_{1i} \\ \lambda_{2i} \\ \mu_i \end{pmatrix} \tag{28}$$

and Eq. (24) becomes

$$\langle \mathbf{k}^* \rangle = R \left\langle \frac{\mathbf{r}_i - \mathbf{e}}{|\mathbf{r}_i - \mathbf{e}|} \right\rangle . \tag{29}$$

Finally, if only three spots are available ($n = 2$), the angles of incidence can be determined by taking $\mathbf{r}'_1$ and $\mathbf{r}'_2$ as defined in Eq. (19) and using $\mathbf{r}'_3 = \mathbf{r}'_1 \times \mathbf{r}'_2$.[9]

C. The method of Cunningham and Weinberg[7]

The method of Cunningham and Weinberg assumes that the electron gun is positioned so that the incident beam points through the screen center of curvature and is normal to the film plane. Here, the matrix **R** reduces to the identity matrix, while e_x and e_y are zero. The method also assumes that E is given, but e_z is left as an unknown. As with the previous techniques, trivial modifications are needed to handle the cases where e_x and e_y are known ($\neq 0$) and where **R** is known ($\neq \mathbf{I}$).

For $e_z \neq 0$, the problem of nonlinear scaling can be circumvented by taking the ratio of the x and y components of Eq. (12).

$$\frac{\eta(hk)}{\xi(hk)} = \frac{x \sin \varphi + y \cos \varphi}{\cos \Theta(x \cos \varphi - y \sin \varphi) - z \sin \Theta}, \tag{30}$$

where Eq. (10) gives

$$z = -\cos \Theta - [\cos^2 \Theta - 2 \sin \Theta \times (x \cos \varphi - y \sin \varphi) - (x^2 + y^2)]^{1/2}. \tag{31}$$

This result is essentially the same as Eq. (6) of Cunningham and Weinberg, and the angles of incidence may be found using a nonlinear least squares procedure.

Suppose that n spots have been photographed, with $n \geq 2$, and define the n-dimensional column vector

$$\mathbf{f}(\Theta, \varphi) = \begin{pmatrix} f_1(\Theta, \varphi) \\ f_2(\Theta, \varphi) \\ \vdots \\ f_n(\Theta, \varphi) \end{pmatrix}, \tag{32}$$

where the components are

$$f_i(\Theta, \varphi) = \frac{\eta_i}{\xi_i} - \frac{x_i \sin \varphi + y_i \cos \varphi}{\cos \Theta(x_i \cos \varphi - y_i \sin \varphi) - z_i(\Theta, \varphi) \sin \Theta}, \quad i = 1, 2, \ldots, n. \tag{33}$$

The least squares estimates of the angles of incidence are the values of Θ and φ, which minimize the length of the vector $\mathbf{f}(\Theta, \varphi)$, with the ideal case being $\mathbf{f} = \mathbf{0}$. These optimal values, denoted Θ^* and φ^*, can be found using a Gauss–Newton procedure[20] where $\mathbf{f}(\Theta, \varphi)$ is expanded in a Taylor series about some initial values, say Θ_0 and φ_0. Solving a set of linear equations leads to an improved estimate for the angles, Θ_1 and φ_1, and the process is iterated until it converges to Θ^* and φ^*.[18]

Define the vector $\Omega = \begin{pmatrix} \Theta \\ \varphi \end{pmatrix}$. The Taylor series for **f** gives

$$\mathbf{f}(\Omega^*) = \mathbf{f}(\Omega_j) + \mathbf{J}_j(\Omega^* - \Omega_j) + (\text{higher order terms}), \tag{34}$$

where the Jacobian matrix is

$$\mathbf{J}_j = \left(\frac{\partial \mathbf{f}}{\partial \Theta} \quad \frac{\partial \mathbf{f}}{\partial \varphi} \right)\Big|_{\Theta_j, \varphi_j}. \tag{35}$$

Ignoring the higher order terms and setting $\mathbf{f}(\Omega^*) = \mathbf{0}$, the best estimate for Ω^* is $\Omega^* \approx \Omega + \Delta$, where the correction vector is

$$\Delta = -[\mathbf{J}^T\mathbf{J}]^{-1}\mathbf{J}^T\mathbf{f}(\Omega). \tag{36}$$

If the initial value Ω_0 is sufficiently close to Ω^*, then the iteration $\Omega_{j+1} = \Omega_j + \Delta_j$ converges to Ω^*.[18] Good starting values can be obtained by setting $\mathbf{e} = \mathbf{0}$ and using a linear method, such as the one detailed in Sec. IIA, to find the angles Θ_0 and φ_0. For each spot, the least square value for the scale factor is

$$MF = \frac{\xi k_{lx}^s + \eta k_{ly}^s}{(k_{lx}^s)^2 + (k_{ly}^s)^2}, \tag{37}$$

where $\mathbf{k}_l^s$ is given by Eq. (11).

The numerical procedure used here is fast; $(\mathbf{J}^T\mathbf{J})^{-1}$ is a symmetric (2×2) matrix which can be computed from **J** in approximately $3n$ operations, while **J** itself is an analytic function of Θ and φ,

$$\frac{\partial f}{\partial \Theta} = \frac{k_{ly}^s}{(k_{lx}^s)^2}(k_{lz}^s + \alpha^{-1} k_{lx}^s \sin \Theta) \tag{38}$$

and

$$\frac{\partial f}{\partial \varphi} = -\frac{\mathrm{k} x_p}{k_{lx}^s} + \frac{(k_{ly}^s)^2}{(k_{lx}^s)^2}(\sin^2 \Theta \alpha^{-1} - \cos \Theta). \tag{39}$$

Here,

$$x_p = x \cos \varphi - y \sin \varphi \tag{40}$$

and

$$\alpha = [\cos^2 \Theta - 2x_p \sin \Theta - (x^2 + y^2)]^{1/2}. \tag{41}$$

Furthermore, the Jacobian need not be updated at each iteration. With reasonable starting values for the angles, it is sufficient to use $\mathbf{J}_0$ throughout the computation. The correct final Jacobian, however, should be used when estimating the error bounds.

III. NUMERICAL EXAMPLES

To demonstrate the types of results which the photographic methods can achieve, the techniques presented in Secs. II A and II C will be applied to two sets of data.

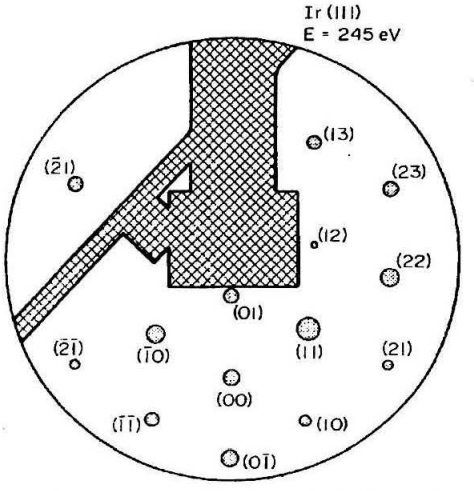

FIG. 4. Drawing of the LEED pattern obtained from Ir(111), after Ref. (7).

The first set consists of a single photograph of the pattern from an Ir(111) surface, while the other set contains five photographs obtained from a Rh(111) surface. A detailed comparison of the two cases indicates that to attain precise results for the angles of incidence, data should be recorded over a wide energy range.

The spot positions in an arbitrary reference frame, ξ_{arb} and η_{arb}, can be measured with a digitizing tablet or by laying a sheet of graph paper over the photograph and marking the spot centers. These data are presented in Tables II and III (p_0 is the center of the image of the screen). To use the photographic methods, measurements in the arbitrary coordinate system must be translated and rotated to the l' frame.

$$\begin{pmatrix}\xi\\ \eta\end{pmatrix} = \begin{pmatrix}\cos\psi & \sin\psi\\ -\sin\psi & \cos\psi\end{pmatrix}\begin{pmatrix}\xi_{arb}-\xi_{p0}\\ \eta_{arb}-\eta_{p0}\end{pmatrix}. \qquad (42)$$

The rotation angle is $\psi = \tan^{-1}[(\eta_{00}-\eta_{p0})/(\xi_{00}-\xi_{p0})]$. [When the specular spot is not on the screen, both the (hk) labeling of the beams and the determination of ψ become difficult.]

Figure 4 is a schematic drawing of the LEED pattern from an Ir(111) surface at $E = 245$ eV. This is the same photograph which was analyzed in Ref. (7). It is evident from the large distortion in the pattern that the crystal was not located at the center of curvature of the screen. Table I shows the parameters needed for the nonlinear procedure of Sec. II C, while the data measured from the photograph are in Table II. The simple linear method provides the initial estimates for the angles: $\Theta = 13.6°$ and $\varphi = 0.3°$. Using the iteration of Eq. (41), the fully converged values are $\Theta = 13.1 \pm 0.1°$ and $\varphi = 0.2 \pm 0.5°$. The uncertainty intervals represent individual 95% confidence regions for the linearized equation.[19] These angles are consistent with the results reported previously,[7] but our confidence limit for φ is significantly wider.

The true magnitude of the uncertainty in Θ and φ can be determined by examining the fit between predicted and observed spot positions. The predicted positions are computed from Eq. (12), assuming e_x and e_y are zero. Table II indicates that the fit is excellent, so the wide confidence intervals cannot be narrowed by slight im-

TABLE I. Input parameters for the method of Sec. II C: Ir(111).

Parameter	Symbol	Value
Electron energy	E	245 eV
Screen radius of curvature	ρ	6.35 cm
Length of reciprocal unit vectors	c	2.67 Å^{-1}
Shear matrix	U	$\begin{bmatrix}\sin 30° & -1\\ \cos 30° & 0\end{bmatrix}$
Initial estimates	Θ_0	13.6°
	φ_0	0.3°

TABLE II. Measured and predicted positions of the spots shown in Fig. 4.

			Measured Values $\Theta = 13.1°$, $\varphi = 0.20°$		Predicted	
hk	g_{cx} (Å^{-1})	g_{cy} (Å^{-1})	ξ (cm)	η (cm)	ξ (cm)	η (cm)
00	0.00	0.00	2.3	0.0	2.30	0.00
01	−2.67	0.00	0.8	0.0	0.80	0.01
0$\bar{1}$	2.67	0.00	3.8	0.1	3.80	0.01
10	1.34	2.31	3.1	1.4	3.05	1.51
$\bar{1}$0	−1.34	−2.31	1.4	−1.5	1.42	−1.48
11	−1.34	2.31	1.4	1.4	1.37	1.43
$\bar{1}$1	1.34	−2.31	3.1	−1.5	3.08	−1.53
21	0.00	4.62	2.0	2.9	2.01	2.89
2$\bar{1}$	0.00	−4.62	2.1	−3.1	2.13	−3.08
12	−4.01	2.31	−0.2	1.4	−0.26	1.39
22	−2.67	4.62	0.3	2.8	0.40	2.79
13	−6.68	2.31	−2.2	1.5	−2.19	1.52
23	−5.34	4.62	−1.3	2.8	−1.30	2.80
2$\bar{1}$	−5.34	−4.62	−1.3	−2.7	−1.28	−2.71
p_0	—	—	0.0	0.0	—	—

TABLE III. Measured spot positions from Rh(111) (arbitrary laboratory coordinate system).

	209 eV		209 eV		270 eV		378 eV		378 eV	
hk	ξ	η	ξ	η	ξ	η	ξ	η	ξ	η
43							111	106	41	53
33					52	59				
23	39	73	35	62						
13	22	72	20	62			32	100		
32	66	59	57	50	58	50	94	80	35	41
1$\bar{2}$					7	48				
31					66	39				
11	38	39								
$\bar{1}$1	4	40	5	35	15	35	7	57		
20	67	28	58	25	60	26	96	38	36	23
10	47	25	42	22	46	25	70	34	26	22
00	30	24	27	22	34	24	45	34	15	22
$\bar{1}$0	13	25	13	22	21	24	21	35	4	21
1$\bar{1}$					54	15	85	16	32	14
0$\bar{1}$	40	10	36	10	41	13	59	15	21	13
$\bar{1}\bar{1}$	23	10	21	10	28	13	33	14	10	13
p_0	35	43	30	36	36	39	51	74	17	37

provements in the precision of the spot position measurements. This point is also illustrated by considering the error sum of squares

$$SSQ = \sum_{(hk)} (\xi_{meas} - \xi_{pred})^2 + (\eta_{meas} - \eta_{pred})^2 \quad (43)$$

as a function of Θ and Φ. The contours are very shallow, indicating that the predicted positions are insensitive to variations of $\pm 0.5°$. Now, SSQ = 0.05 corresponds to an average error of 0.02 cm in the position of the center of each spot, while the spots themselves are 0.2 cm or wider in diameter. Hence, it is not feasible to reduce the uncertainty in the angles by improving the SSQ.

Part of the reason for the insensitivity of the SSQ to variations in Θ and Φ is that Eq. (37) adjusts the factor F to accommodate some of the lack of fit in the spot positions. This factor and the vector component e_z are related by

$$e_z = [(MF\mathrm{k})^2 - (\xi^2 + \eta^2)]^{1/2} - [(\rho M)^2 - (\xi^2 + \eta^2)]^{1/2}. \quad (44)$$

For a single spot, the positioning error e_z appears essentially as an energy error in the z component of the incident wavevector $\mathbf{k}_g^i$. Since the scattered component k_{iz}^s varies by less than 20% across the photograph, the value of e_z cannot be determined very precisely by using position data recorded at one energy. In fact, for a set of (Θ, Φ) points within the SSQ = 0.05 contour, the value $e_z = -1.5 \pm 0.3$ cm was obtained. These considerations indicate that precise measurements require data from several photographs taken over a range of energies (where k_{iz}^s varies by a factor of two or three).

The second data set consists of five photographs taken at E = 209, 270, and 378 eV. As in the previous example, the initial estimates ($\Theta = 12.2°$, $\Phi = 79.5°$) are obtained from the method of Sec. II A. After iterating Eq. (41) seven times, the converged values for the angles are $\Theta = 11.1 \pm 0.1°$ and $\Phi = 79.5 \pm 0.2°$, where again, the precision is estimated from the linearized equations.

In conclusion, it is clear that photographic techniques can provide precise measurements of the angles of incidence. Possible sources of systematic error include residual magnetic fields, optical distortion introduced by the camera, and nonsphericity or warping of the screen. When a large number of spots are recorded over a range of energies, it becomes possible to test for these effects. For this reason it may be useful to form adsorbate overlayers with unit cells larger than the (1×1) substrate unit cell and to use high electron energies, thus increasing the amount of data available per photograph. Finally, it should be noted that no angle determination method based on geometrical ideas can account for the refraction which occurs as the electrons drop from the vacuum potential to the inner potential of the solid. Hence, at low energies or high angles of incidence, it may be necessary to correct the geometric angles for this electronic effect.[21]

ACKNOWLEDGMENT

The support of the Army Research Office under grant No. DAAG29-79-C-0132 is gratefully acknowledged.

[1] W. Berndt, Rev. Sci. Instrum. **53**, 221 (1982).
[2] R. E. Dietz, E. G. McRae, and R. L. Campbell, Phys. Rev. Lett. **45**, 1280 (1980); G. L. Price, P. J. Jennings, P. E. Best, and J. C. L. Cornish, Surf. Sci. **89**, 151 (1979); J. Rundgren and G. Malmström, Phys. Rev. Lett. **38**, 836 (1977).
[3] M. A. Van Hove and S. Y. Tong, *Surface Crystallography by LEED* (Springer, New York, 1979).
[4] R. Feder, Phys. Status Solidi B, **58**, K137 (1973); G. E. Laramore, Phys. Rev. B **6**, 2950 (1972); Groupe d'Etude des Surfaces, Surf. Sci. **48**, 497 (1975).
[5] M. G. Lagally, T. C. Ngoc, and M. B. Webb, Phys. Rev. Lett. **26**, 1557 (1971).
[6] J. Larscheid and J. Kirschner, Rev. Sci. Instrum. **49**, 1486 (1978); J. M. Burkstrand, Rev. Sci. Instrum. **44**, 774 (1973).
[7] S. L. Cunningham and W. H. Weinberg, Rev. Sci. Instrum. **49**, 752 (1978).
[8] J. H. Onuferko and D. P. Woodruff, Surf. Sci. **91**, 400 (1980).
[9] G. L. Price, Rev. Sci. Instrum. **51**, 605 (1980).
[10] J. B. Pendry, *Low-Energy Electron Diffraction* (Academic, New York, 1974).
[11] G. Ertl and J. Küppers, *Low Energy Electrons and Surface Chemistry* (Verlag Chemie, Weinheim, 1974).
[12] R. D. Milne, *Applied Functional Analysis* (Pitman, Boston, 1979).
[13] E. D. Nering, *Linear Algebra and Matrix Theory* (Wiley, New York, 1970).
[14] R. L. Park, J. E. Houston, and D. G. Schreiner, Rev. Sci. Instrum. **42**, 60 (1971).
[15] G. Comsa, Surf. Sci. **81**, 57 (1979).
[16] J. F. Wendelken, S. P. Withrow, and P. S. Herrell, Rev. Sci. Instrum. **51**, 255 (1980).
[17] A. C. Sobrero and W. H. Weinberg (in preparation).
[18] G. Dahlquist and Å. Björck, *Numerical Methods* (Prentice-Hall, Englewood Cliffs, New Jersey, 1974).
[19] N. R. Draper and H. Smith, *Applied Regression Analysis* (Wiley, New York, 1966).
[20] Y. Bard, *Nonlinear Parameter Estimation* (Academic, New York, 1974); P. E. Gill, W. Murray, and M. H. Wright, *Practical Optimization* (Academic, New York, 1981).
[21] P. M. Marcus, F. Jona, S. Finch, and H. Bay, Surf. Sci. **103**, 141 (1981).

Chapter IV

Analysis of the Zanazzi-Jona and Other Reliability Factors for LEED

Analysis of the Zanazzi-Jona and Other Reliability Factors for LEED

A. C. Sobrero* and W. H. Weinberg

Division of Chemistry and Chemical Engineering

California Institute of Technology

Pasadena, California 91125

* Current address: E.I. du Pont de Nemours and Co., Inc.; Wilmington, Delaware 19898; USA.

Abstract

As a means of quantifying the agreement between different sets of intensity spectra, the Zanazzi-Jona R-factor, R_{ZJ}, has served the LEED community well. The single beam R-factor was constructed explicitly to be sensitive to certain features in the intensity spectra while ignoring insignificant differences. Unfortunately, R_{ZJ} is not a metric over the space of intensity spectra and this leads to a number of undesirable properties. The most severe of these are that R_{ZJ} does not satisfy the triangle inequality and that it can be very small or even zero (indicating perfect agreement) for intensity spectra which are significantly different. Reliability factors presented by Pendry, Adams et al., Van Hove et al., and Sobrero and Weinberg as well as the X-ray R-factor are also analyzed.

1. Introduction

In the determination of surface structure by Low-Energy Electron Diffraction (LEED), it is necessary to compare computed intensity spectra for various structural models and pick the set that best agrees with the experimental data. The question naturally arises as to what criteria are to be used in effecting this comparison. Often, as is the case when multilayer relaxations are being studied (1-5), the differences one is trying to measure are rather subtle. One way to examine large amounts of data in a reproducible and quantitative manner is to use a computed reliability factor (or R-factor).

In their seminal paper concerning R-factors (6), Zanazzi and Jona discussed a number of desiderata that such a function should fulfill. They critiqued several possible R-factors for LEED intensity curves, and finally they proposed the widely used Zanazzi-Jona R-factor. The important properties this function possesses are that it is sensitive to: (1) the general shapes of the curves while disregarding the absolute values of the intensities of the two curves being compared and the amount of background; (2) the relative intensities between different sections of the intensity curves; (3) the relative positions of maxima, minima and shoulders; and (4) the presence of peculiarities, such as narrow peaks (6). Other workers have introduced R-factors designed to meet somewhat different criteria (7-13).

Unfortunately, the Zanazzi-Jona R-factor does not satisfy properties (3) or (4) and, unless the background is a piecewise linear function of energy (which it is not), it also fails to have property (1). The violation of property (3) makes the Zanazzi-Jona R-factor in its original form problematic for comparing intensity spectra. In section 2 we analyze the properties of the single beam Zanazzi-Jona R-factor and of various modifications. We show that the null space of R_{ZJ} consists of piecewise linear functions, so curves differing

only by a piecewise linear function will have a single-beam R-factor of zero, indicating perfect agreement between the spectra. This is undesirable since spectra with piecewise linear differences can have peaks shifted by several eV or even different numbers of peaks. Section 3 contains analyses of R-factors due to Pendry (8), Van Hove et al. (7), Adams et al. (5,11,12), Sobrero and Weinberg (13) and the X-ray R-factor (9,16). The five functions introduced in Ref. (7) are not statistically independent so one can expect to find correlations among them. This weakens the argument that only near the true surface structure will the functions have minima simultaneously. Finally, we discuss the issues of variance, sensitivity and information content of intensity spectra and show that R-factors should be averaged in momentum space rather than over the energy variable as is the current universal practice.

2. Analysis of the Zanazzi-Jona R-factor

In this section we review the definition of the Zanazzi-Jona R-factor and show that it has units of eV^{-2}. A dimensionless form of the R-factor is introduced together with a simple function that bounds R_{ZJ}. These functions are modified to make them symmetric with respect to the exchange of their arguments and to attempt to make them satisfy the triangle inequality. In this manner, we show that no function of the form of R_{ZJ} can be a metric for intensity curves or their derived functions.

The definition of the single beam Zanazzi-Jona R-factor is (6)

$$R_{ZJ} = \left[\frac{|A|}{E_f - E_s}\right] \int w(E)\, |cI_{calc}' - I_{obs}'|\, dE, \qquad (1)$$

with

$$c = \frac{\int I_{obs}\, dE}{\int I_{calc}\, dE} \qquad (2)$$

$$w(E) = \frac{|cI_{calc}'' - I_{obs}''|}{|I_{obs}'| + |I_{obs}'|_{max}} \qquad (3)$$

and

$$A = \frac{E_f - E_s}{\int I_{obs}\, dE}\,. \qquad (4)$$

Here, E_s and E_f are, respectively, the start and finish (lowest and highest) energies at which data are available, I_{obs} and I_{calc} are the observed and calculated intensities, and the prime denotes differentiation with respect to the energy, E. This expression can be simplified by introducing the dimensionless variables

$$\varepsilon = \frac{E - E_s}{E_f - E_s} \qquad (5)$$

and

$$i_o(\varepsilon) = \frac{I_{obs}(E)}{\langle I_{obs}\rangle}\;; \qquad i_c(\varepsilon) = \frac{I_{calc}(E)}{\langle I_{calc}\rangle}\,. \qquad (6)$$

In Equations (5) and (6) the averages are

$$\langle I_{obs}\rangle = \frac{\int I_{obs}\, dE}{E_f - E_s}\;; \quad \langle I_{calc}\rangle = \frac{\int I_{calc}\, dE}{E_f - E_s}\,. \qquad (7)$$

With these definitions, Equation (1) becomes

$$R_{ZJ} = \left[\frac{1}{E_f - E_s}\right]^2 \int_0^1 \frac{|i_c'' - i_o''|\,|i_c' - i_o'|\, d\varepsilon}{|i_o'| + |i_o'|_{max}}\,, \qquad (8)$$

where now the prime denotes differentiation by the dimensionless energy, ε. This form shows that the R-factor is not dimensionless and that there is a strong dependence on the length of the energy interval. To eliminate this dependence, define the dimensionless function

$$r(i_o, i_c) = (E_f - E_s)^2\, R_{ZJ}. \qquad (9)$$

The numerator in the integrand of Equation (8) can be written as $|[(i_o' - i_c')^2]'|/2$, and we have finally

$$r = \frac{1}{2} \int_0^1 \frac{|[(d_o - d_c)^2]|' \, d\varepsilon}{|d_o| + |d_o|_{max}} , \tag{10}$$

where $d_n = i_n'$ for n = o, c. This function is essentially the same as the Zanazzi-Jona R-factor, the only modification being the conversion to dimensionless form introduced by Equation (9).

For the purpose of analysis, Equation (10) is somewhat unwieldy. Fortunately, the function r can be bounded by a simpler expression. Since $0 \le |d_o| \le |d_o|_{max}$ the mean value theorem gives the bounds

$$(\sqrt{2}/2)p \le r \le \sqrt{2}p \tag{11}$$

for

$$p = \left[\frac{\sqrt{2}}{4|d_o|_{max}}\right] \int |[(d_o - d_c)^2]|' \, d\varepsilon. \tag{12}$$

Equation (11) is entirely symmetrical since

$$(\sqrt{2}/2)\, r \le p \le \sqrt{2}\, r. \tag{13}$$

Thus, the R-factors r and p are equivalent to within a factor of two. The function p is computationally simpler than r since the integral can be evaluated analytically. This function also eliminates the need for the values of the second derivatives, a welcome benefit in view of the numerical instability of differentiation. To evaluate the integral in Equation (12), define the function

$$\delta(\varepsilon) = (d_o - d_c)^2 \tag{14}$$

and the set of closed intervals

$$\Omega_{-} = \{\varepsilon: \delta'(\varepsilon) \leq 0\}$$

and

$$\Omega_{+} = \{\varepsilon: \delta'(\varepsilon) \geq 0\}. \qquad (15)$$

The zeroes where δ' changes sign are labeled $\varepsilon_1, \varepsilon_2, \ldots, \varepsilon_n$ and belong to both sets. Without loss of generality, assume that the interval $[0, \varepsilon_1] \in \Omega_{+}$ and that $[\varepsilon_n, 1] \in \Omega_{+}$. The other cases can be treated with small modifications. The integral now becomes

$$\tfrac{1}{2} \int_0^1 |\delta'| \, d\varepsilon = \tfrac{1}{2} \left[\int_{+} \delta' \, d\varepsilon - \int_{-} \delta' \, d\varepsilon \right]$$

$$= [\delta(1) - \delta(0)]/2 + \sum \delta(\varepsilon_{2j-1}) - \delta(\varepsilon_{2j}) \qquad (16)$$

a sum involving only the first derivatives of the intensity spectra. The second derivatives still need to be computed to determine the zeros ε_j but, because the points where $\delta' = 0$ are the stationary points of δ, the zeros need not be located with great accuracy.

A minor difficulty with Equations (10) and (12) is that these functions are not symmetric with respect to the exchange or the curves labeled c and o. If one is comparing two sets of experimental data with equal variances (or two sets of computed curves), there is no reason to favor one set over the other. When independent data sets have unequal variances, they should be weighed by the inverse of their respective standard deviations, and thereafter the weighed data sets should be treated equally (14). The functions r and p can be made symmetric by replacing the denominator in the integrands of Equations (10) and (12) with

$$(|i_o'| + |i_o'|_{max} + |i_c'| + |i_c'|_{max})/2 \qquad (17)$$

and

$$(|i_o'|_{max} + |i_c'|_{max})/2 \qquad (18)$$

respectively. The symbols r_s and ρ_s will denote these symmetric versions.

A more substantial difficulty with ρ and r is that even for very similar curves it is possible to violate the triangle inequality. That is, for three curves i_1, i_2 and i_3 it is possible to have a small R-factor between curves i_1 and i_2 or between i_1 and i_3, while the R-factor between curves i_2 and i_3 is nevertheless large, which is undesirable. Say curves i_1 and i_2 are from two experiments, while i_3 is the best-fit computed curve for experiment 1. Since i_1 and i_2 match closely (R-factor small), it stands to reason that the computed curve which fit i_1 well should also fit the data from experiment 2 reasonably well. So, for an R-factor function to be useful, it needs to satisfy the triangle inequality. That this is not so for the functions r or ρ indicates a weakness in their definitions and in R_{ZJ}.

To examine this issue in greater detail, we can construct an example for ρ_s where the triangle inequality is violated. Suppose there are three curves with

$$|i_1'|_{max} = |i_2'|_{max} = |i_3'|_{max} = \sqrt{2}/2 \tag{19}$$

a value chosen so that the constant in Equation (12) drops out. Define the differences

$$\alpha = i_1' - i_2'$$

$$\beta = i_2' - i_3'$$

$$\gamma = i_1' - i_3' = \alpha + \beta \tag{20}$$

and suppose that α and β have the same sign over most or the energy range, and similarly for α' and β'. Qualitatively, this means that the differences between the intensity curves behave the same way. We now have

$$\rho_s (i_1, i_3) = \int_0^1 |\alpha+\beta||\alpha'+\beta'| \, d\varepsilon$$

$$= \int_0^1 |\alpha\alpha'| + |\beta\beta'| + |\alpha\beta' + \beta\alpha'| \, d\varepsilon$$

$$\geq \int_0^1 |\alpha\alpha'| + |\beta\beta'| \, d\varepsilon$$

$$\geq \rho_s (i_1, i_2) + \rho_s (i_2, i_3), \qquad (21)$$

where the second step follows from the way the signs have been chosen. Hence, for these three curves, close agreement as measured by *Ps* between i_1 and i_2, as well as between i_2 and i_3 nevertheless gives the result that curves i_1 and i_3 are not close to each other. This counterintuitive result shows that *Ps* is not a good measure of the agreement between intensity spectra.

One factor of Equation (10) preventing r from satisfying the triangle inequality is the denominator. The original purpose for the denominator was to emphasize the extrema in the intensity spectra (6). The function ρ, however, which does not treat the extrema in any special way, conveys almost the same information as r because the denominator is a very mild weighing function varying at most by a factor of two and on average by much less than that. Had the weighing function been chosen to be proportional to, say,

$$(10 \, |d_o| + |d_o|_{max})^{-1} \qquad (22)$$

then a function like ρ would be much less successful at bounding r. As it is, let us eliminate the denominator in order to attempt to restore the triangle inequality. Taking the square root of the resulting function, we arrive at the modified R-factor

$$r_m^2 = \tfrac{1}{2} \int_0^1 |\delta'| \, d\varepsilon. \qquad (23)$$

In terms of the intensity spectra, r_m is

$$r_m(i_1, i_2) = [\int_0^1 |i_1' - i_2'||i_1'' - i_2''| \, d\varepsilon]^{1/2}. \qquad (24)$$

If both dimensionless spectra are multiplied by a positive constant, this R-factor is multiplied by the same constant, so r_m is a symmetric, positive definite homogeneous function of order 1. The function r_m is related closely to the Euclidean norms for the first and second derivatives given by

$$r_1 = [\int_0^1 |i_1' - i_2'|^2 \, d\varepsilon]^{1/2} \tag{25}$$

and

$$r_2 = [\int_0^1 |i_1'' - i_2''|^2 \, d\varepsilon]^{1/2}. \tag{26}$$

Despite the similarity of form, however, r_m itself is not a norm and still does not satisfy the triangle inequality, as is demonstrated in the Appendix.

There are many ways of proceeding at this point. Up to now all the modifications have retained the essential character of the original definition; even the function r_m bounds R_{ZJ} within a factor of two. It appears that no function that retains the essence of R_{ZJ} can be a metric. Although a reasonable R-factor need not be a metric in the strict mathematical sense, for similar curves it is essential that the triangle inequality hold.

Before leaving R_{ZJ} completely, let us examine another aspect of this function. The R-factor may be viewed as an operator on $f = i_1 - i_2$, where f is piecewise C^2. From the definition of R_{ZJ} we see that its null space consists of continuous, piecewise linear functions. This is not a suitable null space for a LEED R-factor since intensity spectra that have peaks in very different positions, and even different numbers of peaks, can nevertheless have an R-factor of zero.

3. Analysis of Other Reliability Factors

We now look at R-factors due to Pendry (8), Van Hove et al. (7), Adams et al. (5,11,12), Sobrero and Weinberg (13) and the X-ray R-factor (9,16). These R-factors are metric

functions or, with minor modifications, can be converted into metrics. The numerical R-factor of Sobrero and Weinberg reflects the distance between the physical surface structure and the parameterized model structure for the dynamical scattering of LEED. For kinematic scattering, as in X-ray diffraction, the distance between structures can be measured by an analytic function.

The technique of analyzing an R-factor by examining its null space can be applied to the function proposed by Pendry (8). This R-factor is defined as

$$R_{PE} = \frac{<<(Y_1 - Y_2)^2>>}{<<Y_1^2> + <Y_2^2>>}, \qquad (27)$$

where the double angle brackets denote the average over all beams and all energies and

$$Y = (L^{-1} + V^2 L)^{-1}. \qquad (28)$$

In Equation (28), L is the logarithmic derivative $L = I'/I$, V is the imaginary part of the inner potential, and the prime denotes differentiation with respect to energy. This R-factor can be written more symmetrically in terms of the dimensionless variables

$$e = E/V$$

$$i(e) = I(E)/<I(E)>$$

$$l = i'/i$$

and

$$y = (l^{-1} + l)^{-1},$$

where the intensity average is only over energy and the prime denotes d/de. The formula for R_{PE} is given by Equation (27) with y_i in place of Y_i.

To find the null space of R_{PE}, assume the denominator is not zero. Then $R_{PE} = 0$ if and only if $y_1 = y_2$ for all beams at all energies. This gives a quadratic equation for l_1 in terms of l_2 with the two solutions

$$l_1 = l_2$$

and

$$I_1 = I_2^{-1} \tag{30}$$

which are ordinary differential equations for the intensities. Solving these equations shows that $R_{PE} = 0$ only if

$$i_1 = ci_2$$

or

$$i_1 = c \exp[\int (d \ln i_2/de)^{-1} de] \, . \tag{31}$$

The first solution is the intended null space of R_{PE} but the second solution could be problematic. Fortunately, we are interested only in using R_{PE} to compare intensity spectra that are similar in shape, i.e., I_1 similar to I_2 and very different from I_2^{-1}. Hence the second solution should not arise in practice.

For curves that are very similar, the reliability factor R_{PE} is almost a norm for the functions y_i. If we define the normalized y's by

$$\eta = y/\langle y^2 \rangle^{1/2} \tag{32}$$

then

$$r_{PE} = \langle\langle (\eta_1 - \eta_2)^2 \rangle\rangle^{1/2} \tag{33}$$

is the Euclidean norm for the difference $\eta_1 - \eta_2$. The functions r_{PE} and R_{PE} will have the same value if $\langle y_1^2 \rangle = \langle y_2^2 \rangle$ for all beams.

Van Hove, Tong and Elconin (7) used five R-factors to compare intensity spectra:

$$R_1 = \int |I_1 - cI_2| \, dE \, / \int |I_1| \, dE$$

$$R_2 = \int (I_1 - cI_2)^2 \, dE \, / \int (I_1)^2 \, dE$$

R_3 = fraction of energy range where curves have slopes of different signs

$$R_4 = \int |I_1' - cI_2'| \, dE \, / \int |I_1'| \, dE$$

$$R_5 = \int (I_1' - cI_2')^2 \, dE \, / \int (I_1')^2 \, dE$$

with the scaling factor

$$c = \int I_1 dE \,/\!/ \int I_2 dE. \tag{34}$$

The normalizations lead to difficulties since only R_3 is a metric; it is the energy average of the discrete metric (13) applied to the function sign(I') and can be written as

$$R_3 = \tfrac{1}{2} \langle |\mathrm{sign}(I_1') - \mathrm{sign}(I_2')| \rangle \,. \tag{35}$$

With slight changes in the scaling factors and normalizations, the other four R-factors can be converted into norms. The normalization should not depend solely on one of the curves since either spectrum is only an approximation to the unknown true curve. The need for normalization can be eliminated by using the dimensionless variables ε and i introduced in Equations (5-6) and by defining the dimensionless spectrum

$$j = i / \| i \|, \tag{36}$$

where

$$\| i \| = [\int_0^1 i^2 \, d\varepsilon]^{1/2}. \tag{37}$$

Replacing the scaling factors in the definitions of R_2 and R_5 with

$$c_2 = \| i_1 \| / \| i_2 \| \tag{38}$$

and taking their square roots gives

$$r_1 = \langle | i_1 - i_2 | \rangle$$

$$r_2 = \| j_1 - j_2 \|$$

$$r_3 = \tfrac{1}{2} \langle |\mathrm{sign}(i_1') - \mathrm{sign}(i_2')| \rangle$$

$$r_4 = \langle | i_1' - i_2' | \rangle$$

and

$$r_5 = \| j_1' - j_2' \|, \tag{39}$$

where r_1 and r_2 are norms for the difference between spectra, r_4 and r_5 are norms for the first derivatives, and r_3 is a metric for i'. The l_p norms are defined by

$$l_p(x) = \langle |x|^p \rangle^{1/p} \text{ for } p \geq 1 \tag{40}$$

so r_1 and r_4 are l_1 norms, while r_2 and r_5 are l_2 (or Euclidean) norms. The sum $r_1 + r_4$ is the Sobolev norm for differentiable functions. With a slightly different normalization, the five R-factors can be expressed in terms of the spectra i by using

$$r_{2'} = \|i_1 - i_2\|$$

and

$$r_{5'} = \|i_1' - i_2'\|. \qquad (41)$$

With five metric functions in hand, it is useful to see how much information is conveyed by each one. Eventually, the R-factor must determine which set of parameter values is the best and what other values are so close that the difference is not significant. Hence, the objective of the LEED structure analysis is to decide if one set of five R-values is better than another set. The five R-factors will, other than in exceptional cases, give different optima for the parameters, they do not all convey the same amount of useful information, and they are not statistically independent.

The discrete metric r_3 does not convey much information useful for LEED intensity analysis. It was originally stated (7) that for parameter values near the true surface structure all five R-factors should have local minima. Suppose r_4 and r_5 are small (so the derivatives match fairly closely), while r_3 is large. That r_3 is not also small indicates that there are ranges where i_1' and i_2' are both near zero, but they happen to have opposite signs. It is not desirable to assign large R-values to small differences in slopes, so r_3 confuses the evaluation of the level of agreement between curves. Also, we would not assign any significance to the finding that r_3 was small, while the other R-factors were not. If two sets of parameters give the same small values for r_1, r_2, r_4 and r_5 but gave very different values for r_3, we would not feel confident in declaring one set of parameters better than the other. Thus, r_3 is not very useful in finding the best parameter values.

Of the other four R-factors, r_1 and r_2 are statistically correlated, as are r_4 and r_5. This can be demonstrated using $r_{2'}$ and $r_{5'}$. The R-factor r_1 measures the first moment of the curve $\Delta = i_1 - i_2$ while $r_{2'}$ measures the second moment. The quantity

$$\sigma_2 = (r_{2'}^2 - r_1^2)^{1/2} \tag{42}$$

is a measure of the variance of Δ. Hence, $r_{2'}$ and σ_2 are two independent measures of the agreement between curves. If two sets of parameters give similar values for $r_{2'}$, then the set with the smaller σ_2 provides a better fit to the data. Similarly, we can construct

$$\sigma_5 = (r_{5'}^2 - r_4^2)^{1/2}. \tag{43}$$

If the variance between curves remains approximately constant for different parameter values (e.g., if the variance is dominated by experimental uncertainties), then r_1 and $r_{2'}$ will be highly correlated, and likewise for r_4 and $r_{5'}$.

Sobrero and Weinberg (13) presented a numerical reliability factor that reflects the level of agreement between a structural model and the true surface structure. In LEED, the dynamical theory is sufficiently complicated that no closed-form, analytical function with this property is known. For X-ray diffraction, however, the theory is simple and an R-factor to measure the agreement between structures can be derived. This derivation is based on Parseval's theorem (15).

In the kinematic theory of X-ray diffraction (16), the electron density in a crystal, $\rho(x)$, can be expressed in a Fourier series as

$$\rho(x) = \Sigma F_{\mathbf{h}} e^{-i\mathbf{h}\cdot\mathbf{x}} / V, \tag{44}$$

where V is the volume of the unit cell, $F_{\mathbf{h}}$ is a structure factor, and $\mathbf{h}$ is a reciprocal lattice vector. The Euclidean norm of ρ is

$$\| \rho \|^2 = \Sigma |F_{\mathbf{h}}|^2 / V^2. \tag{45}$$

For two different structures, e.g., the true structure and an approximate model, we have

$$\rho_1 - \rho_2 = \Sigma(F_1 - F_2)e^{-i\mathbf{h}.\mathbf{x}} / V, \tag{46}$$

and

$$||\rho_1 - \rho_2||^2 = \Sigma|F_1 - F_2|^2 / V^2. \tag{47}$$

The structure factors are complex numbers,

$$F = |F| e^{i\phi} \tag{48}$$

but experimentally, only the modulus |F| can be measured; the phases are reconstructed from the moduli. This procedure gives F_1 and F_2 the same phase for each **h**, so

$$F_1 - F_2 = (|F_1| - |F_2|) e^{i\phi} \tag{49}$$

and

$$||\rho_1 - \rho_2||^2 = \Sigma||F_1| - |F_2||^2 / V^2. \tag{50}$$

This expression provides an un-normalized R-factor for X-ray diffraction.

The usual normalization is to divide by the sum of the observed moduli, $\Sigma|F_1|/V$.

Adopting this procedure, one obtains

$$R_{XRD} = (\Sigma||F_1| - |F_2||^2)^{1/2} / \Sigma|F_1|, \tag{51}$$

which can be compared with the usual X-ray R-factor (17),

$$R_{XRD'} = \Sigma||F_1| - |F_2||) / \Sigma|F_1|. \tag{52}$$

As noted above, there are problems with normalization based on only one of the two data sets. These issues can be avoided by introducing the dimensionless

$$f_{\mathbf{h}} = F_{\mathbf{h}} / ||F||, \tag{53}$$

where the norm is

$$||F||^2 = \Sigma|F_{\mathbf{h}}|^2. \tag{54}$$

This gives, finally,

$$r_{XRD} = (\sum ||f_{1h}| - |f_{2h}||^2)^{1/2} \qquad (55)$$

as a normalized R-factor for structure determination by X-ray diffraction; r_{XRD} is related closely to the function minimized in the least-squares refinement of structures (17). If the kinematic model is correct, r_{XRD} directly measures the Euclidean norm of the difference between two structures.

It is unfortunate that we cannot derive a closed-form R-factor for LEED in a similar manner. If we assume, however, that the dynamical theory provides an adequate model for LEED intensities, then we can formulate a numerical R-factor to measure the distance between two structures. In the X-ray case, a Fourier transformation provided the connection between the structural model and the diffracted amplitudes, from which the intensities are then obtained. For LEED, the connection is a complex dynamical scattering model expressed as

$$q = I(p), \qquad (56)$$

where q are the intensities and p are the parameters. As with r_{XRD}, it is necessary to assume that the recorded intensities q* lie in Q, the range of I. If we also assume that near the optimum p* the function I(p) is continuous and bijective, then a continuous I^{-1} exists and can be estimated numerically. This leads to the definition

$$r_{SW} = d[I^{-1}(q^*), p], \qquad (57)$$

where d is a metric in the parameter space. The main difficulty with applying this function is that it is necessary to project the measured intensities onto Q.

Finally, we turn to the method used by Adams et al. (5,11,12) to obtain uncertainty intervals for the optimum parameter values. The R-factor R_2 defined in Equation (34) is used to measure the error between intensity spectra. The standard deviations of the parameters are computed from the curvature matrix at the optimum parameter values,

p*. There is a difficulty with this choice since it fails to take into account uncertainties in the data and so the method of Ref. (12) can make the computed uncertainties appear arbitrarily small, a spurious result.

Couching the analysis in terms of the norm r_2 and its square r_2^2, a Taylor series expansion around a point in parameter space, p_0, gives

$$r(p) = r_0 + \mathbf{g}_0^T\delta + \tfrac{1}{2}\delta^T\mathbf{G}_0\delta + 0(\|\delta\|^3), \tag{58}$$

where $\delta = p - p_0$, $\mathbf{g}$ is the gradient vector, $\mathbf{G}$ is the Hessian matrix, and we have dropped the subscript on r_2. At a strong local minimum in r the gradient is zero and for a scalar parameter we have

$$r(p) = r_0 + 1/2\, G_0\delta^2 + 1/6\, \gamma_0\delta^3 + 0(\delta^4), \tag{59}$$

which gives

$$r^2(p) = r_0^2 + r_0G_0\delta^2 + 1/3\, r_0\delta^3 + 0(\delta^4), \tag{60}$$

where γ_0 is the third order coefficient. The ratio of the second to the third term is the same for both expansions, so the ranges over which r and r^2 can be approximated by quadratics are identical if the next term to enter the expansions is the cubic term. Both r and r^2 have strong minima at p_0, but the curvatures differ. The function r^2 is more sharply curved and therefore appears to define the optimum p_0 more precisely than r, but the gain is illusory. Following Ref. (12), we would estimate the uncertainties as

$$\sigma_1^2 = G_0^{-1}r_0/(N - \nu)$$

and

$$\sigma_2^2 = G_0^{-1}r_0/2(N - \nu) \tag{61}$$

for r and r^2, respectively. Here, N is the number of degrees of freedom and ν is the number of fitted parameters. It appears that by squaring the R-factor we have gained a factor of 2 in improved precision. Of course, the argument employed in going from Equation (59) to Equation (60) can be repeated to produce the functions r^4, r^8,... , gaining an apparent reduction of 2 in the uncertainties with each step.

Since there is no change in the information content, the improved precision is illusory and the estimates in Equation (61) are erroneous. The correct result is provided by the observation that if

$$|r_0 - r_1| \leq \varepsilon \tag{62}$$

for a parameter p_1, then

$$\begin{aligned} |r_0^2 - r_1^2| &= |r_0 - r_1||r_0 + r_1| \\ &\leq 2r_0\varepsilon \end{aligned} \tag{63}$$

to order ε^2. If ε is an estimate for the magnitude of the errors in the experimental and calculated intensities when r is used as the R-factor, then $2r_0\varepsilon$ measures the variance in the intensities when r^2 is used. Since r_0 and r_1 are equal within the uncertainties in the data analysis, we include all the values p_1 that satisfy Equation (62) in the interval of acceptable parameters (18). This leads to

$$\|p_1 - p_0\|^2 = 2\varepsilon / e^T G_0 e(N - \nu), \tag{64}$$

where the error vector $e = (p_1 - p_0)/\|p_1 - p_0\|$. If G_0 is ill-conditioned, then the uncertainty in the parameters depends on the direction of e. The largest uncertainty occurs in the direction of the eigenvector corresponding to the eigenvalue of G with the smallest magnitude (18). So the difficulty with the uncertainty estimates of Adams et al. is with the use of r_0 as a measure of the variance in the data.

We have demonstrated that several of the R-factors proposed for LEED can be modified to make them metric functions. With the present limited understanding of the statistical distribution of errors in LEED it is not possible to determine which is the best R-factor. This leads to the situation where some R-factors, such as r_{PE}, are formulated with the intent that they will account for some of the known deficiencies in LEED theory, e.g., the large discrepancies in absolute intensities. As both the theory and the experiment improve, the need for the R-factor to play this role should diminish.

We have emphasized the interpretation of the R-factor as a metric over an appropriate space. For example, r_{PE} is a metric for the functions y(e) defined in Equation (29) while r_4 is a metric for the first derivatives i'. Since both the experimentally observed data and the computed intensity spectra contain errors, they can be considered estimates for the true intensities. It is essential, therefore, that the R-factor satisfy the triangle inequality when similar spectra are compared. This guarantees that the unknown distance between the true intensity and the computed solution is bounded by the measured distance between the observed and the fitted curves plus the estimated variance of the data.

A question remains as to the proper averaging of the R-factor. The common practice in LEED is to average point values as a function of the energy variable to obtain single beam R-factors. (R_{PE} is a slight exception; a small modification in the definition [e.g. the function r_{PE} given by Equation (33)] puts it into this form.) Uniform energy averaging, however, reduces the sensitivity of LEED structure determination and increases the variance of the parameters. The structural information contained in an intensity spectrum is distributed approximately uniformly in momentum space (k-space). One manifestation of this is that features such as peaks in the spectra broaden with increasing energy. Energy averaging, therefore, amounts to a weighted average in k-space where the high momentum transfer information is emphasized at the expense of the low k transfer data. Since the high energy electrons are penetrating more deeply into the sample, surface sensitivity is reduced. (In X-ray crystallography, the R-factor is an average in k-space.) Strictly speaking, the conversion to a momentum scale requires that the inner potential, Vo, be known. But, only an approximate estimate is needed to produce a practical scale. Sensitivity can be increased and the variance reduced by employing a statistically weighted average in k-space.

In conclusion, we have discussed a number of reliability factors for LEED from a unified point of view and shown that the Zanazzi-Jona R-factor is not a suitable measure of the

level of agreement between intensity spectra. Without a firm theoretical foundation, any of a number of metric functions can be used as a reliability factor, but as both the experiment and the theory improve, the need for the R-factor to be insensitive to certain types of discrepancies should decrease. Finally, we have shown that no matter which metric is used as an R-factor, Equation (64) should be used to obtain an estimate of the variance in the parameters and that the average is best computed over momentum space.

References

1. D. L. Adams, H. B. Nielsen and J. N. Andersen, Surface Sci. **128**, 294 (1983).

2. D. L. Adams, H. B. Nielsen, J. N. Andersen, I. Stensgaard, R. Feidenhans'l and J. E. Sorensen, Phys. Rev. Letters **49**, 669 (1982).

3. H. L. Davis and J. R. Noonan, J. Vacuum Sci. Technol. **20**, 842 (1982).

4. H. L. Davis and J. R. Noonan, Surface Sci. **126**, 245 (1983).

5. H. B. Nielsen, J. N. Andersen, L. Petersen and D. L Adams, J. Phys. C **15,** L1113 (1982).

6. E. Zanazzi and F. Jona, Surface Sci. **62**, 61 (1977).

7. M. A. Van Hove, S. Y. Tong and M. H. Elconin, Surface Sci. **64**, 85 (1977).

8. J. B. Pendry, J. Phys. C **13**, 937 (1980).

9. C. B. Duke, A. Paton, W. K. Ford, A. Kahn and J. Carelli, Phys. Rev. B **24**, 562 (1981).

10. J. Philip and J. Rundgren, in *Determination of Surface Structure by LEED*, P. M. Marcus and F. Jona (eds.), Plenum, New York (1985).

11. D. L. Adams, H. B. Nielsen and M. A. Van Hove, Phys. Rev. B **20**. 4789 (1979).

12. H. B. Nielsen and D. L. Adams, J. Phys. C **15**, 615 (1982).

13. A. C. Sobrero and W. H. Weinberg, in *Determination of Surface Structure by LEED*, P. M. Marcus and F. Jona (eds.), Plenum, New York (1985).

14. N. R. Draper and J. Smith, *Applied Regression Analysis,* Wiley, New York (1966).

15. G. Dahlquist and A. Björck, *Numerical Methods*, Prentice-Hall, Englewood Cliffs, New Jersey (1974).

16. M. M. Woolfson, *X-Ray Crystallography*, Cambridge University Press, Cambridge (1970).

17. G. H. Stout and L. H. Jensen, *X-Ray Structure Determination*, Macmillan, New York (1968).

18. P. E. Gill, W. Murray and M. H. Wright, *Practical Optimization,* Academic, New York (1981).

APPENDIX

It remains to be shown that the function r_m defined in Equation (23) does not satisfy the triangle inequality. Let $r_{jk} = r_m(i_j,i_k)$ and recall that

$$r_{12}^2 = \int_0^1 |\alpha\alpha'| \, d\varepsilon \tag{A1}$$

and similarly for r_{23} and r_{13} using β and γ [defined in Equation (20)]. We will construct a counterexample to the triangle inequality. Suppose that

$$r_{13} > r_{12} + r_{23} \geq 0. \tag{A2}$$

Then, in terms of α and β,

$$\int_0^1 |\alpha+\beta||\alpha'+\beta'| - |\alpha\alpha'| - |\beta\beta'| \, d\varepsilon > 2r_{12}r_{23}. \tag{A3}$$

As before, we will choose α and β to have the same sign, and also α' and β' so that the integrand simplifies. We obtain

$$(\int_0^1 |\alpha\beta'+\beta\alpha'| \, d\varepsilon)^2 > 4 \int_0^1 |\alpha\alpha'| \, d\varepsilon \int_0^1 |\beta\beta'| \, d\varepsilon \tag{A4}$$

as a sufficient condition on α and β, subject to the sign restriction. A particularly simple example is to take three curves with

$$\alpha \geq 0$$

and

$$\beta = \alpha + c, \; c>0, \tag{A5}$$

where c is a constant. We will establish that Equation (A4) holds.

Let

$$a = \int_0^1 |\alpha'|\, d\varepsilon \qquad \text{(A6)}$$

and

$$A = \int_0^1 |\alpha\alpha'|\, d\varepsilon. \qquad \text{(A7)}$$

Assuming α' is not zero everywhere, we have

$$c^2a^2 > 0$$

$$(2A + ca)^2 > 4A(A + ca)$$

$$[\int_0^1 |(2\alpha + c)\alpha'|\, d\varepsilon)]^2 > 4 \int_0^1 |\alpha\alpha'|\, d\varepsilon\, [\int_0^1 |(\alpha + c)\alpha'|\, d\varepsilon)]$$

$$(\int_0^1 |\alpha\beta' + \beta\alpha'|\, d\varepsilon)^2 > 4 \int_0^1 |\alpha\alpha'|\, d\varepsilon \int_0^1 |\beta\beta'|\, d\varepsilon,$$

which establishes Equation (A4), and hence demonstrates that the triangle inequality is violated for this choice of curves.

Chapter V

A Mathematical Foundation for *Ad Hoc* Reliability Factors in LEED

Reprinted with permission from A. C. Sobrero and W. H. Weinberg, "A Mathematical Foundation for *Ad Hoc* Reliability Factors in LEED," in P. M. Marcus and F. Jona, eds., *Determination of Surface Structure by LEED*, Plenum, New York (1985).

From: DETERMINATION OF SURFACE STRUCTURE BY LEED
Edited by P.M. Marcus and F. Jona
(Plenum Publishing Corporation, 1985)

A MATHEMATICAL FOUNDATION FOR AD HOC RELIABILITY FACTORS IN LEED*

A. C. Sobrero and W. H. Weinberg‡

Division of Chemistry and Chemical Engineering
California Institute of Technology
Pasadena, CA 91125

1. INTRODUCTION

In surface crystallography by low-energy electron diffraction (LEED), the reliability factor provides a measure of the agreement between the experimental data and the calculated intensity spectra. Ideally, statistical considerations completely determine the reliability factor (r-factor). For LEED however, the r-factor will remain somewhat arbitrary until discrepancies between theory and experiment, such as the differences in absolute intensities, are better understood. Nevertheless, statistics and functional analysis can guide the formulation of r-factors to maximize the amount of information obtained from the data.

Clearly, the use of arbitrary reliability factors can add to the inaccuracy and uncertainty of the structural determination. Zanazzi and Jona[1] illustrate this point in their review of reliability criteria. Van Hove *et al.*[2] demonstrate that only when the correspondence between computed and observed values is excellent will different r-factors yield similar estimates for the parameters. This further indicates that inappropriate r-factors can degrade LEED results. Despite these caveats, employing a reliability factor will almost always be superior to simple visual evaluation.[1]

As a quantitative technique for surface crystallography, LEED must provide statistically meaningful confidence limits on the structural parameters. This is discussed in section 3. The use of the r-factor in a gradient search for the correct structure is presented in the section on metrics.

* Supported by the Army Research Office under grant No. DAAG29-79-C-0132.

‡ Camille and Henry Dreyfus Foundation Teacher-Scholar.

2. TRADITIONAL LEED INTENSITY ANALYSIS

The usual method for analysing multiple-scattering LEED data is a trial-and-error procedure.[1] This review of the method serves to introduce the definitions of the parameter manifold P, the intensity space Q, and the intensity operator I. The reconstructed Ir(110)-(1x2) surface[3] is discussed to illustrate the notation.

The first step in the data analysis is to postulate a family of models, $M(\vec{p})$, for the structure. Here the point $\vec{p}$ is a member of the parameter space P which characterizes the family. In this way, each point in P represents a model of the surface according to the mapping

$$\vec{m} = M(\vec{p}). \tag{1}$$

The models $\vec{m}$ include the atomic positions, phase shifts, inner potentials, and other factors which govern low-energy electron scatter.

Often, several different families M_i are proposed, each with its own parameter space P_i. Consider the two models for Ir(110) illustrated in Figure 1. The paired rows model M_1 has a three dimensional parameter space P_1, where σ, δ_1, and E_0 can vary (see the caption to Figure 1 for definitions). The components of a point in the space P_1 are: $\vec{p} = (\sigma, \delta_1, E_0)$. Similarly, the parameter space for the missing row model M_2 is four dimensional, with $\vec{p} = (\delta_1, \delta_2, \beta, E_0)$ when $\vec{p} \in P_2$.

Clearly, not all the points in a parameter space P_i are acceptable. There are two restrictions: the $\vec{p}$ must map to physically realizable structures, and each structure should correspond to a unique point. The second condition insures that the mapping M_i is one-to-one, thus avoiding ambiguities in the parameterization of the crystal surface. For example, the spacing σ must always be less than or equal to a.

These constraints limit the choice of parameter values to a manifold $P_i \subseteq P_i$. The bounds actually used with the paired rows model M_1 were: $\sigma \in [2.95\ \text{Å}, 3.55\ \text{Å}]$, $\delta_1 \in [1.21\ \text{Å}, 1.81\ \text{Å}]$, and $E_0 \in [-10\ \text{eV}, -20\ \text{eV}]$. This manifold lies well within the above constraints.

The next step in the procedure is to calculate the intensity spectrum $\vec{q}$ for each model:

$$\vec{q} = \hat{I}(M_i(\vec{p})). \tag{2}$$

The operator $\hat{I}$ denotes the computational method used to obtain the spectrum. This nonlinear operator constitutes a mathematical model for electron diffraction.[4] The spectrum $\vec{q}$ is a point in the high-dimensional intensity space Q, with each component q_j representing the intensity of one beam at a particular electron energy and angle of incidence. Thus, all the data from a LEED experiment defines one point, $\vec{q}^{\,*}$, in Q.

In the case of Ir(110), because I-V curves were computed for 18 beams at 2 eV intervals over an average range of 100 eV and for one angle of

incidence, the intensity space Q is 900-dimensional. Here, for example, the first 50 dimensions might represent the intensity of the (01) beam at 30 eV, 32 eV,..., 128 eV.‡ The operator $\hat{I}$ consisted of the Reverse Scattering Perturbation with Layer Doubling.[5]

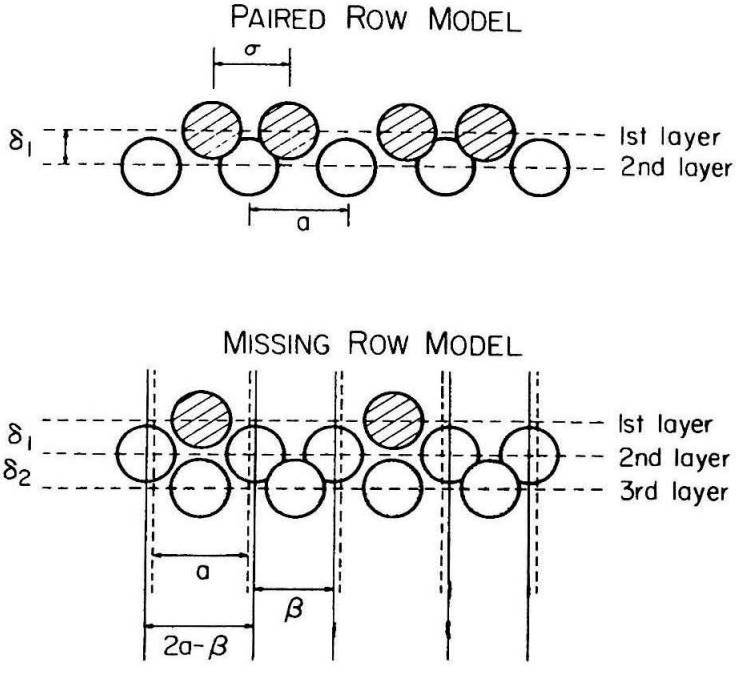

Figure 1. Two models for the reconstructed Ir(110)-(1x2) structure. Here, a = 3.58 Å is the bulk spacing between rows of atoms in the (001) direction, while δ_1 is the distance from the first to the second layers of atoms. The real part of the inner potential, E_0, is a non-structural parameter in the models. Other geometrical parameters: for the paired rows model, σ is the spacing between the adjacent close-packed top rows of atoms which have moved toward each other; in the missing row model, δ_2 is the distance from

‡ Since the experimental intensities were not recorded at exactly these values of the energy, it was necessary to interpolate the data. This projection is a mapping from the data space to Q.

the second to the third layer, while β is the spacing between the adjacent rows of atoms in the second layer.

Henceforth, to simplify the notation, consider only one family of models M, and define the intensity operator I as the composition $\hat{I} \circ M$. The operator I now provides a direct connection between the parameter manifold P and the intensity space Q:

$$\vec{q}_i = I(\vec{p}_i) \qquad \text{for } \vec{p}_i \in P. \tag{3}$$

Since I describes a physical process, assume that this operator is a continuously differentiable function of $\vec{p}$. Figure 2 illustrates the relationship between the various mappings.

The final stage in the structural analysis is to minimize the reliability factor,

$$r_i = D(\vec{q}^{\,*}, \vec{q}_i), \tag{4}$$

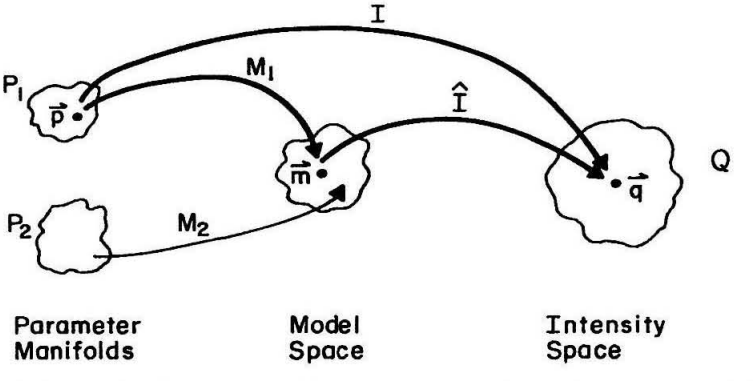

Figure 2. Schematic indicating the range and domain spaces for the operators introduced in the text.

over the set $\{\vec{q}_i\}$ of computed points and thus obtain the calculated spectrum which best matches the observed one. The function $D(\vec{q}_1, \vec{q}_2)$ measures a distance, in some sense, between members of the space Q. For convenience, denote the best fitting spectrum by $\vec{q}^+$ and the corresponding surface structure by $\vec{p}^+$, so that $\vec{q}^+ = I(\vec{p}^+)$. Also, define the vector of residuals as

$$\vec{\varepsilon} = \vec{q}^* - \vec{q}^+. \tag{5}$$

This vector contains the variation in the data which is not explained by the mathematical model $I(\vec{p})$.

3. STATISTICS

Due to random errors in the experiment, the deterministic model $I(\vec{p})$ cannot fit the observed data perfectly. It is important, therefore, to measure how well the model accounts for the observations by checking the residuals ε_i. Unfortunately, the standard techniques are not appropriate for LEED.

The ususal approach in statistics is to assume a stochastic model for the residuals and then derive the reliability factor by maximizing the *likelihood function*.[6] A widely used model, which leads to the method of weighted least squares, is that the ε_i are Gaussian. Specifically, the assumption is that the residuals are *n*ormally and *i*ndependently *d*istributed random variables with variances s_i^2 and zero mean [abbreviated $NID(0, s_i^2)$].[7] The r-factor derived from this stochastic model is the weighted Euclidean or L_2 norm[8]

$$D(\vec{q}_1, \vec{q}_2) \equiv \left[\sum_j [(q_{1j} - q_{2j})/s_j]^2 \right]^{1/2} = \left[\sum_j (\varepsilon_j/s_j)^2 \right]^{1/2}. \tag{6}$$

Here q_{ij} is the j^{th} component of $\vec{q}_i$. (The function R2 proposed by Adams[2] for I-V curves is related to the square of L_2.) After this r-factor is minimized, the Snedecor F or, Student t, distribution provides confidence limits for the parameter values.[9] Clearly, changing the assumed values for the variances s_i^2 will affect the parameter estimates. The data, however, will support only a small range of s_i^2. When the residuals do not substantiate the assumed stochastic model, the F statistic indicates that the parameter values are meaningless. Thus, the fitting procedure can be tested for self consistency, and there is a statistical basis for establishing confidence limits.

For LEED, the positions of peaks in the computed I-V curves are less sensitive than the peak amplitudes to deficiencies of the model $I(\vec{p})$. This implies that the residuals are not $NID(0, s_i^2)$ so that the standard statistics are inapplicable. At present, there is no successful model for the ε_i in LEED.

This is the crux of the problem of finding the best reliability factor. Without a model for the errors, there is no test for internal consistency. In effect, this greatly increases the uncertainty of the parameter estimates.

4. THE RELIABILITY FACTOR AS A METRIC

Although statistical considerations will not determine the reliability factor for LEED, other requirements can limit the choice of functional form. For example, the r-factor must be a metric function. To understand this, consider the definition of a metric presented in the appendix. Suppose $\vec{q}_1$ is a computed spectrum and $\vec{q}_2$ the corresponding experimental one. The information contained in these two spectra is unchanged if it is discovered that they have been mislabelled and that $\vec{q}_1$ is really the experimental data. Since altering the labels does not modify the level of agreement between the spectra, the r-factor must be symmetric, with $D(\vec{q}_1, \vec{q}_2) = D(\vec{q}_2, \vec{q}_1)$. Having $D(\vec{q}_1, \vec{q}_2) = 0$ if and only if $\vec{q}_1 = \vec{q}_2$ corresponds to the notion that the r-factor measures the discrepancy between spectra and that a zero value signals perfect agreement.

The triangle inequality says that if two spectra agree well with a third, then they also agree with each other. Consider the implications of violating this axiom. Suppose someone measures $\vec{q}_1^{\,*}$ and computes $\vec{q}_1^{\,+}$, obtaining a small r-factor $D(\vec{q}_1^{\,*}, \vec{q}_1^{\,+})$. Another worker independently measures $\vec{q}_2^{\,*}$ for the same crystal surface and verifies that $D(\vec{q}_1^{\,*}, \vec{q}_2^{\,*})$ is small. Then, it would be ridiculous to find that $D(\vec{q}_1^{\,+}, \vec{q}_2^{\,*})$ was large. Hence, a function which does not satisfy the triangle inequality cannot be a very useful reliability factor.

Of course, many metric functions, such as D_1 in the appendix, are not suitable reliability factors. To be a good r-factor, the function D must be continuously differentiable so that minor variations in the spectra produce only small changes in the value of D. Also, since some of the components of $\vec{p}$ are more important than others, the sensitivity of the r-factor to the parameters should be variable. Finally, the expense of an exhaustive enumeration search through the manifold P dictates that gradient, or steepest descent, techniques be used where feasible.[10] For this reason, the negative of the gradient of $D(I(\vec{p}), \vec{q}^{\,*})$ with respect to $\vec{p}$ should point toward $\vec{p}^{\,+}$ over a large region in parameter space. It will be shown, by construction for a special case, that functions which have these properties do exist.

In order to simplify the discussion, define the functions I^{-1} and D^* as follows. The inverse of I is any operator I^{-1} with $I(I^{-1}(\vec{q})) = \vec{q}$ in some open set of intensity space. Because I is a very nonlinear function, its inverse does not necessarily exist over all of Q. Nevertheless, $I(\vec{p})$ is one-to-one at $\vec{p}^{\,+}$. Otherwise there is a degeneracy where many different surface structures produce the same intensity spectrum, $\vec{q}^{\,+}$, and the structural analysis by LEED would not be possible. This guarantees the existence of I^{-1} for a region Z in the space Q near $\vec{q}^{\,+}$. The range of I^{-1} is the region z near $\vec{p}^{\,+}$ where I is invertible. If necessary, the inverse mapping can be approximated using standard numerical methods.

The function D^* is a convenient shorthand,

$$D^*(\vec{p}) = D(I(\vec{p}), \vec{q}^{\,*}), \tag{7}$$

where the gradient of D^* with respect to $\vec{p}$ is simply ∇D^*. Thus, the ideal

reliability factor has $-\nabla D^*(\vec{p})$ pointing toward $\vec{p}^+$, with the magnitude of $D^*(\vec{p})$ indicating the distance to the optimal parameters.

In general, since $D^*(\vec{p}^+)$ is not zero, no reliability factor can measure exactly the distance from $\vec{p}$ to $\vec{p}^+$. With "artificial data," however, such a measure is possible. In this case, there is a set of parameters $\vec{p}^*$ with $\vec{q}^* = I(\vec{p}^*)$ so that the inverse I^{-1} exists at $\vec{q}^*$. Then, the formulation of a function which possesses the desiderata mentioned above proceeds in two stages. First one constructs a norm $d(\vec{p}_1, \vec{p}_2)$ over the space P. This function then defines the reliability factor $D(\vec{q}_1, \vec{q}_2)$ over Q. The inverse of the intensity operator I provides a connection between P and Q.

The desired sensitivities to the parameters are easily attained. The suggested procedure is to define separate norms for appropriate groups of parameters. Then, d is a linear combination of these metrics, with the weight coefficients determining the relative sensitivities. There is considerable flexibility in the choice of d, as long as the resulting function is a norm.

To illustrate the process, recall the paired rows model, where $\vec{p} = (\sigma, \delta_1, E_0)$. It is clear from Figure 2 that in terms of atomic positions, an error in σ of 0.2 Å is equivalent to a 0.1 Å error in δ_1. Thus, it is convenient to combine these two parameters in one norm. The function

$$d_1(\sigma, \sigma^*; \delta_1, \delta_1^*) = \frac{1}{\delta_0}\left[\left(\frac{\sigma-\sigma^*}{2}\right)^2 + (\delta_1-\delta_1^*)^2\right]^{1/2} \tag{8}$$

provides a good measure of the total positional error. The normalization factor δ_0 makes the metric dimensionless. If δ_0 is the bulk interlayer spacing of 1.36 Å, then the function d_1 expresses the total error as a fraction of the bulk spacing. For the real part of the inner potential, E_0, the error can be described by

$$d_2(E_0, E_0^*) = \frac{|E_0 - E_0^*|}{|E_1|} \quad . \tag{9}$$

Here, E_1 might be -15 eV, the initial value of E_0 used in the multiple scattering calculation. Combining these functions,

$$d(\vec{p}, \vec{p}^*) = a_1 d_1 + a_2 d_2 \tag{10}$$

with, say, $a_1 = 0.9$ and $a_2 = 0.1$ to reflect the relative importance of the structural parameters. Of course, other choices for these coefficients are possible. It may be advantageous, for example, to scale d to measure positional error directly in Å. Picking $a_1 = \delta_1 \times 1\ \text{Å}^{-1}$ means that $d = 0.1$ corresponds to an uncertainty of ± 0.1 Å in δ_1 or in $\sigma/2$. The function d determines what information is obtained from the experiment.

Using the inverse operator I^{-1} and the carefully constructed function d, a complete definition of the reliability factor is

$$D(\vec{q}_1, \vec{q}_2) = d(I^{-1}(\vec{q}_1), I^{-1}(\vec{q}_2)) \qquad \text{for } \vec{q}_1, \vec{q}_2 \in Z. \tag{11}$$

Clearly, the function $D(\vec{q}_1, \vec{q}_2)$ is a metric for the space Q. Furthermore, the negative of the gradient with respect to $\vec{p}$ of $D(I(\vec{p}), \vec{q}^*)$ points toward $\vec{p}^*$, with the magnitude of D indicating the distance to the optimal parameters.

The requirement that the spectra lie in the region Z is not a restriction particular to this method. Outside this region there is no one-to-one correspondence between parameter values $\vec{p}$ and intensity spectra $\vec{q}$. Hence, only within Z can any reliability factor be a measure of the error in the parameters.

5. CONCLUSION

The expense of obtaining a good approximation for I^{-1} and the unrealistic assumption about the existence of $\vec{p}^*$ make it unlikely that the function D defined in Equation (11) will be a practical reliability factor. Yet, the procedure presented above can be reversed to provide a means of evaluating *ad hoc* r-factors. For example, any proposed reliability factor can be tried on synthetic data to test whether lines of constant d map to contours of D. If these contours differ greatly, especially near $\vec{q}^*$, then the r-factor is distorting the information in the spectra. Of course, all reliability factors should ultimately be judged on the basis of the self consistency criterion discussed in section 3.

It has been shown that the reliability factor presents a two-fold challenge. A statistical basis needs to be developed so that the true precision of the parameters can be gauged. Pending this, the reliability factors which are utilized should adhere to the criteria formulated in the last section. Otherwise, some of the information painstakingly gathered by the experimentalists may be destroyed in the analysis.

APPENDIX

A function D which maps two elements from a space Q to a real number, $D: Q \times Q \to R$, is a metric or distance function if it satisfies the following four axioms:[11]

1. $D(\vec{q}_1, \vec{q}_2) = D(\vec{q}_2, \vec{q}_1)$ for all $\vec{q}_1, \vec{q}_2 \in Q$.
2. $D(\vec{q}_1, \vec{q}_2) = 0$ if and only if $\vec{q}_1 = \vec{q}_2$.
3. $D(\vec{q}_1, \vec{q}_2) > 0$ if and only if $\vec{q}_1 \neq \vec{q}_2$.
4. $D(\vec{q}_1, \vec{q}_2) = D(\vec{q}_1, \vec{q}_3) + D(\vec{q}_2, \vec{q}_3)$.

The first condition says that the distance from $\vec{q}_1$ to $\vec{q}_2$ is the same as from $\vec{q}_2$ to $\vec{q}_1$. The next two axioms say that D is positive definite, while the last condition is the triangle inequality.

A function is a norm if, in addition to being a metric, it is also linear:

5. $D(a\vec{q}_1, a\vec{q}_2) = aD(\vec{q}_1, \vec{q}_2)$ for $a \in R$. (12)

Some simple metrics are:

$D_1(\vec{q}_1, \vec{q}_1) = 0$ for all $\vec{q}_1 \in Q$.

$D_1(\vec{q}_1, \vec{q}_2) = 1$ for $\vec{q}_1 \neq \vec{q}_2$.

This is the discrete metric on Q.

$$D_2(\vec{q}_1, \vec{q}_2) = \left[\sum_j |q_{1j} - q_{2j}|^p \right]^{1/p} \quad \text{for } p \geq 1.$$

This is the L_p metric, which for $p = 2$ is the Euclidean norm.

$$D_3(\vec{q}_1, \vec{q}_2) = \sum_{m=0}^{n} |\vec{q}_1^{(m)} - \vec{q}_2^{(m)}|$$

D_3 is the Sobolev norm for functions which are m times differentiable.

REFERENCES

1. E. Zanazzi and F. Jona, A Reliability Factor for Surface Structure Determinations by Low-Energy Electron Diffraction, *Surface Sci.* 62: 61-80 (1977).
2. M. A. Van Hove, S. Y. Tong, and M. H. Elconin, Surface Structure Refinements of 2H-MoS_2, 2H-$NbSe_2$ and W(100) p(2x1)-O Via New Reliability Factors for Surface Crystallography, *Surface Sci.* 64: 85-95 (1977).
3. C. M. Chan, M. A. Van Hove, W. H. Weinberg, and E. D. Williams, An *R*-Factor Analysis of Several Models of the Reconstructed Ir(110)-(1x2) Surface, *Surface Sci.* 91: 440-448 (1980).
4. J. B. Pendry, "Low Energy Electron Diffraction," Academic Press, New York (1974).
5. M. A. Van Hove and S. Y. Tong, "Surface Crystallography by LEED," Springer-Verlag, New York (1979).
6. I. Guttman, S. S. Wilks, and J. S. Hunter, "Introduction to Engineering Statistics," Wiley, New York (1971).
7. G. E. P. Box, W. G. Hunter, and J. S. Hunter, "Statistics for Experimenters," Wiley, New York (1978).
8. G. Dahlquist and A. Björk, "Numerical Methods," Prentice-Hall, Englewood Cliffs, N. J. (1974).
9. N. R. Draper and H. Smith, "Applied Regression Analysis," Wiley, New York (1966).
10. D. J. Wilde and C. S. Beightler, "Foundations of Optimization," Prentice-Hall, Englewood Cliffs, N. J. (1967).
11. S. Lang, "Analysis I," Addison-Wesley, Reading, Mass. (1969).

Chapter VI

Theoretical Justification of Equivalent Beam Averaging for LEED

Theoretical Justification of Equivalent Beam Averaging for LEED

A. C. Sobrero* and W. H. Weinberg

Division of Chemistry and Chemical Engineering

California Institute of Technology

Pasadena, California 91125

* Current address: E.I. du Pont de Nemours and Co., Inc.; Wilmington, Delaware 19898; USA.

Abstract

The equivalent beam averaging procedure corrects LEED intensities to first order for systematic error due to angular misalignment of the incident beam. The method also corrects for misorientation of the surface plane or for large-scale variations in surface topography. High-order corrections for these errors can be obtained in the special case where equivalent beams are averaged coherently.

1. Introduction

Systematic errors are the bane of the experimentalist; unlike random errors, statistical averaging does not reduce their effect on the data and there is no simple prescription for eliminating them. Small errors persist despite great care in the preparation of the sample, the calibration of the instrument and the execution of the measurements. In low-energy electron diffraction (LEED) experiments, crystals are oriented typically only to within $\pm\frac{1}{2}°$ of the desired surface when they are cut, angles of incidence are not controlled to better than $\pm\frac{1}{2}°$, residual magnetic fields distort the beam paths, the point of incidence may be misaligned by a few millimeters, and so on. All of these errors noticeably degrade data from a high-resolution instrument (1) and to quantitatively assess the influence of such errors the complete experiment has to be replicated independently (2). A simple technique that can improve the quality of the data is welcomed.

A useful procedure for reducing the effects of angular misorientations has been presented by Davis and Noonan (3). The technique, known as equivalent beam averaging (EBA), relies on the averaging of beams that are equivalent under the point symmetry group of the ideal wavefield. The method has been justified on the empirical grounds that it improved the quality of the fit between computed and experimental intensity profiles in studies of the Cu(100) and Ag(110) surfaces (4). Numerical calculations have shown that EBA can mitigate against the effects of slight errors in the incidence angle and it has been suggested that EBA can reduce the errors due to beam divergence and variations in surface topography (3). Here we give a theoretical derivation of the technique demonstrating that this is in fact the case.

In Section 2 we show that when the only symmetry element is a mirror plane, the EBA technique corrects for alignment error perpendicular to the mirror plane to first order. For

surfaces with more than one mirror plane, or for any rotation axis including C_2, EBA corrects to first order for alignment error in both the polar and azimuthal directions. High-order correction is available when the beams can be averaged coherently.

2. Theory

The equivalent beam averaging technique relies on the fact that for any diffraction beam other than the specular reflection, the complex amplitude as a function of the incidence angle has the point group symmetry of the surface (5,6). The (00) beam is special since the reciprocity theorem (time reversal symmetry) requires that this beam have a twofold rotation axis normal to the surface, even if the surface itself has no such symmetry element (7,8). At normal incidence, the wavefield will have the complete point group symmetry of the surface, so this is where EBA is most useful.

Over most of the energy range of a LEED intensity-voltage spectrum, the scattered amplitude is an analytic function of the incidence angles. The exceptions occur near the grazing emergence conditions for new beams where there may be slope discontinuities in the intensity (9). Instrumental broadening will smooth out even this mild singularity, so we will proceed initially by assuming that the wavefield can be expanded in a Taylor series, checking a posteriori to see if the intensity is varying too rapidly as a function of incidence angle for this procedure to be justified.

Consider first the case of a perfectly oriented surface with a mirror plane and suppose that the incident beam lies in this plane. For any beam (h_0k_0) in the mirror plane, there is a symmetrically equivalent beam (h_1k_1). Denote the amplitudes of two equivalent beams by ψ_0 and ψ_1. If there is a slight misalignment, the incident beam will be tilted by an angle ζ with respect to the mirror plane. In the intervals where the wavefield is analytic, the amplitudes can be expressed in Taylor series with a positive radius of convergence

$|\zeta| < \zeta_0$ as

$$\psi_0(\zeta) = \psi + \zeta\psi_\zeta + \tfrac{1}{2}\zeta^2\psi_{\zeta\zeta} + 0(\zeta^3)$$

$$\psi_1(\zeta) = \psi - \zeta\psi_\zeta + \tfrac{1}{2}\zeta^2\psi_{\zeta\zeta} + 0(\zeta^3), \qquad (1)$$

where an unimportant phase shift has been ignored. The corresponding beam intensities are

$$I_0(\zeta) = \psi_0^*\psi_0 = \psi^*\psi + 2\mathrm{Re}(\zeta\psi^*\psi_\zeta) + \mathrm{Re}(\zeta^2\psi^*\psi_{\zeta\zeta} + \zeta'\zeta\psi_\zeta^*\psi_\zeta) + 0(\zeta^3)$$

$$I_1(\zeta) = \psi_1^*\psi_1 = \psi^*\psi - 2\mathrm{Re}(\zeta\psi^*\psi_\zeta) + \mathrm{Re}(\zeta^2\psi^*\psi_{\zeta\zeta} + \zeta'\zeta\psi_\zeta^*\psi_\zeta) + 0(\zeta^3) \qquad (2)$$

Thus, the average intensity is

$$\langle I\rangle = \tfrac{1}{2}(I_0 + I_1) = I + 0(\zeta^2). \qquad (3)$$

Averaging has corrected the intensities to first order for error in the azimuthal angle. The analysis can be carried a step further by noting that the linear combination

$$\delta = \tfrac{1}{2}(I_0 - I_1) = 2\mathrm{Re}(\zeta\psi^*\psi_\zeta) + 0(\zeta^3) \approx \zeta I_\zeta \qquad (4)$$

gives an estimate for the sensitivity of the data due to variations in the incidence angle. If the angle ζ is measured accurately, e.g., using a photographic technique (10), the derivative I_ζ is approximated by δ/ζ. The estimate of the variance

$$\varepsilon = [(I_0 - \langle I\rangle)^2 + (I_1 - \langle I\rangle)^2]^{1/2} = \sqrt{2}\,\delta \qquad (5)$$

can be used to weight the comparison between measured and computed intensities. When the observed variance is large, the energy is likely to be near a singularity in the intensity, and beam averaging is not justified. Hence, for both statistical and theoretical considerations, ε^{-1} should be used to weigh the comparison between measured and computed intensities.

Consider now a perfect surface with an n-fold rotation axis. At normal incidence, any beam $(h_i k_i)$ other than the specular will have n beams in its equivalence class. Denote the amplitude of the n equivalent beams by $\psi_0, \psi_1, \ldots, \psi_{n-1}$. Suppose now that the incident beam is slightly misaligned, making an angle of $\Omega = (\theta, \varphi)$ with respect to the surface normal. Converting to complex notation, let

$$z = \theta e^{i\varphi} \tag{6}$$

so that rotation by $2\pi/n$ is represented by $s = e^{2\pi i/n}$. In regions where $\psi(z)$ is free of singularities for $|z| < z_0$, defining the vectors

$$\Psi = (\sqrt{n})^{-1} \begin{bmatrix} \psi_0 \\ \psi_1 \\ \psi_2 \\ . \\ . \\ . \\ \psi_{n-1} \end{bmatrix} \qquad \Phi = \begin{bmatrix} \psi \\ z\psi^{(1)} \\ z^2\psi^{(2)}/2 \\ . \\ . \\ . \\ z^{n-1}\psi^{(n-1)}/(n-1)! \end{bmatrix} \tag{7}$$

gives the Taylor series expansion

$$\Psi = S\Phi + 0(z^n) \text{ for } |z| < z_0, \tag{8}$$

where the unitary matrix S is given by $S_{jk} = (\sqrt{n})^{-1} s^{jk}$. The average intensity is

$$\langle I \rangle = \Psi^* \Psi = \Phi^* \Phi + 0(z^n) = I + 0(z^2) \tag{9}$$

and again the first-order term has been eliminated. The sensitivity of the data can be estimated by

$$\delta = n^{-1} \left| \Sigma\, s^j I_j \right| = |zI_z| + 0(z^m), \tag{10}$$

where m = 2 for n odd, and m = 3 for n even. The higher derivatives of I cannot be estimated this way since they are confounded either with $\langle I \rangle$ or δ.

An interesting outcome from the analysis is that contrary to the accepted view that four equivalent beams are needed to correct for error in both the polar and azimuthal angles (3), any n-fold rotation, in particular C_2 and C_3, will achieve a first-order correction. Four spots are needed, however, when the only symmetry elements present are mirror planes.

In Equation (8), n terms were carried and the result of the averaging in Equation (9) was a first-order correction to the beam intensity. The second-order error term in $\langle I \rangle$ arises from the incoherent averaging of the n equivalent beams. If the wavefunctions could be summed coherently, the average intensity would be

$$\langle I \rangle = n^{-2} [\Sigma\, \psi_i]^* [\Sigma\, \psi_i]$$

$$= n^{-1}(\Psi^{*}\mathbf{1})(\mathbf{1}^{T}\Psi) + 0(z^{n})$$

$$= I + 0(z^{n}), \qquad (11)$$

where $\mathbf{1}$ is a nx1 vector of ones: $\mathbf{1} = (1\ 1\ 1)^{T}$. Hence, coherent averaging corrects the intensity to order n.

Experimentally, an approximation to coherent averaging is obtained when there are many symmetrically equivalent domains within the coherence area of the instrument. As is shown in Fig. 1, only the overlayer beams are averaged. The averaging will not be perfect since the areas covered by domains of each type will not be exactly equal. If p_i is the relative proportion of domain i per unit area, the amplitude of the wavefunction is

$$\Sigma\, p_i\psi_i = \psi + z\psi^{(1)}\Sigma\, p_i s^{i} + z^{2}/2!\ \psi^{(2)}\ \Sigma\, p_i s^{2i} + \ldots + z^{n-1}/(n-1)!\ \psi^{(n-1)}\ \Sigma\, p_i s^{n-i} + 0(z^{n}) \qquad (12)$$

If there is a large number of coherence areas within the beam, the expected value for the intensity is

$$\langle I\rangle = n(\Psi^{*}\mathbf{p})(\mathbf{p}^{T}\Psi)$$

$$= I + \sigma|z|I_{z} + 0(\sigma z^{2}) + 0(z^{n}), \qquad (13)$$

where the variance in the domain coverage is

$$\sigma = [(n-1)/\langle N\rangle n^{2}]^{1/2} \qquad (14)$$

and $\langle N\rangle$ is the average number of domains within a coherence area.

Finally, suppose that the incident beam is aligned perfectly normal to a high-symmetry plane of the crystal, but that the sample was misaligned slightly when it was prepared so that the actual surface is not exactly parallel to the high-symmetry plane. This situation is the dual of the previous cases. The systematic error discussed above concerned the misalignment of the wavevector or the incident beam, that is, an error in reciprocal space, while here there is a misalignment in real space. The previously developed equations can be carried over to the dual case by reinterpreting the variables ζ and z. Now, ζ is the azimuthal angle between the surface normal and a mirror plane or the

substrate, while z is given by Equation (6) with θ and φ being the angles between the surface normal and an n-fold rotation axis of the substrate. Hence, EBA intensities are correct to first order for a misorientation of the surface plane.

The case where both types of errors occur does not introduce anything new. Letting z and z^+ measure the errors in real and reciprocal space (or ζ and ζ^+, respectively, for σ_v symmetry), the Taylor series develops as

$$\psi_0 = \psi + JZ + Z^TGZ + 0(\|Z\|^3), \tag{15}$$

where

$$Z = \begin{bmatrix} z \\ z^+ \end{bmatrix} \qquad J = \frac{\partial \psi}{\partial Z} \qquad \text{and} \quad G = \frac{\partial^2 \psi}{\partial Z^2} \tag{16}$$

for $\|Z\| < Z_0$. Now, beam averaging gives first-order correction for both z and z+.

References

1. K. D. Gronwald and M. Henzler, Surface Sci. **117**, 180 (1982).

2. F. Jona, in *Determination of Surface Structure by LEED*, P. M. Marcus and F. Jona (eds.), Plenum, New York (1985).

3. H. L. Davis and J. R. Noonan, Surface Sci. **115**, 175 (1982).

4. H. L. Davis and J. R. Noonan, in *Determination of Surface Structure by LEED*, P. M. Marcus and F. Jona (eds.), Plenum, New York (1985).

5. D. A. King and D. P. Woodruff, eds., *The Chemical Physics of Solid Surfaces and Heterogeneous Catalysis*, Vol. 1, Elsevier, New York (1981).

6. B. W. Holland and D. P. Woodruff, Surface Sci. **36**, 488 (1973).

7. M. G. Lagally, T. C. Ngoc and M. B. Webb, Surface Sci. **20**, 444 (1971).

8. D. P. Woodruff and L. McDonnell, Surface Sci. **40**, 200 (1973).

9. J. I. Gersten and E. G. McRae, Surface Sci. **29**, 483 (1972).

10. A. C. Sobrero and W. H. Weinberg, Rev. Sci. Instrum. **53**, 1566 (1982).

Figure Caption

Figure 1: An asymmetric adsorbate on a C_4 site can produce four rotationally equivalent domains, leading to coherent averaging for the overlayer beams.

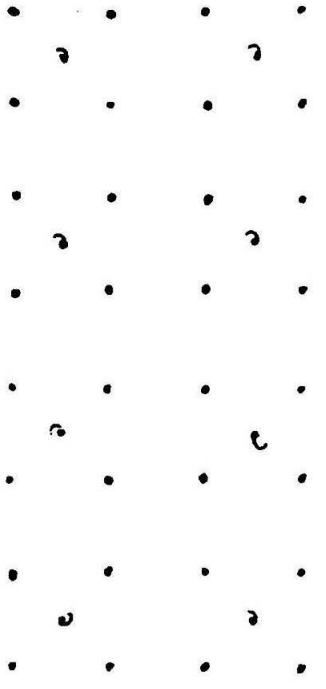

• = substrate lattice

= asymmetric adsorbate on C_4 site

(a)

rotational equivalent configurations

(b)

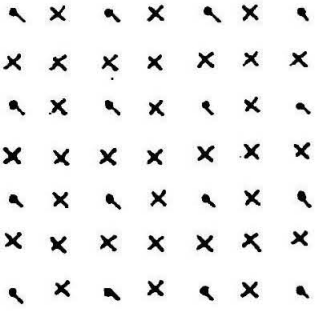

reciprocal lattice showing the effect on the amplitude of a small error in the incidence angle

= effect on substrate spots

× = effect on overlayer spots for four equivalent domains

(c)

Figure 1

Appendix 1

CO on Ru (001): Island Size and Disordering

CO on Ru(001): Island size and disordering

Ellen D. Williams,[a] W. H. Weinberg, and A. C. Sobrero

Division of Chemistry and Chemical Engineering, California Institute of Technology, Pasadena, California 91125
(Received 22 September 1981; accepted 8 October 1981)

Low-energy electron diffraction (LEED) has been used to study the influence of steps and of temperature variation on the formation of ordered islands of CO on the (001) surface of ruthenium. The clean surface was found to have steps two atoms (one hcp unit cell) high separated by terraces with an average width between 135 and 270 A. Widths of the beam profiles for the CO overlayer were measured as a function of coverage at 100 and 310 K. The coverage dependence requires that there be increasing numbers of islands per terrace at decreasing coverages. The temperature dependence of the overlayer was measured also. The frequency of the frustrated translational motion of the CO admolecules parallel to the surface is estimated to be 45 cm^{-1}. At fractional (ϑ) coverages up to 1/6, the ordered islands of CO disorder substantially below the desorption temperature. At $\vartheta = 1/3$, disordering is much less marked. The disordering behavior depends strongly on the distribution of sizes of islands in the overlayer. The correct distribution was determined and used to calculate the island sizes as a function of coverage. The mean number of CO molecules per island is 1000 at $\vartheta = 1/6$, 500 at $\vartheta = 0.14$, and 300 at $\vartheta = 0.12$.

I. INTRODUCTION

The interactions among chemically adsorbed molecules are of both practical and theoretical interest. In practical terms, lateral interactions clearly affect the diffusion and reaction of chemically adsorbed molecules.[1] The theoretical interest in lateral interactions arises because they represent a type of molecular interaction not observed in homogeneous systems. Interactions among chemically adsorbed molecules can arise as a result of a perturbation of the electrons of the metal near the surface or an elastic distortion of the surface by the adsorbed species.[2-9] The effects of lateral interactions are manifest in vibrational spectra of chemisorbed overlayers,[10,11] in thermal desorption mass spectrometry,[12,13] and, most strikingly, in low-energy electron diffraction (LEED).[14] Each of these measurements offers a different potential for the determination of lateral interaction energies. Only qualitative information is available via vibrational spectroscopies. Proper analysis of thermal desorption mass spectra allows the estimation of net attractive and repulsive interaction energies in overlayers. LEED, however, offers the possibility of determining both the size and directional dependence of the microscopic lateral interactions between chemisorbed species.

When molecules adsorb onto the regular array of binding sites of a single crystal surface, they often form ordered overlayers, observable by LEED, which have a periodicity greater than that of the substrate. This is a direct consequence of lateral interactions. The geometry of the overlayer provides immediate qualitative information concerning the interactions. Short-range repulsive interactions tend to cause vacancies in sites adjacent to an occupied site, thus increasing the periodicity of the overlayer. Attractive interactions allow the molecules to cluster into islands of ordered structure even at very low surface coverages if the temperature is sufficiently low. Increasing the temperature causes the ordered superstructure to disorder, resulting in a disappearance of the LEED pattern. This is a physical realization of the two-dimensional order–disorder transition that has been employed widely in theoretical studies of phase transitions.[15] The techniques and results of these studies therefore are directly applicable to an analysis of the ordered overlayers that form as a result of lateral interactions at surfaces.[16,17] LEED studies of order–disorder phenomena in overlayers have been carried out for a limited number of chemisorbed systems. Among the most thoroughly studied systems have been oxygen adatoms on W(110),[18-26] hydrogen adatoms on Ni(111),[27-30] and oxygen adatoms on Ni(111).[31-34]

An additional effect of lateral interactions, island formation, is accessible to study by LEED. Results from the adsorption of oxygen on W(110)[24,25,35] have shown that the oxygen adatoms cluster into many small islands, rather than forming one large island as would be expected from energetic considerations alone. It is reasonable to assume that the formation of small islands arises as the result of limitations on the diffusion of atoms or molecules across the surface. For the case of oxygen atoms on W(110), it appears that steps on the surface may act as barriers to diffusion, isolating the adatoms on distinct terraces. In other systems, it is possible that islands form as a result of a limited mobility of the adspecies even on a perfect surface. In either case, the mechanism of island formation will determine the distribution of sizes of islands at any given coverage. Therefore, quantitative studies of the size of ordered islands can provide information on the limitations of diffusion of molecules across the surface. Furthermore, it is well known[36-38] that finite size effects can influence strongly the nature of phase transitions. Detailed information concerning the dimensions of ordered structures on the surfaces, thus, may be crucial to a thorough understanding of order–disorder phenomena in chemisorbed overlayers.

In the following, we will discuss the results of a LEED investigation of the island formation and order–disorder behavior of CO on Ru(001). It is known that CO adsorbs

[a] Present address: Department of Physics and Astronomy, University of Maryland, College Park, Maryland 20742.

 0021-9606/82/021150-12$02.10

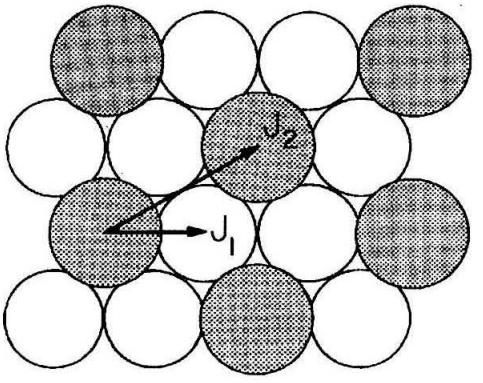

FIG. 1. The $(\sqrt{3}\times\sqrt{3})R$ 30° structure of CO on Ru(001). Arrows indicate the repulsive first neighbor interaction J_1 and the attractive second neighbor interaction J_2.

molecularly in the on-top site on Ru(001),[10,39] At fractional coverages up to $\vartheta=\frac{1}{3}$ (one CO per three surface Ru atoms, or 5.26×10^{14} CO/cm^2), the adsorbed molecules order into a $(\sqrt{3}\times\sqrt{3})$ R 30° superstructure (hereafter referred to as the $\sqrt{3}$ structure).[40–42] The formation of the $\sqrt{3}$ structure, in which nearest neighbor sites are unoccupied, indicates a repulsive first neighbor interaction. Results of thermal desorption[43] and infrared spectroscopic[10] measurements on this system indicate that there is an attractive second neighbor interaction between CO molecules which gives rise to island formation at low temperatures. The $\sqrt{3}$ structure with first and second neighbor interactions J_1 and J_2 is shown in Fig. 1. The experimental techniques used to study this system are described in the following section. In Sec. III, we present experimental data concerning island size, and change in island size with temperature. A detailed analysis of the data and the corresponding discussion are presented in Sec. IV. Section V contains a summary of our major conclusions.

II. EXPERIMENTAL METHODS

The experiments were carried out in an ion-pumped stainless steel ultrahigh vacuum system equipped also with liquid nitrogen cooled titanium sublimation pumping. The base pressure, following bakeout, was below 1×10^{-10} Torr. The system contains a quadrupole mass spectrometer and a single pass cylindrical mirror Auger electron spectrometer as well as four grid LEED optics and a movable Faraday cup for beam intensity measurements. The Faraday cup contains an einzel lens which is negatively biased to accept only those electrons of energy within approximately 0.5 eV of the energy of the incident beam. It also has been modified by replacement of the original collector cup by a channel electron multiplier.[44,45] A 0.13 mm diameter aperture on the Faraday cup was used in these experiments.

The Ru surface was oriented, cut, and polished to within 1° of the (001) plane using standard methods. The polished crystal was spotwelded to two parallel 0.025 cm diameter Ta heating wires which were clamped in a Cu holder which was part of a rotary manipulator assembly. Thermocouple leads of 5% Re/95% W and 26% Re/74% W were spotwelded together and then spotwelded to a small piece of Ta foil (approximately 1 mm^2 surface area) on the back of the crystal to make the junction. The crystal could be cooled to 100 K using liquid nitrogen refrigeration, and it could be heated resistively to above 1600 K. The thermocouple calibration of Sandstrom and Withrow[46] was used below 273 K. Cleaning procedures established previously[42] were used to keep the surface free of contaminants.

LEED beam profiles were measured by positioning the Faraday cup on the center of the profile and varying the energy of the electron beam to sweep the profile across the cup aperture.[47] Profiles measured in this way were corrected for the intensity variation of the beam with energy by division by the I–V curve. It was assumed in making this correction that there was no variation in beam width over the energy range of the beam profile. The energy width (FWHM) of the substrate beams ranged from approximately 1.5 eV at 37 eV to 3.4 eV at 95 eV. The FWHM of the $(\sqrt{3}\times\sqrt{3})$ R 30° overlayer beams ranged from 1.5 eV for the narrowest beam measured to 2.7 eV for the widest. Transformation of the beam profiles as functions of energy to functions of wave vector was done using

$$\left.\frac{\partial k}{\partial E}\right|_{\theta}=\frac{\sin\Theta}{2\sqrt{150.4}}\,E^{-1/2}, \tag{1}$$

where Θ is the angle of the diffracted beam with respect to the surface normal, E is the electron energy in eV, and k is the parallel component of the wave vector in Å^{-1}.[47] The bulk value of 2.7058 Å[40] was used for the nearest neighbor Ru–Ru distance on the unreconstructed (1×1) surface in calculating the values of k at the center of the diffracted beam profiles.

The overlayers of CO were prepared usually by adsorption at 350 K followed by cooling to either 100 or 310 K. This procedure was followed since it has been shown that direct adsorption at low temperature leads to a large density of defects (domain boundaries) in the overlayer at $\vartheta=\frac{1}{3}$.[49] To calibrate the coverage, the LEED intensity due to the $\sqrt{3}$ structure was measured as a function of exposure to CO at 330 K. The exposure at which a maximum in intensity occurs represents optimum ordering of the $\sqrt{3}$ structure and thus a coverage of $\vartheta=\frac{1}{3}$. The known constancy of the probability of adsorption of CO at room temperature up to $\vartheta=\frac{1}{3}$[41,50,51] was then used to relate lower coverages to exposure.

Measurements of the first order $\sqrt{3}$ beam profiles were carried out at an incident energy of 28 eV. One set of measurements was duplicated at an energy of 49 eV to confirm that multiple scattering effects did not change the measured width.[52] Incident beam fluxes of 1–10 nA/mm^2 were used to minimize electron stimulated desorption or dissociation of the CO.[53] Variation of intensity of the $\sqrt{3}$ beam with temperature was measured by monitoring the intensity of the beam while cooling from 400 K (desorption of CO begins above 400 K). Or-

dering and disordering of the overlayer with temperature was completely reversible: the intensity and width of the beam profile at 100 K remained unchanged following multiple heating and cooling cycles. The widths of the beam profiles are quite sensitive to the presence of oxygen on the surface. Even small amounts of oxygen contaminant cause substantial beam broadening. Care therefore was taken to keep the surface rigorously free of oxygen by techniques established previously.[42]

III. EXPERIMENTAL RESULTS

Three distinct sets of experiments were performed in this study of the adsorption of CO on Ru(001). First, profiles of the first-order LEED beams of the Ru(001) surface were measured as a function of electron energy to determine the instrument response function and the step density of the surface. Then, beam profiles for the $\sqrt{3}$ structure of the CO overlayer were measured for a variety of coverages at 100 and 310 K. Finally, the disordering of the $\sqrt{3}$ structure at temperatures up to 400 K was studied at three coverages by monitoring the LEED intensity as a function of temperature. Each of these sets of experiments is described below.

A. Instrument response and step density

The parameters determining the instrument response function are the energy spread of the incident electron beam ΔE, the diameter of the Faraday cup aperture d, the effective width of the incident electron beam D, and the angular spread (source extension) of the incident beam γ.[47,54] For this instrument, ΔE was determined to be 1.2 eV, using the einzel lens in the Faraday cup as a retarding field energy analyzer. The cup aperture is 0.13 mm, and the true beam width is approximately 1 mm, as estimated by moving the crystal across the beam. However, this width may be modified to a different effective width by a focusing action of the einzel lens. The source extension was not determined independently, but values of approximately 0.01 rad have been found for other similar instruments.[47,54]

To determine the values of D and γ and to measure the step density, the width of the first-order substrate beams was measured at energies between 35 and 90 eV. For a surface with a distribution of terraces of different sizes separated by steps, the beam profiles will become broader and narrower with changing energy.[54–57] The smallest measured width corresponds to the instrumental width.[54] Henzler[55] has derived a relationship for the energies at which broadening and narrowing should be observed for the (001) surface of an hcp lattice with steps of height equal to the lattice constant along the hexagonal axis (4.28 Å for Ru). These energies are indicated by arrows in Fig. 2 along with the experimentally determined values of the beam width. It is clear that the measured values are consistent with a model of the surface containing a distribution of steps of height 4.28 Å.

The degree of broadening of the beam profile is determined by the average distance between steps. The relative reduced width [the deconvoluted FWHM divided by the value of k for the beam[57]] of the broadened beams

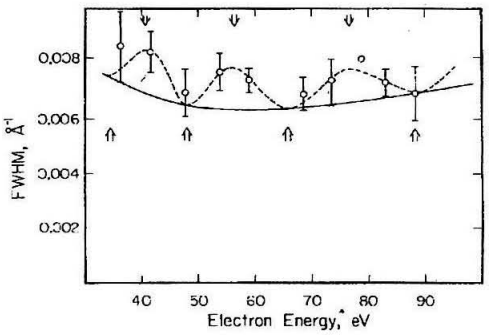

FIG. 2. FWHM of the first-order diffraction beams of the clean Ru(001) as a function of energy. Error bars represent the standard deviation determined from repeated measurements. Only one measurement was made of the point without an error bar. Arrows represent the energies at which maxima (down arrows) and minima (up arrows) are expected in the width [Ref. (55)]. The solid curve is the instrumental width. The dashed curve is drawn empirically as a guide to the eye.

shown in Fig. 2 is 1.0±0.3%. Depending on the model used for the distribution of terrace sizes, this indicates either terraces of width 100 lattice spacings (270 Å)[57] or of width 50 lattice spacings (135 Å).[58] These two estimates have been used as upper and lower limits on the step density. As discussed in Sec. IV A, on the basis of the island size determination, the upper limit seems to represent the surface more adequately.

The minima in the measured widths in Fig. 2 represent the width of the instrument response function. Using the predetermined values of ΔE and d, these minima were used to determine the values of D and γ from the known relationships between the parameters ΔE, d, D, and γ and the instrumental width as a function of energy and angle.[47,54] The values for these parameters were found to be $D = 0.05$ mm and $\gamma = 0.006$ rad. The small value of the effective width indicates that the einzel lens in the Faraday cup acts to discriminate against electrons not moving orthogonally to the detector. A collecting lens used by Park and co-workers[47] also reduced the effective beam diameter by essentially increasing the distance between the sample and the collector. For this instrument, the instrumental resolution is limited by the energy spread ΔE at low electron energies and by the source extension γ at higher energies.

Because the $\sqrt{3}$ beam occurs at a smaller angle with respect to the incident beam than does the substrate beam for the same electron energy, the width of the instrument response is narrower for the $\sqrt{3}$ beam. Using the experimentally determined values for ΔE, d, D, and γ, the width of the instrument response for the $\sqrt{3}$ beam is 0.0060 Å^{-1} at 28 eV and 0.0057 Å^{-1} at 49 eV. An uncertainty of ±0.0006 Å^{-1} is assigned to these values by comparison with the uncertainties in the widths of the substrate beam profiles.

B. Beam profiles of the CO overlayer

Beam profiles of the $\sqrt{3}$ structure formed by CO were measured at 100 and 310 K for a range of coverages as described in Sec. II. Profiles measured at 100 K for coverages of $\vartheta = \frac{1}{3}$ and $\vartheta = 0.10$ are shown in Fig. 3. At $\vartheta = \frac{1}{3}$, the FWHM of the beam profile is 0.0064 Å^{-1}, only slightly broader than the instrument response function. At $\vartheta = 0.10$, the FWHM is 0.0132 Å^{-1}. This increased width indicates that the CO molecules are present in ordered islands of limited size.

The measured profiles were corrected for the broadening due to the instrument response by a Fourier transform deconvolution. Since the measured profile $I_m(k)$ is the convolution product of the instrument response function $T(k)$ and the true beam profile $I_t(k)$,[47] the true profile can be recovered from the measured profile using the expression

$$I_t(k) = F^{-1}\left\{\frac{F[I_m(k)]}{F[T(k)]}\right\}, \qquad (2)$$

where F and F^{-1} are the forward and reverse Fourier transforms, respectively. The average of two $\sqrt{3}$ beam profiles that had the same FWHM as the instrument response (0.006 Å^{-1}) was used for the instrument response function $T(k)$. The measured beam profiles were symmetrized by averaging about their center prior to deconvolution. The application of Eq. (2) was quite sensitive to truncation of the profiles and to noise. Therefore, profiles were smoothed and their wings extended prior to taking the Fourier transforms.

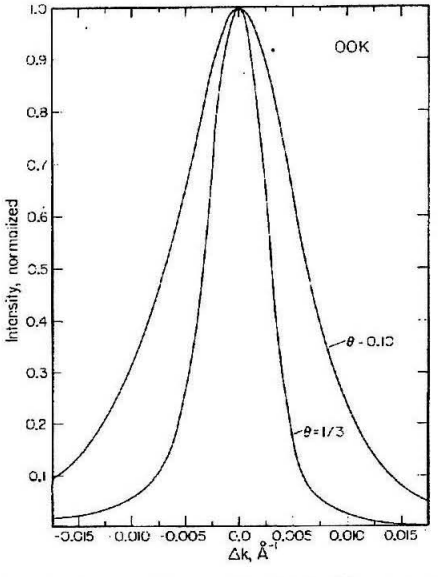

FIG. 3. Averaged beam profiles for the $\sqrt{3}$ structure at absolute coverages $\vartheta = \frac{1}{3}$ and $\vartheta = 0.10$ measured at 100 K. The profile for $\vartheta = \frac{1}{3}$ is the average of nine measured profiles, that at $\vartheta = 0.10$ is the average of five. Measurements were made with an incident electron energy of 28 eV. $\Delta k = 0$ is the center of the $\sqrt{3}$ beam profile, at $k = 0.2464$ Å^{-1}.

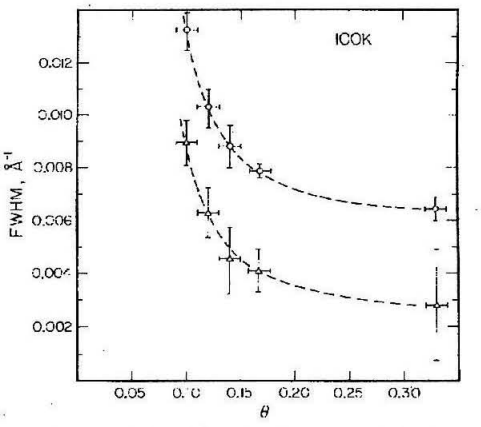

FIG. 4. FWHM of the $\sqrt{3}$ beam profile as a function of coverage at 100 K. Circles o measured widths at incident electron energy of 28 eV. Triangles Δ widths corrected for instrument response by deconvolution. Error bars on FWHM are the standard deviation determined from repeated measurements. Error bars on the coverage are estimated from the known reproducibility of exposure.

The widths of profiles measured at 100 K for coverages from $\vartheta = \frac{1}{3}$ are shown in Fig. 4 before and after deconvolution. The width increases steadily as the coverage decreases. This shows that, as might be expected, smaller islands form at lower coverages. Values of the widths shown in Fig. 4 as well as widths measured at 310 K are listed in Table I. The standard deviation in the widths of the deconvoluted profiles was calculated using the error propagation equation appropriate for the deconvolution of two Gaussian functions.

TABLE I. Widths of beam profiles in Å^{-1} for $\sqrt{3}$ structure at different coverages and temperatures. FWHM_m and σ_m are the measured width and standard deviation. FWHM_t and σ_t are the width and standard deviation following deconvolution to correct for the instrument response. Values for $\vartheta = \frac{1}{3}$ at 100 and 310 K are combined as they are identical.

T	ϑ	FWHM_m	σ_m	FWHM_t	σ_t
100 K	$\frac{1}{3}$	0.0064	0.0005	0.0028	0.0021
	$\frac{1}{6}$	0.0079	0.0002	0.0041	0.0008
	0.14	0.0088	0.0008	0.0046	0.0012
	0.14[a]	0.0090	0.0002	0.0049	0.0007
	0.12	0.0103	0.0007	0.0063	0.0010
	0.10	0.0132	0.0007	0.0090	0.0009
310 K	0.20	0.0068	0.0006	0.0030	0.0017
	$\frac{1}{6}$	0.0089	0.0005	0.0058	0.0009
	0.14	0.0155	0.0015	0.0115	0.0016

[a]Value measured at 49 eV incident energy. All other values measured at 28 eV incident energy.

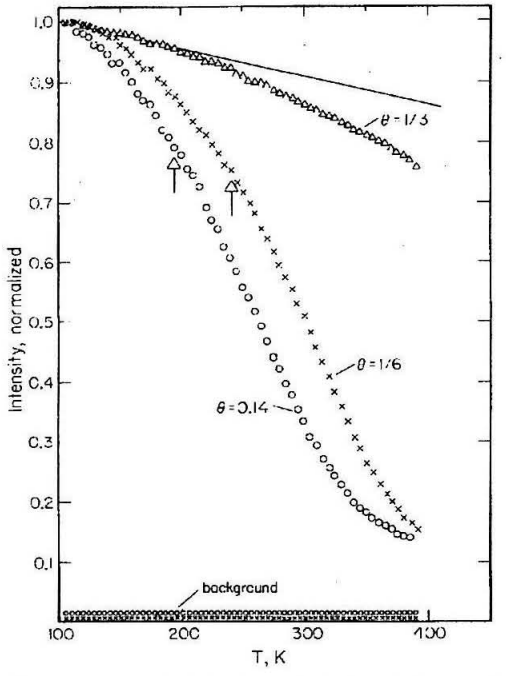

FIG. 5. The variation with temperature of the intensity at the center of the $\sqrt{3}$ beam profile for $\vartheta=\frac{1}{3}$, $\frac{1}{6}$, and 0.14. The variation of the background intensity at $\vartheta=\frac{1}{6}$, x's and at $\vartheta=0.14$, is also shown. Arrows indicate the temperatures at which the beams begin to broaden. The smooth curve is the calculated decrease in intensity due to frustrated translational motion of the CO parallel to the surface with a frequency of 45 cm^{-1}.

At $\vartheta=\frac{1}{3}$, the optimum coverage for the $\sqrt{3}$ structure, there is no difference between the FWHM at 100 and that at 310 K. For lower coverages, $\vartheta=\frac{1}{6}$ and $\vartheta=0.14$, the FWHM increases with the temperature. This indicates a decrease in island size which must be due to loss of CO molecules from the islands. For $\vartheta=0.12$, the beam profile is so weak and broad at 310 K as to be unmeasurable. At lower coverages still, no intensity due to the $\sqrt{3}$ structure can be seen at all at 310 K. The good agreement between the deconvoluted widths of the profiles measured at 28 and 49 eV indicates that the use of the kinematic (single scattering) approximation is adequate for the present analysis.

C. Temperature dependence of the CO overlayer

Changes in the CO overlayer with temperature were first monitored by measuring the temperature dependence of the intensity of the beam profile at its center. The results for three different coverages are shown in Fig. 5. At $\vartheta=\frac{1}{3}$, there is only about a 20% decrease in intensity between 100 and 400 K. At $\vartheta=\frac{1}{6}$ and $\vartheta=0.14$, however, there is a dramatic decrease in intensity with increasing temperature.

Some decrease in intensity with temperature is expected due to the displacement of the CO molecules from their optimum positions on the surface as a result of vibrational motion. The expected intensity variation is[59]

$$I=I_0\exp(-2W), \tag{3}$$

where

$$2W=(2\pi)^2\sum_q|\Delta s\cdot u_q|^2, \tag{4}$$

Δs is the change in the electron beam wave vector, and u_q is the displacement in the q direction. The vibrational frequencies of CO are 2021 cm^{-1} for the carbon–oxygen stretch,[10] 445 cm^{-1} for the metal–carbon stretch,[39] in the range of 400 to 600 cm^{-1} for the frustrated rotational motion,[60-61] and between 34 and 126 cm^{-1} for the frustrated translational motion parallel to the surface.[60-62] Of these, only the frustrated translational modes are sufficiently low in frequency to cause a measurable change in the mean displacement of CO between 100 and 400 K. Hosemann and Bagchi[59] have derived the mean square displacement with temperature of a three-dimensional harmonic oscillator. A similar derivation for a two-dimensional harmonic oscillator gives

$$|u_{\parallel}|^2=\frac{h}{8\pi^2\nu m}\left\{\frac{1}{2}+\frac{1}{\exp(h\nu/k_BT)-1}\right\}, \tag{5}$$

where $u_{\parallel}$ is the displacement parallel to the surface, ν is the vibrational frequency, and m is the mass of the CO molecule, which has been treated as a single particle. Equations (4) and (5) were used to calculate the intensity variation with temperature for a range of values of ν. The most satisfactory fit to the experimental data was obtained for $\nu=45$ cm^{-1}. The calculated intensity variation is shown by the solid curve in Fig. 5. Up to approximately 220 K, the observed decrease in intensity at $\vartheta=\frac{1}{3}$ can be attributed to vibrational motion. Above that temperature, an additional type of disorder must occur. Site disorder, in which CO molecules occupy "incorrect" sites in the lattice with respect to the $\sqrt{3}$ structure, is the obvious example. It seems likely that site disorder at $\vartheta=\frac{1}{3}$ will begin at domain boundaries, only becoming prevalent throughout the overlayer at high temperature.

From measurements at 310 K, it is known that the beam profiles at $\vartheta=\frac{1}{6}$ and $\vartheta=0.14$ broaden with increasing temperature. To monitor this change in shape, the intensities at different points on the profile were measured as a function of temperature. As a profile broadens, the intensity in the wings of the profile will decrease less rapidly than the intensity at the center. This behavior is illustrated for $\vartheta=0.14$ in Fig. 6. Three intensity–temperature curves are plotted together: one was measured at the center of the profile, and the other two at quarter-maximum intensity. Each curve was normalized independently. The slower decrease in intensity at the quarter-maximum points, which indicates broadening, is apparent. The ratio of the intensity at quarter-maximum to that at the center, hereafter referred to as the width ratio, shows the broadening with temperature even more clearly. The onset of an increase in the width ratio is abrupt, occurring at a

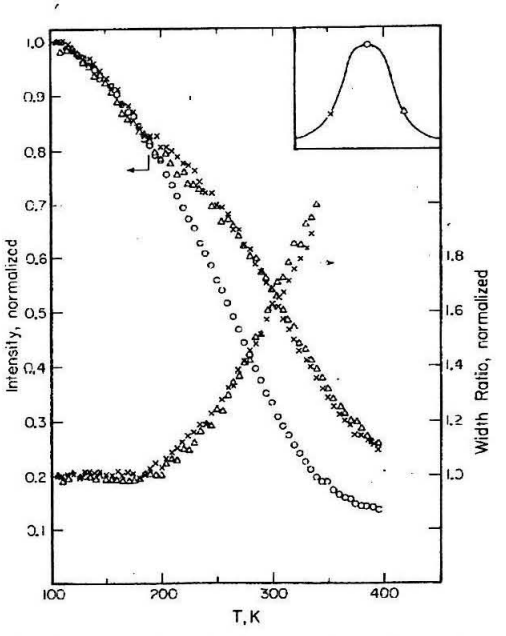

FIG. 6. The variation with temperature of the intensity at three different positions on the beam profile. Circles measured at the maximum of the beam profile, triangles, and x's measured at one-fourth maximum as illustrated schematically in the inset. Each curve has been normalized independently to unity at 100 K. The ratio of the curves measured in the wings of the profile to the curve measured at the center is also shown for the same points.

temperature of 195± 5 K. The same type of behavior is observed at $\vartheta=\frac{1}{6}$, with the onset of broadening at 240 ± 10 K. The temperatures at which the width ratio begins to change are indicated with arrows in Fig. 5. At $\vartheta=\frac{1}{3}$, the width ratio is constant up to 400 K. This confirms the previous observation that the FWHM of the beam at $\vartheta=\frac{1}{3}$ is the same at 100 and 310 K.

The abrupt onset of beam broadening, which occurs after the intensity has decreased by approximately 20%, is somewhat surprising. Intuitively, one would expect the profile to begin to broaden gradually as the intensity decreases, as has been observed for oxygen adatoms on W(110).[24] An explanation of this behavior is presented in Sec. IV B.

IV. ANALYSIS AND DISCUSSION

An analysis of the results presented in the preceding section is divided into two categories that initially appear to be distinct. The first category is the analysis of the widths of the beam profiles to determine the size, and possibly the mechanism of formation of the islands. The second category is the analysis of the ordering and disordering of the islands with temperature to determine the CO–CO lateral interaction energies and to compare with theoretical phase diagrams. However, during the analysis, it will become apparent that the island size distribution and the order–disorder behavior are strongly related. In the following subsection, we shall describe first the analysis of the island size distributions insofar as it can be carried out without reference to the order–disorder behavior. In the second subsection, the order–disorder behavior and its relationship to the island size distribution are discussed. Finally, the results are compared with theoretical phase diagrams for the $\sqrt{3}$ structure in the third subsection.

A. Island sizes

In principle, the mechanism of formation of the islands determines the distribution of island sizes.[63] There are two possible reasons for the formation of small islands. The first is step-limitation of adatom diffusion.[35] If steps act as barriers to diffusion, then adatoms will be trapped on the terrace on which they initially are adsorbed. The size distribution of the islands, thus, will be determined by the size distribution of the terraces. Except at extremely low coverages, this model requires that there be a constant number of islands which vary in size directly with coverage. In the following discussion, the phase "strict step-limited model" will refer to the case where there is little or no diffusion across step edges and only one island on a terrace. A second possible reason for the formation of small islands is a limited adatom diffusion distance. In this model, adatoms, which initially are adsorbed near one another, merge to form small islands. Once formed, the configuration with many small islands may represent a local minimum in the free energy, with an activation barrier to the formation of a single large island.

In practice, only for the step-limited model of island formation have size distributions been predicted.[35,57] The experimental beam widths were analyzed using these distributions as well as three semiempirical size distributions. The relation[64]

$$I(k)=N\sum_{M}P(M)\,I_{M}(k)\,, \tag{6}$$

where N is the number of islands, $P(M)$ is the probability of occurrence of an island containing M molecules, and $I_M(k)$ is the beam profile due to a single island with M molecules, was used to calculate beam profiles for comparison with experiment given a distribution of sizes $P(M)$. A set of 34 $I_M(k)$ was calculated for values of M ranging from 59 to 4955, with the molecules arranged in round islands. The 34 island sizes were chosen to represent constant increments in the value of the diameter of the islands. Thus, the increments in M are smaller at smaller values of M where the width of the beam profile varies more rapidly with island size. The summation in Eq. (6) was carried out over this set of values of M, with $P(M)$ replaced by $P(M)\Delta M$. The results of the analysis for each of the five size distributions is described below.

1. Geometrical distribution

Lu and co-workers[35,58] have developed a geometrical distribution for terrace widths Γ:

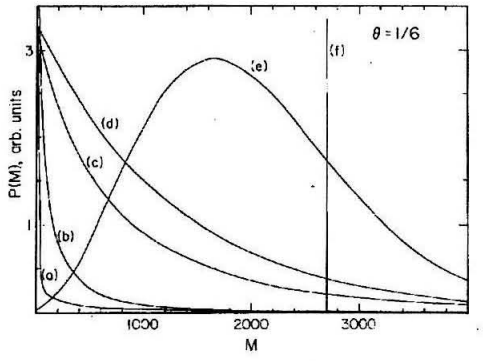

FIG. 7. Probability of observing an island containing M molecules as a function of M for (a) geometrical distribution. (b) Henzler's distribution, (c) empirical distribution (described in Sec. IV B), (d) ball-in-urn distribution, (e) distance distribution, and (f) delta function distribution. Each distribution gives rise to a beam profile of width 0.0041 Å^{-1} as observed for $\vartheta = \frac{1}{6}$ at 100 K.

$$P(\Gamma) \sim (1-\beta)^{\Gamma-1}\,\beta\,, \tag{7}$$

where β is the probability of encountering a step between two surface atoms in a given direction, and Γ is the width of the terrace in the number of surface atoms. An analysis of the step distribution for the surface used in this study based on Eq. (7) indicates that the mean terrace width is approximately 50 Ru atoms (Sec. II A). This corresponds to a value of $\beta = 0.02$. If the islands are step-limited, the size of an island will be determined by the overall coverage and the size of the terrace on which it resides by

$$M = \vartheta\Gamma^2\,, \tag{8}$$

where M is the number of molecules in the island, and where it has been assumed that on the average, terraces will have uniform widths in two dimensions. Using this model, the calculated FWHM of the beam profile varies only slightly (from 0.0040 to 0.0042 Å^{-1}) between $\vartheta = \frac{1}{6}$ and $\vartheta = 0.10$. It is apparent that using a constant average terrace width, this model cannot predict the rapid change in FWHM with coverage at intermediate coverages that is observed experimentally. Only if the value of β is allowed to vary substantially with coverage, which corresponds to allowing more than one island per terrace at low coverages, can the experimental values be reproduced. Curve (a) in Fig. 7 shows the island size distribution (with $\beta = 0.022$) that gives the correct FWHM for $\vartheta = \frac{1}{6}$ at 100 K.

2. Henzler's distribution

Henzler[57] has proposed a distribution for the terrace width distribution given by

$$\Gamma P(\Gamma) \propto \Gamma \exp\left[-\left(\frac{\Gamma}{w}\right)^E - \left(\frac{w}{\Gamma}\right)^E\right]\,, \tag{9}$$

where $E \simeq 0.8$ and w is an adjustable parameter determining the mean terrace width. Based on this distribution, the mean terrace width on the Ru surface was found to be approximately 100 Ru atoms, as discussed in Sec. III A. A value of $w = 40$ in Eq. (9) gives this mean terrace width. Equation (8) again was used to relate M to Γ, so that Eq. (9) could be used to predict island size distributions. As with the geometrical distribution, the requirement of islands limited by terrace size results in a very slow variation of FWHM with coverage between $\vartheta = \frac{1}{6}$ and $\vartheta = 0.10$. (The range of the value of the FWHM was 0.0036 Å^{-1} at $\vartheta = \frac{1}{6}$ to 0.0037 Å^{-1} at $\vartheta = 0.10$.) A fit to the experimental data requires a different value of w, or a varying number of islands per terrace at each coverage. The distribution that corresponds to the correct beam profile width at $\vartheta = \frac{1}{6}$ ($w = 17$ and mean terrace width = 41 Ru atoms) is shown by curve (b) in Fig. 7.

3. Ball-in-urn distribution

If there is a fixed number of nucleation sites N for islands, then an island size distribution can be determined from the number of ways of distributing n adsorbates among those sites. The result is[54]

$$P(M) \propto \frac{\Omega'(N, n, M)}{N\Omega(N, n)}\,, \tag{10}$$

where

$$\Omega(N, n) = \frac{(N-1+n)!}{(N-1)!\,n!}$$

and

$$\Omega'(N, n, M) = N\,\frac{(N-2+n-M)!}{(N-2)!\,(n-M)!}\,.$$

A different number of nucleation sites had to be used for each coverage to fit the experimental data with this distribution. This is consistent with the results of the prior two analyses that the experimental values are incompatible with a model that requires a fixed number of islands at all coverages. Curve (d) in Fig. 7 shows the ball-in-urn distribution ($N = 2100$ and $n = 2\,666\,667$ for a 4000×4000 Ru atom surface) which gives the value of the FWHM measured for $\vartheta = \frac{1}{6}$ at 100 K.

4. Distance distribution

A computer simulation based on a very simple model of diffusion-limited island nucleation was used to generate probability distributions for the nearest-neighbor distance between island centers τ that are Gaussian in τ.[54] The width of the distributions increases approximately linearly with the mean distance τ_0. Assuming that the number of molecules in an island is related to the distance to its nearest neighbor by $M = \vartheta\tau^2$, distributions of island sizes were generated using this model. A decreasing value of τ_0 with decreasing coverage was required to fit the measured values of the FWHM. This suggests, as do the prior results, that there are more but smaller islands present at lower coverages. The failure of this model to fit the experimental data with a constant value of τ_0 indicates that the model used to generate this distribution is too simple to describe the overlayer correctly. Curve (e) in Fig. 7 represents

the distance distribution ($\tau_0 = 106$ Ru atoms) for $\vartheta = \frac{1}{6}$ at 100 K.

5. Delta function distribution

For comparison with the other distributions, a distribution in which there is only one island size was also considered. The delta function distribution for $\vartheta = \frac{1}{6}$ is shown by curve (f) of Fig. 7.

Figure 7 amply demonstrates that knowledge of the width only of a beam profile is insufficient to determine the island sizes. In addition, use of the delta function distribution to analyze the size does not give the mean size in any sense, but at best an upper limit to the mean size.[64] Knowledge of the coverage dependence of the beam width can be used to test specific models for the size distribution. In this case, models that require a fixed number of islands fail to fit the experimental data because they cannot generate the rapid change in full width with coverage that is observed. This indicates that neither a strict step-limited model nor a defect-nucleation model are correct for this system. The distance–distribution also seems to be incorrect, since a varying value of τ_0 with coverage is necessary to fit the experimental data. This indicates that the assumptions used in deriving this distribution[64] do not describe adequately the diffusion of CO on the Ru(001) surface.

B. Disordering and island size

As shown in Figs. 5 and 6, no change in the width of the low-coverage beam profiles with increasing temperature is observed until the intensity has decreased by approximately 20%. This seems a somewhat surprising result. The I–T behavior at $\vartheta = \frac{1}{3}$ indicates that there is no site disorder within the $\sqrt{3}$ structure below approximately 220 K. Thus the decrease in intensity must be due to loss of CO molecules from the islands. But as CO molecules leave the islands, the islands become smaller and the FWHM larger. Therefore, it might be expected that changes in intensity and FWHM would occur simultaneously. This has in fact been observed for oxygen adatoms on W(110).[24] However, it is possible that the size distribution of the islands could modify this simple prediction. Since the height of a beam profile for a single island $I_m(k)$ is proportional to the square of the number of molecules in the island, large islands overwhelmingly dominate in determining the overall profile [Eq. (6)]. On the other hand, the FWHM of the profile for a single island is inversely proportional to the diameter of the island, so that the FWHM changes very rapidly with size for small islands and more slowly for large islands. Using these considerations, it can be seen that if small islands totally dissolve, it will tend to decrease the FWHM. If, at the same time, large islands lose some fraction of their molecules, the intensity will decrease, and the FWHM will increase slightly. For the correct distribution of island sizes, it is possible that the two influences on the FWHM will cancel until the intensity has dropped appreciably. To test this hypothesis, a simple model of the disordering process was considered for step-limited and nonstep-limited models of island formation.

The disordered phase of CO was tested as a two-dimensional ideal gas, and the $\sqrt{3}$ structure as a $2D$ solid. The chemical potentials of the two phases were calculated and equated to determine the number density of disordered CO molecules as a function of temperature. The partition function for the $2D$ gas is

$$Q_g = \frac{1}{N_g!}\left(\frac{2\pi m k_B T}{h^2} A_g\right)^{N_g} q_{\rm int}^{N_g}, \tag{11}$$

where N_g is the number of $2D$ gas molecules, m is the mass, A_g is the surface area available to the molecules (total area minus the area covered by islands), and $q_{\rm int}$ is the internal partition function of a single molecule. In the $2D$ solid, it is assumed that all the molecules are ordered in the $\sqrt{3}$ structure, i.e., there is no occupancy of nearest neighbor sites. If the vibrational modes of the CO remain independent in the $2D$ solid (the CO–CO distance is 4.7 Å), the partition function for an island for which the edge molecules are a negligible fraction of the total is

$$Q_s = q_{\rm int}^{N_s} \exp\left(\frac{-6N_s J_2}{2k_B T}\right), \tag{12}$$

where N_s is the number of molecules in the $2D$ solid and J_2 is the interaction energy for CO molecules in second nearest neighbor sites. In both Eqs. (11) and (12), the zero of energy has been taken as the minimum of the potential energy well for binding of a CO molecule to the surface. Equating the chemical potential for the solid and gas gives

$$\vartheta_g = \frac{N_g}{A_g} = \left(\frac{2\pi m k_B T}{h^2}\right)\left(\frac{q_{{\rm int},g}}{q_{{\rm int},s}}\right)\exp\left(\frac{6J_2}{2k_B T}\right). \tag{13}$$

The internal partition functions for molecules in the gas and solid were taken to be the same, except for a minor difference due to the different carbon–oxygen stretching frequencies.[10]

For a finite size island, the energy will be less than $6J_2N_s/2$ since the molecules at the edge of the island have a coordination smaller than six. The number of molecules at the edge of the island will be proportional to the square root of the number in the island, so that the total energy is

$$E = \frac{6J_2 N_s}{2} - cJ_2\sqrt{N_s}, \tag{14}$$

where c is a constant taking into account the coordination of the edge molecules and the proportionality of $\sqrt{N_s}$ to the number at the edge. Using this value of E in the partition function for the solid, the new value for the $2D$ gas phase density is

$$\vartheta_g' = \vartheta_g \exp\left(\frac{-cJ_2}{k_B T\sqrt{N_s}}\right). \tag{15}$$

In a step-limited model of island formation, each island is located on a terrace, isolated from all other islands. Thus, Eq. (15) can be used directly to calculate the $2D$ gas-phase density on each terrace as a function of temperature. Once ϑ_g' is known, the change in size of the island follows immediately, and the beam profile can thus be calculated as a function of temperature. For comparison with experiment, the calculated profiles

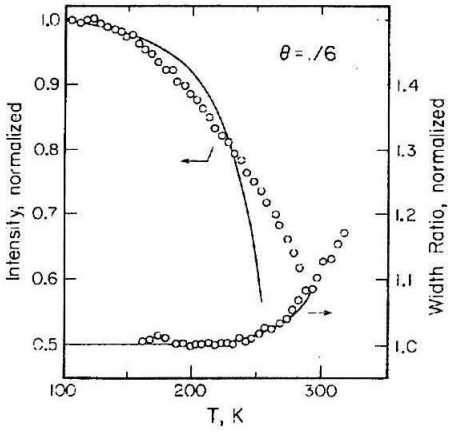

FIG. 8. Comparison of calculated (solid curves) and experimental (circles) intensity and width ratio as functions of temperature. An arbitrary size distribution (see text) and a value of $J_2 = -1.28$ kcal/mol were used in the calculation. The calculated intensity has been multiplied by $\exp(-2W)$ [see Eq. (4)].

were numerically convoluted with a Gaussian "instrument response function" of width 0.006 Å^{-1}. This calculation was carried out for distributions (a), (c), (d), (e), and (f) in Fig. 7. The calculation was quite successful in duplicating the sudden onset of change in the width ratio. However, for none of the size distributions did the intensity drop by more than 10% before the width ratio began to change. In addition, only a 10 K difference between the intensity curves at $\vartheta = \frac{1}{6}$ and $\vartheta = 0.14$ was calculated, in contrast to the observed difference of 30 K or more (Fig. 5).

If the islands are not step-limited, then all the islands in the overlayer should be considered in calculating the partition function for the $2D$ solid. A direct approach to this problem was not attempted. Instead, an approximate method was used. The overall $2D$ gas density was calculated using Eq. (13). It was then assumed that all islands lose CO molecules from their edges at the same rate, with a correction term for the higher energy of smaller islands as in Eq. (15), until the correct overall $2D$ gas density was reached. Inclusion of the energy correction term causes small islands to lose molecules from their edges at a greater rate than large islands. Omission of this term causes a distribution to act like a distribution with a slightly larger mean island size. Beam profiles were calculated as for the step-limited model. It was found that for different distributions of island sizes, the onset of change of the width ratio was shifted to higher temperatures as the mean island size became smaller. This is in agreement with our qualitative argument concerning the relative effects of a loss of CO molecules from small and large islands in the FWHM. For the ball-in-urn distribution, the intensity decreased by 10% before beam broadening was observed. For the geometrical distribution, the profile actually became narrower with increasing temperature as the large number of small islands in that distribution preferentially disordered. Therefore, a distribution intermediate in shape between these two was sought. An empirical distribution of the form

$$P(M) \propto (1-b)^{M^{3/4}}, \tag{16}$$

where b is an arbitrary constant, was found to give the correct relative behavior of intensity and width with temperature. The distribution used at $\vartheta = \frac{1}{6}$ is shown in curve (c) of Fig. 7. The calculated intensity and width ratio for $J_2 = -1.28$ kcal/mol is compared with the experimental data in Fig. 8. The calculation reproduces the delayed onset of broadening quite successfully, although the shape of the calculated intensity curve is not correct. Also, the more rapid increase in width with temperature at $\vartheta = 0.14$ than at $\vartheta = \frac{1}{6}$ is predicted by the calculation. However, as for the step-limited model, the observed difference in temperature between the two intensity curves is not reproduced. The best fit to both sets of data ($\vartheta = \frac{1}{6}$ and $\vartheta = 0.14$) therefore occurs with $J_2 = -1.20$ kcal/mol which places the calculated curves for $\vartheta = \frac{1}{6}$ approximately 10 K too low and those for $\vartheta = 0.14$ approximately 10 K too high in temperature.

Three major approximations were made in deriving the partition functions for the $2D$ gas and $2D$ solid [Eqs. (11) and (12)]. The first two were: (1) treating the disordered phase as an ideal gas and (2) equating the internal partition functions of molecules in the two phases. Modification of these two approximations causes the calculated intensity and width ratio curves to change mainly by a shift along the temperature axis. Thus, these two approximations affect the estimate of J_2 most strongly. The third approximation, that site-disorder does not occur within the islands, is best at low temperature. Inspection of the intensity–temperature curve at $\vartheta = \frac{1}{3}$ (Fig. 6) shows that this is a rather reasonable approximation over the temperature range for which the calculations were performed. The relative behavior of the intensity and the width ratio are not influenced greatly by these approximations. Therefore, conclusions based on calculations of these two quantities can be given a rather high degree of credence.

It was not possible to fit the experimental intensity and width ratio curves if it is assumed that CO molecules cannot cross steps and that, thus, the density of the disordered phase about an island is due to loss of CO molecules from that island alone. If the number of CO molecules lost from each island is proportional to the number of molecules at the edge of the island (and this is a very reasonable approximation), it is possible to fit the experimental curves only with one model for the island size distribution. It is therefore concluded that curve (c) of Fig. 7 represents the physical distribution of island sizes, although Eq. (16), used to describe it, is only an empirical equation. Therefore, the mean island sizes have been determined by varying the parameter b in Eq. (16) to produce profiles of the widths measured at 100 K. The results are compared with the values calculated using the delta function distribution in Table II. In making these calculations, it has been assumed that the width measured at 100 K is the narrowest width that will occur at each coverage. This has been shown to be

TABLE II. Mean island size and diameter for the correct distribution described in Sec. IV B, and the delta function distribution. b is the value of the parameter used in Eq. (16).

	Correct distribution			Delta function distribution	
ϑ	b	$\bar{M}$	$\bar{d}$, Å	M	d, Å
$\frac{1}{6}$	0.008	1000	140	2700	255
0.14	0.014	500	95	1700	215
0.12	0.019	300	75	1100	165
0.10	0.032	160	85	560	115

correct experimentally for $\vartheta=\frac{1}{6}$ and $\vartheta=0.14$. Extrapolating the behavior at $\vartheta=\frac{1}{6}$ and $\vartheta=0.14$, it appears that the onset of broadening at $\vartheta=0.12$ is near 100 K, and at $\vartheta=0.10$, it is probably below 100 K. Therefore, the calculated island sizes are correct for $\vartheta=\frac{1}{6}$, 0.14, and 0.12, and probably somewhat small for $\vartheta=0.10$. As shown in Table II, regardless of the distribution used to calculate the mean island size, the mean size decreases with coverage far more rapidly than linearly. This demonstrates that there are increasing numbers of islands with decreasing coverage.

Both the coverage dependence of the beam widths and the behavior of intensity and width with temperature show that a strict step-limited model for island growth is not correct for CO on Ru(001). While the maximum size an island can attain is obviously limited by the size of the terrace on which it is located, at low coverages there is some limit to the mobility of the CO molecules which causes more than one island to form on a single smooth terrace. In addition, analysis of the disordering behavior of the islands has shown that the size distribution must be of the shape of curve (c) in Fig. 7, which can be described by Eq. (16). The shape of this curve places a lower limit on the size distribution of terraces, since the terraces must be large enough to accommodate the islands. The geometrical distribution[35,58] with a step density of 2% (Sec. III A) has a very small proportion of large terraces and would not allow the formation of the island size distribution of Fig. 7(c). Henzler's distribution[57] with a step density of one percent (Section III A) has a very slow decay with increasing terrace width, and could easily accommodate the proposed island sizes. It appears, therefore, that the broader distribution describes the step density on this surface more accurately.

C. Comparison with phase diagrams

The dissolution of ordered islands into a disordered phase is a first-order transition. In these experiments, the disordering was monitored under conditions of constant $2D$ density (coverage). For these conditions, the disordering will take place over a range of temperature, and the transition temperature will be that at which the ordered phase disappears completely. This point is observable by LEED as the temperature at which the integrated intensity in the overlayer beam profile effectively goes to zero.[36] Quantitative measurements of these temperatures were not made in this study. However, from the experiments that were performed, a clear trend in the dependence of the transition temperature on coverage appears. Extrapolation of the intensity versus temperature curves at $\vartheta=\frac{1}{6}$ and $\vartheta=0.14$ shows that the transition temperatures are well above 400 K for these two coverages. At $\vartheta=0.12$, there is only a weak profile observable at 310 K, indicating a transition temperature between 310 and 400 K. No profile is observable at $\vartheta=0.10$ at 310 K, which shows that the transition temperature is $\lesssim 310$ K. The results indicate that the transition temperature decreases very rapidly with coverage.

Phase diagrams have been calculated for overlayers on a triangular substrate such as Ru(001), with attractive second and repulsive first nearest-neighbor interactions in the ratios $J_2/J_1=-1$[65] and $J_2/J_1=0$.[66–69] In the case where the second neighbor interaction is zero, no ordered structure forms at any temperature below a coverage of approximately 0.28.[66,67] Above that coverage, an ordered structure does form and disorders with increasing temperature via a second-order phase transition. The maximum transition temperature occurs at $\vartheta=\frac{1}{3}$ and has a value of $k_B T/J_1 \simeq 0.35$.[68,69] When the attractive second neighbor interaction is added, the transition temperature at $\vartheta=\frac{1}{3}$ is increased to a value of $k_B T/J_1 \simeq 1.4$.[65] In addition, a coexistence region in which the ordered and disordered phases are in equilibrium is added to the phase diagram. The coverage range over which island formation has been observed for CO on Ru(001) falls within the theoretically predicted coexistence region.

For CO on Ru(001), the magnitude of the second neighbor interaction should be considerably smaller than that of the first. From thermal desorption measurements, a value of $J_2/J_1=-\frac{1}{4}$ has been estimated.[43] Therefore, a direct comparison of the experimental transition temperatures with the calculated values is not feasible. However, a qualitative comparison reveals an interesting disparity between the theory and experiment. The exporimental values of the transition temperature, although determined only approximately, show a clear trend of rapidly decreasing transition temperature with coverage. The experimental transition temperature drops by at least one-third between $\vartheta=\frac{1}{6}$ and $\vartheta=0.10$. In contrast, the theoretical transition temperature drops by only 10% between the two coverages.[65] This is similar to the difference between the calculated coverage dependence of the intensity–temperature curves of Section IV B and the larger experimental dependence.

This discrepancy may be the result of the small island sizes of the CO overlayer (see Table II). Renormalization group calculations have shown that finite size effects can transform a flat phase boundary to one in which the transition temperature increases with coverage.[38] While the boundary conditions used in the calculation are almost certainly not the same as those which determine island size in the experimental system, the results indicate that finite size effects have the potential to perturb the phase diagram as observed experimentally.

V. CONCLUSIONS

The major conclusions of this work are summarized below:

(1) The Ru(001) surface contains steps that are one hcp unit cell (two Ru atoms) in height. Based on the broadening of the substrate beam profiles, the mean terrace width is between 50 and 100 Ru atoms. Measurements of overlayer island sizes indicate that the true terrace size distribution is closer to the larger limit for this surface.

(2) The temperature dependence of the fully ordered $(\sqrt{3}\times\sqrt{3})$ R 30° CO overlayer indicates that the frequency of the frustrated translational motion of CO parallel to the surface is approximately 45 cm^{-1}.

(3) The coverage dependence of the widths of the $\sqrt{3}$ beam profiles is inconsistent with a strict step-limited model of island formation for CO on Ru(001). There appear to be increasing numbers of smaller islands with decreasing coverage.

(4) The distribution of island sizes can have a pronounced effect on the change in the beam width during island dissolution. Using this effect, it was possible to determine the island size distribution for CO on Ru(001) and, thus, the mean island size as a function of coverage [see Eq. (16) and Table II].

ACKNOWLEDGMENTS

This research was supported by the Army Research Office under Grant No. DAAG29-79-C-0132. The research reported in this paper made use of the Dreyfus-NSF Theoretical Chemistry Computer which was funded through grants from the Camille and Henry Dreyfus Foundation, the National Science Foundation (Grant No. CHE78-20235), and the Sloan Fund of the California Institute of Technology.

[1]T. Engel and G. Ertl, J. Chem. Phys. 69, 1267 (1978).
[2]T. B. Grimley and M. Torrini, J. Phys. C 6, 868 (1973).
[3]T. L. Einstein and J. R. Schrieffer, Phys. Rev. B 7, 3629 (1973).
[4]K. H. Lau and W. Kohn, Surf. Sci. 65, 607 (1977).
[5]A. M. Stoneham, Solid State Commun. 24, 425 (1977).
[6]T. L. Einstein, Phys. Rev. B 16, 3411 (1977).
[7]K. H. Lau, Solid State Commun. 28, 757 (1978).
[8]V. Hartung, Z. Phys. B 32, 307 (1979).
[9]A. M. Brodskii and M. I. Urbakh, Surf. Sci. 105, 196 (1981).
[10]H. Pfnur, F. M. Hoffmann, A. Ortega, D. Menzel, and A. M. Bradshaw, Surf. Sci. 93, 431 (1980).
[11]A. Crossley and D. A. King, Surf. Sci. 95, 131 (1980).
[12]D. L. Adams, Surf. Sci. 42, 12 (1974).
[13]P. K. Johansson, Chem. Phys. Lett. 65, 366 (1979).
[14]E. Bauer, in *Phase Transitions in Surface Films*, edited by J. G. Dash and J. Ruvalds (Plenum, New York, 1980).
[15]H. E. Stanley, *Introduction to Phase Transitions and Critical Phenomena* (Oxford University, New York, 1971).
[16]K. Binder and D. P. Landau, Surf. Sci. 61, 577 (1976).
[17]D. P. Landau, in *Monte Carlo Methods in Statistical Physics*, edited by K. Binder (Springer, New York, 1979).
[18]J. C. Buchholz and M. G. Lagally, Phys. Rev. Lett. 35, 442 (1975).
[19]T. Engel, H. Niehus, and E. Bauer, Surf. Sci. 52, 237 (1975).
[20]G. Ertl and D. Schillinger, J. Chem. Phys. 66, 2569 (1977).
[21]T.-M. Lu, G.-C. Wang, and M. G. Lagally, Phys. Rev. Lett. 39, 411 (1977).
[22]E. D. Williams, S. L. Cunningham, and W. H. Weinberg, J. Chem. Phys. 68, 4688 (1978).
[23]W. Y. Ching, D. L. Huber, M. G. Lagally, and G.-C. Wang, Surf. Sci. 77, 550 (1978).
[24]G.-C. Wang, T.-M. Lu, and M. G. Lagally, J. Chem. Phys. 69, 479 (1978).
[25]T.-M. Lu, G.-C. Wang, and M. G. Lagally, Surf. Sci. 92, 133 (1980).
[26]M. G. Lagally, T.-M. Lu, and G.-C. Wang, in *Ordering in Two Dimensions*, edited by S. Sinha (Elsevier, Amsterdam, 1980).
[27]R. J. Behm, K. Christmann, and G. Ertl, Solid State Commun. 25, 763 (1978).
[28]R. C. Kittler and K. H. Bennemann, Solid State Commun. 32, 403 (1979).
[29]K. Christmann, R. J. Behm, G. Ertl, M. A. Van Hove, and W. H. Weinberg, J. Chem. Phys. 70, 4168 (1979).
[30]E. Domany, M. Schick, and J. S. Walker, Solid State Commun. 30, 331 (1979).
[31]A. R. Kortan, P. I. Cohen, and R. L. Park, J. Vac. Sci. Technol. 16, 541 (1979).
[32]L. D. Roelofs, T. L. Einstein, P. E. Hunter, A. R. Kortan, R. L. Park, and R. M. Roberts, J. Vac. Sci. Technol. 16, 478 (1979).
[33]L. D. Roelofs, A. R. Kortan, T. L. Einstein, and R. L. Park, Phys. Rev. Lett. 46, 1465 (1981).
[34]A. R. Kortan and R. L. Park, Phys. Rev. B (to be published).
[35]T.-M. Lu, G.-C. Wang, and M. G. Lagally, Surf. Sci. 107, 494 (1981).
[36]M. E. Fisher, *Proceedings of the Enrico Fermi International School of Physics* (Academic, New York, 1971).
[37]D. P. Landau, Phys. Rev. B 13, 2997 (1976).
[38]S. Ostlund and A. N. Berker, Phys. Rev. Lett. 42, 843 (1979).
[39]G. E. Thomas and W. H. Weinberg, J. Chem. Phys. 70, 1437 (1979).
[40]J. T. Grant and T. W. Haas, Surf. Sci. 21, 76 (1970).
[41]T. E. Madey and D. Menzel, Jpn. J. Appl. Phys. Suppl. 2, Pt. 2, 229 (1974).
[42]E. D. Williams and W. H. Weinberg, Surf. Sci. 82, 93 (1979).
[43]H. Pfnur, P. Feulner, H. A. Engelhardt, and D. Menzel, Chem. Phys. Lett. 59, 481 (1978).
[44]S. P. Weeks, C. D. Ehrlich, and E. W. Plummer, Rev. Sci. Instrum. 48, 190 (1977).
[45]S. P. Weeks (private communication).
[46]D. R. Sandstrom and S. P. Withrow, J. Vac. Sci. Technol. 14, 748 (1977).
[47]R. L. Park, J. E. Houston, and D. G. Schreiner, Rev. Sci. Instrum. 42, 60 (1971).
[48]*International Tables for X-Ray Crystallography*, (Kynoch, Birmingham, England, 1962), Vol. III.
[49]P. Feulner, H. A. Englehardt, and D. Menzel, Appl. Phys. 15, 355 (1978).
[50]J. C. Fuggle, T. E. Madey, M. Steinkelberg, and D. Menzel, Surf. Sci. 52, 521 (1975).
[51]J. A. Schwarz and S. R. Kelemen, Surf. Sci. 87, 510 (1979).
[52]W. Moritz, in *Electron Diffraction* 1927–77, edited by P. J. Dobson, J. B. Pendry, and C. J. Humphreys (The Institute of Physics, London, 1977), p. 261.
[53]J. C. Fuggle, E. Umbach, P. Feulner, and D. Menzel, Surf. Sci. 64, 69 (1977).
[54]G.-C. Wang and M. G. Lagally, Surf. Sci. 81, 69 (1979).
[55]M. Henzler, Surf. Sci. 22, 12 (1970).
[56]M. Henzler, in *Electron Spectroscopy for Surface Analysis*, edited by H. Ibach, (Springer, Berlin, 1977), Vol. 4.
[57]M. Henzler, Surf. Sci. 73, 240 (1978).

[58]T.-M. Lu, S. R. Anderson, M. G. Lagally, and G. C. Wang, J. Vac. Sci. Technol. 17, 207 (1980).
[59]R. Hosemann and S. N. Bagchi, *Direct Analysis of Diffraction by Matter* (North Holland, Amsterdam, 1962).
[60]T. E. Madey, Surf. Sci. 79, 575 (1979).
[61]N. V. Richardson and A. M. Bradshaw, Surf. Sci. 88, 255 (1979).
[62]C. O. Quicksall and T. G. Spiro, Inorg. Chem. 7, 2365 (1968). (1968).
[63]M. G. Lagally, G.-C. Wang, and T.-M. Lu, CRC Crit. Rev. in Solid State Mater. Sci. 1, 233 (1978).
[64]E. D. Williams and W. H. Weinberg, Surf. Sci. 109, 574 (1981).
[65]B. Mihura and D. P. Landau, Phys. Rev. Lett. 38, 977 (1977).
[66]L. K. Runnels and L. L. Combs, J. Chem. Phys. 45, 2482 (1966).
[67]D. S. Gaunt, J. Chem. Phys. 46, 3237 (1967).
[68]B. D. Metcalf, Phys. Lett. A 45, 1 (1973).
[69]M. Schick, J. S. Walker, and M. Wortis, Phys. Lett. A 58, 479 (1976).

Appendix 2

Least Squares

1. Least Squares with Error in All Variables

The usual equations in regression analysis assume that the independent variables can be measured exactly while assigning all the uncertainty to the dependent variables. In many cases this separation of variables into two classes is quite arbitrary since all the data contain errors. Different choices for the independent variables will give different values for the parameters, and it is not always clear which are the best values.

Consider as an example two variables x and y with a linear relationship between them. This is usually expressed as

$$y = mx + b \tag{1}$$

with the two parameters m and b to be fitted by least squares. Another straight line is

$$x = \mu y + \beta \tag{2}$$

When there are measurement errors in both x and y, these equations do not give the same line (except by coincidence). Treating the two variables symmetrically, as in

$$1 = mx + ny, \tag{3}$$

which gives the normal equations

$$\begin{bmatrix} \Sigma x_i \\ \Sigma y_i \end{bmatrix} = \begin{bmatrix} \Sigma x_i^2 & \Sigma y_i x_i \\ \Sigma x_i y_i & \Sigma y_i^2 \end{bmatrix} \begin{bmatrix} m \\ n \end{bmatrix} \tag{4}$$

(If the constant term b is close to zero, then the symmetric form in Equation (3) cannot be used.) This treatment assumes that the variables have been scaled so that the variances σ_x and σ_y are equal. For unequal variances, Equation (3) becomes

$$1 = m(x/\sigma_x) + n(y/\sigma_y) \tag{3.1}$$

The general case of linear least squares is handled similarly. The usual equation is

$$\mathbf{y} = \mathbf{xb} + \mathbf{1}b_o, \tag{5}$$

where **y** is the vector of dependent variables, **x** is the data matrix, **b** is the

parameter vector to be determined, **1** is the vector of 1's and b_o is the constant term. The symmetric form is obtained by the rearrangement

$$1 = [x|y] \begin{bmatrix} \mathbf{b}/b_o \\ 1/b_o \end{bmatrix} \tag{6}$$

using an augmented data matrix and parameter vector, from which the normal equations follow. As before, $|b_o|$ cannot be too small when this form is used.

When the number of parameters to be fitted is ≥3, there are biased estimates for **b** with smaller variance than the Gauss-Markov estimate. A general technique for obtaining reduced variance estimates is ridge regression (1, 2) with b given by

$$\mathbf{b}(k) = (\mathbf{X}^T\mathbf{X} + k\mathbf{I})^{-1}\mathbf{X}^T\mathbf{1}, \tag{7}$$

where **X** is the augmented data matrix and k is the ridge parameter. A good value for this parameter is the generalized cross-validation estimate (3) found by minimizing the function

$$V(k) = \|\mathbf{I} - \mathbf{A}(k)\mathbf{1}\|^2/[\mathrm{Trace}(\mathbf{I} - \mathbf{A}(k))]^2, \tag{8}$$

where

$$\mathbf{A}(k) = \mathbf{X}(\mathbf{X}^T\mathbf{X} + k\mathbf{I})^{-1}\mathbf{X}^T \tag{9}$$

and the Euclidean norm is used.

2. Least Squares for Conic Sections

When applying the photographic method for determining angles of incidence (4), it is necessary to find the center and radius of the image of the LEED screen on the photograph. Geometrically, any three points on the circumference are sufficient to determine the circle, but errors in measuring the coordinates of the points lead to errors in determining the unknown parameters. To obtain the high precision in the parameters needed for the angle determination technique, many data points must be measured and used in a least-squares procedure to fit a circle.

The equation for a circle, as it is usually written, is nonlinear in the desired parameters,

$$r = (x - x_o)^2 + (y - y_o)^2 \tag{1}$$

A rearrangement gives the linear form

$$1 = R^{-1}[(x^2 + y^2) - 2x_o x - 2y_o y], \tag{2}$$

where

$$R = r^2 - (x_o^2 + y_o^2) \tag{3}$$

and the parameters R^{-1}, $x_o R^{-1}$ and $y_o R^{-1}$ can be found by linear least squares. The conditioning of the normal equations can be improved by subtract off the mean values of x and y, viz., $\langle x \rangle$ and $\langle y \rangle$, and rescaling the variables by dividing by the standard deviations σ_x and σ_y to make them dimensionless

$$\xi_i = (x_i - \langle x \rangle)/\sigma_x$$

$$\eta_i = (y_i - \langle y \rangle)/\sigma_y$$

and

$$\zeta_i = [(x_i - \langle x \rangle)^2 + (y_i - \langle y \rangle)^2]/(\sigma_x^2 + \sigma_y^2) \tag{4}$$

This gives

$$\mathbf{1} = [\xi\eta\zeta] \begin{bmatrix} \alpha \\ \beta \\ \gamma \end{bmatrix}, \tag{5}$$

where

$$\alpha = -2\sigma_x/R$$

$$\beta = -2\sigma_y/R$$

$$\gamma = (\sigma_x^2 + \sigma_y^2)/R$$

and

$$R = r^2 - [(x_o - \langle x \rangle)^2 + (y_o - \langle y \rangle)^2] \tag{6}$$

The solution to Equation (5) is given via the normal equations as

$$[\mathbf{x}^T\mathbf{x}]^{-1}\mathbf{x}^T\mathbf{1} = \mathbf{b}, \tag{7}$$

where the data matrix is $\mathbf{x} = [\xi\eta\zeta]$ and the parameter vector is $\mathbf{b} = (\alpha\beta\gamma)^T$. The same fitting procedure can be used for the general conic section

$$1 = \alpha x^2 + \beta xy + \gamma y^2 + \delta x + \epsilon y, \tag{8}$$

which becomes

$$\mathbf{1} = [x_i^2 \;\; x_i y_i \;\; y_i^2 \;\; x_i \;\; y_i] \begin{bmatrix} \alpha \\ \beta \\ \gamma \\ \delta \\ \epsilon \end{bmatrix} = \mathbf{xb} \tag{9}$$

The data values x_i and y_i can be normalized as before and ridge regression can again be used to reduce the variance in **b**.

References

1. A. E. Hoerl and R. W. Kennard, Technometrics **12**, 55 (1970).

2. A. E. Hoerl and R. W. Kennard, Technometrics **12**, 69 (1970).

3. G. H. Golub, M. Heath and G. Wahba, Technometrics **21**, 215 (1979).

4. A. C. Sobrero and W. H. Weinberg, Rev. Sci. Instrum. **53**, 1566 (1982).